Contract Number: 622177

Deliverable D3.5

Geophysical Methods for Repository Monitoring

Work Package 3 Task 3.5

Project Acronym	Modern2020
Project Title	Development and Demonstration of Monitoring Strategies and Technologies for Geological Disposal
Start date of project	01/06/2015
Duration	48 Months
Lead Beneficiary	AMBERG
Contributor(s)	*ETH, TUL, VTT, STRATHCLYDE*
Contractual Delivery Date	31/08/2018
Actual Delivery Date	09/04/2019
Reporting period :	3
Version	Final

Project co-funded by the European Commission under the Euratom Research and Training Programme on Nuclear Energy within the Horizon 2020 Framework Programme		
Dissemination Level		
PU	Public	X
PP	Restricted to other programme participants (including the Commission Services)	
RE	Restricted to a group specified by the partners of the Modern2020 project	
CO	Confidential, only for partners of the Modern2020 project and EC	

© Modern2020

Contents

© Modern2020

© Modern2020

Abstract

Geophysical techniques offer excellent means for non-intrusive monitoring radioactive waste repositories. Here, we consider seismic and geoelectrical methods. Previous studies have identified seismic full waveform inversion (FWI) to be the most promising option for delineating subtle changes of physical properties within a repository using data acquired at safe distances outside of the repository. Significant anisotropy of the host rock, particularly in clay environments, precluded so far application of FWI technology for repository monitoring. With the development of a novel model parameterization, this problem could be addressed in the framework of Modern2020. Moreover, incorporation of structural constraints, that is, enforcing structural similarity of different physical parameters, further improved the quality and reliability of our FWI algorithms. This was demonstrated with synthetic data and a field data set acquired in the Mont Terri rock laboratory.

For a better characterization of small differential changes between two consecutive experiments, a novel differential tomography methodology was developed. It was tested with field data sets, for which traveltime and amplitude inversions were applied. It is expected that this new method can be transferred in a straightforward manner to FWI problems.

FWI technologies require extensive data analyses and substantial computer resources. Therefore, it was checked, if it is possible to employ quick and inexpensive tools, with which temporal changes in a repository can detected, but not necessarily imaged. For that purpose, an anomaly detection algorithm was developed, and it will be tested with field data.

In addition to seismic methods, electrical techniques can provide valuable information for repository monitoring. Therefore, tomographic algorithms for geoelectrical and induced polarization data were established and tested with laboratory data. For transferring the electrical parameters, obtained from these tomographic inversions, into relevant physical parameters, such as temperature and moisture content, calibration measurements were performed, and constitutive relationships between these parameters were established. The developments of the geoelectrical techniques, resulting from the Modern2020 project, are currently being validated in the framework of the Tournemire demonstrator experiment.

© Modern2020

List of Figures

© Modern2020

© Modern2020

List of Tables

© Modern2020

Glossary

4D:	Time-lapse
ANN:	Artificial neural networks
BH:	Borehole
DT:	Decision trees
EBS:	Engineered barrier systems
EDL:	electrical double layer
EDZ:	Excavation damage zone
ERT:	Electrical Resistivity Tomography
ETH:	Federal Institute of Technology Zurich, Switzerland (ETH Zurich)
FWI:	Full waveform inversion
GBM:	Granulated bentonite mixture
GIF:	Geophysical Inversion Facility
GPR:	Ground penetrating radar
HLW:	High-Level Waste
ID:	Identification
ILLL:	Intermediate level long lived
IP:	Induced Polarisation
IPT:	Induced Polarisation Tomography
LTRBM:	Long Term Rock Buffer Monitoring
PFE:	Percent frequency effect
PVC:	Polyvinyl Chloride
RH:	Relative Humidity
RTG:	Radioisotope Thermoelectric Generator
SEALEX:	Tests de performance de scellements
SVM:	Support vector machines
STRATCHCLYDE:	University of Strathclyde, U.K.
TDR:	Time Domain Reflectometer
TEG:	Thermo-Electric Generator
THC:	Thermo-hydro-chemical
TI:	Transversely isotropic
TUL:	Technical University of Liberec, Czech Republic
UBC:	University of British Columbia
URL:	Underground Rock Laboratory
VTT:	VTT Technical Research Centre of Finland
WDT:	Wireless Data Transmission

© Modern2020

1. Introduction

Geophysical techniques offer powerful means for the implementation of non-intrusive monitoring of radioactive waste repositories, but progress should be made in the conversion of geophysical variables into relevant physical for engineered barrier systems (EBS). The indirect nature of geophysical measurements (i.e., material properties are not measured directly, but through the geophysical data that are affected by the material properties relevant to repository system) can result in considerable uncertainties and ambiguities. Extensive reviews and previous work performed in the preceding MoDeRn project revealed that seismic full waveform inversion (FWI) currently offers the most promising opportunities, but also geoelectrical methods can offer very useful information. Results, obtained so far with both techniques, show that there is a great margin for improvements.

Four partners, namely ETH Zurich, Switzerland (ETH), Technical University of Liberec, Czech Republic (TUL), University of Strathclyde, U.K. (STRATHCLYDE) and the VTT Technological Research Center, Finland (VTT) teamed up to tackle some of the most burning problems. The main task of ETH was to further improve seismic FWI technologies, such that they become applicable to repository monitoring. Furthermore, novel differential tomography techniques should be explored that will allow the identification of subtle temporal changes. Since the tomographic imaging methods to be developed by ETH represent a considerable computational chore, TUL's mandate was to establish quick and inexpensive means to just identify (not necessarily image) anomalies.

VTT and STRATHCLYDE joined forces to explore possibilities and limitations of electrical methods. For that purpose, the task of VTT was to establish suitable tomographic algorithms, with which not only geoelectrical data, but also induced polarization (IP) measurements can be inverted. STRATHCLYDE's focus lied on the calibration of the electrical data, such that the corresponding electrical parameters can be related to other physical parameters of interest (temperature, pressure, moisture content, etc.).

The specific research tasks for the individual subprojects can be summarized as follows:

Seismic waveform inversions (FWI)

Existing FWI algorithms were further developed, such that they can be applied for non-intrusive radioactive waste repository monitoring. The methodological developments include:

- identification and implementation of suitable parameterizations of anisotropy,
- applying structural constraints for improving the reliability of FWI inversions,
- establishing suitable pre-processing strategies that lead to stable inversion results, and
- application to field data.

Differential tomography

Differential inversions of monitoring data are expected to provide more accurate results, because they consider only differential changes between individual measurement suites, and are thus less susceptible to systematic errors compared with traditional inversions. Here, it is investigated if such methods can be applied to ground-penetrating-radar (GPR) data acquired in the framework of a full-scale emplacement (FE) experiment conducted in the Mont Terri Rock laboratory, with the idea to later transfer this technology to seismic FWI problems.

© Modern2020

Anomaly detection algorithms

The primary objective of this subtask is to design, implement and test algorithms capable of detecting small-scale temporal data changes in the seismic data. In contrast to the tomographic methods, these techniques are not expected to provide images of the radioactive waste repository and their surroundings, but they should yield efficient and inexpensive means for the detection of anomalies. In this context, the term "anomaly" refers to differential changes in the geophysical data.

Geoelectrical techniques

Besides considering seismic methods, Task 3.5 also includes developments of Electrical Resistivity Tomography (ERT) and Induced Polarisation Tomography (IPT). Specific objectives of this module include

- development of optimal numerical conceptualization, monitoring protocol and inversion processes for the combined ERT/IPT in the canister-buffer-bedrock system, and
- development of a 3D/4D ERT/IPT inversion process with the possibility to include thermo-hydro-chemical (THC) constraints (information from point-sensor time-series, from petrophysical dependences as well as from dynamic THC behaviour/knowhow).

In addition to developing the tomographic inversions codes, it is also planned to establish relations between the electric material properties and geotechnical properties, such as water content, temperature, etc. This should be achieved by measuring electrical properties of Bentonite samples at controlled geotechnical properties, and validating the results with a field-scale experiment.

This is the final technical report of the Task 3.5 of the project. The aim of this deliverable is to synthetize the progress achieved in the Task 3.5 R&D activities. It briefly includes the methodological background of the individual methods employed, and it contains all the key results obtained from numerical experiments, laboratory tests and field studies. Finally, the new findings are critically reviewed and specific recommendations for potential applications to radioactive waste repository monitoring are provided.

© Modern2020

2. Seismic full waveform inversion (ETH)

2.1 Background information

Effective monitoring of radioactive waste repositories that does not compromise the engineered and natural barriers is challenging. Seismic full waveform inversion (FWI) is one of the few possible options that offer the resolution required. In case of seismic FWI, elastic waves are generated at some distances from the repository. These waves propagate through the repository and are recorded by a seismic acquisition system. Due to interactions between the seismic waves and the repository, the recorded seismograms are influenced by the physical state of the repository. Hence, the seismograms contain information about elastic properties of the repository. This information is used by the FWI algorithm to get subwavelength resolution images of the elastic properties of the repository.

The work carried out in previous MoDeRn and ESDRED projects regarding seismic monitoring has highlighted that seismic data contain information on the elastic properties that can be indicative for the actual state of the repository, but (Manukyan et al., 2012b) has noted that significant progress in FWI needs to be made before this technique can be used in radioactive waste repositories. In particular, it was found that in the presence of an anisotropic host rock, the model parameterization (i.e., the choice of the parameters characterizing the elastic properties) is still an unsolved problem (e.g. Manukyan, 2011; Alkhalifah and Plessix, 2014; Gholami et al., 2013; Guitton and Alkhalifah, 2017). Application to field data is even more challenging due to the ambient noise, three-dimensional effects, variable source and receiver coupling terms, etc.

The first priority of the research to be conducted in Modern2020 therefore included the development of an inversion parameterization that can produce high-resolution models for cross-hole experiments. This new model parameterization was tested on synthetic data sets and with a data set recorded in Mont Terri Underground Rock Laboratory (URL).

2.2 Methodological Developments

Here, we provide a brief summary of the methodological developments. A more detailed description of our work can be found in Manukyan and Maurer (2019). FWI is a complex topic, and it is beyond the scope of this report to provide all the technicalities of the approach. For more general information on FWI, it is therefore referred to the textbook of Fichtner (2011) and the review paper of Virieux and Operto (2009) and references therein.

FWI iteratively minimizes an objective function that incorporates the discrepancies between observed and predicted waveforms (e.g., Pratt and Worthington, 1990; Tarantola, 1984). The equations for regularized elastic seismic FWI in the least squares sense can be written as

$$\begin{bmatrix} \mathbf{J} \\ \alpha\mathbf{I} \\ \beta\mathbf{L} \end{bmatrix} \mathbf{m}^{n+1} = \begin{bmatrix} \left(\mathbf{d}^{obs} - \mathbf{d}^{pred}\right) + \mathbf{J}\mathbf{m}^{n} \\ \alpha\mathbf{m}^{ref} \\ 0 \end{bmatrix}, \qquad (4.1)$$

where $\mathbf{J}$ is the Jacobian matrix, $\mathbf{m}$ is a set of inversion model parameters characterizing the elastic properties, superscripts *n* and *n+1* indicate the iteration numbers, $\mathbf{m}^{ref}$ is the reference model, which is either an a priori model from independent sources of information or the current model $\mathbf{m}^{n}$, $\mathbf{d}^{obs}$ and $\mathbf{d}^{pred}$ are observed and predicted waveform data, respectively. The damping coefficient α and the smoothing coefficient β are introduced to stabilize the inversion. Since the FWI problem is highly non-linear, Equation 4.1 needs to be solved iteratively.

© Modern2020

The predicted data ($\mathbf{d}^{pred}$) are calculated by solving the elastic wave equation (i.e., solving the forward problem):

$$\rho \frac{\partial^2 u}{\partial t^2} = \nabla \cdot \left(C : \nabla u \right) + F \,, \tag{4.2}$$

where ρ is the mass density, t is the time, $u = \begin{bmatrix} u_x & u_y & u_z \end{bmatrix}^T$ is the displacement vector (quantity recorded by the seismic sensors), $F = \begin{bmatrix} f_x & f_y & f_z \end{bmatrix}^T$ is the external force (seismic source), $\nabla = \begin{bmatrix} \partial_x & \partial_y & \partial_z \end{bmatrix}$ is the gradient vector operator and C is the elasticity tensor. The model parameterization includes the spatial distribution of the elements of C and ρ, that is $C(x,y,z)$ and $\rho(x,y,z)$.

In a generally anisotropic medium, C has 21 independent coefficients. Here, we restrict ourselves to a 2D problem (i.e., $C = C(x,z)$ and $\rho = (x,z)$). Furthermore, we make the simplifying assumption of transverse isotropy (TI), that is, the material properties are expected to exhibit only anisotropic behavior along a specified spatial direction defined by the so-called symmetry axis. Generally, the (local) symmetry axes can vary spatially, but in repository host rocks with significant anisotropy (i.e., clays), it can be safely assumed that the symmetry axis remains constant within the area of interest. For the sake of notational simplicity, we specify the FWI coordinate system, such that the symmetry axis is parallel to the z-axis.

Considering all these assumptions and conventions, the elasticity tensor can be reduced to four independent elements, namely C_{11}, C_{13}, C_{33}, and C_{44} (Voigt notation is used). The 2D distributions of these elements and the density ρ constitute the elements of the sought model vector m in Equation 4.1.

In the framework of MoDeRn and ESDRED, we developed an anisotropic FWI algorithm with such a model parameterization. Unfortunately, the results were not satisfactory, which was one of the main drivers of the research performed in Modern2020.

Novel model parameterization

We have tested a variety of other model parameterizations, and we came finally up with a new set of parameters. It includes the density ρ, and the combined parameters

$$\begin{aligned} V_P^{90} &= \sqrt{\frac{C_{11}}{\rho}}, \quad V_P^0 = \sqrt{\frac{C_{33}}{\rho}}, \\ V_S^0 &= \sqrt{\frac{C_{44}}{\rho}}, \quad V_{13} = \sqrt{\frac{C_{13}}{\rho}}, \end{aligned} \tag{4.3}$$

As shown later, such a model parameterization does not only lead to satisfactory results, but also includes parameters that have a physical meaning. V_P^0 and V_P^{90} are the P-wave velocities parallel and perpendicular to the symmetry axis, and V_S^0 is the S-wave velocity parallel to the symmetry axis. Only the parameter V_{13} has no obvious physical meaning.

© Modern2020

Structurally constrained FWI

In the case of 2D elastic TI FWI, there are five independent elastic inversion parameters, namely , V_P^0 , V_P^{90} , V_S^0 , V_{13} and ρ. For the simpler elastic isotropic FWI problem, which has only three independent inversion parameters, Manukyan et al. (2012a) have shown that the resolution characteristics of different model parameters strongly depend on the parameter type. Moreover, depending on the experimental configuration there might be strong cross talks between different model parameters during the inversion (Köhn et al., 2012; Manukyan et al., 2012a; Operto et al., 2013). Since FWI is an iterative process, both the poorer convergence of some model parameter types and the parameter trade-offs can adversely affect the overall convergence of the inversion. To improve the convergence behavior of the inversion for elastic isotropic FWI, Manukyan et al. (2018) recently developed a structurally constrained FWI approach, which additionally penalizes structural differences between different model parameters. Here, structural similarity is enforced by so-called cross-gradient constraints.

Tests with synthetic data

For testing the new parameterization, we have set up a test model as shown in Figure 1. It includes a source and a receiver borehole, and deterministic anomalies in form of crosses and an elongated zone. To make this test more realistic, stochastic fluctuations were added to all parameters.

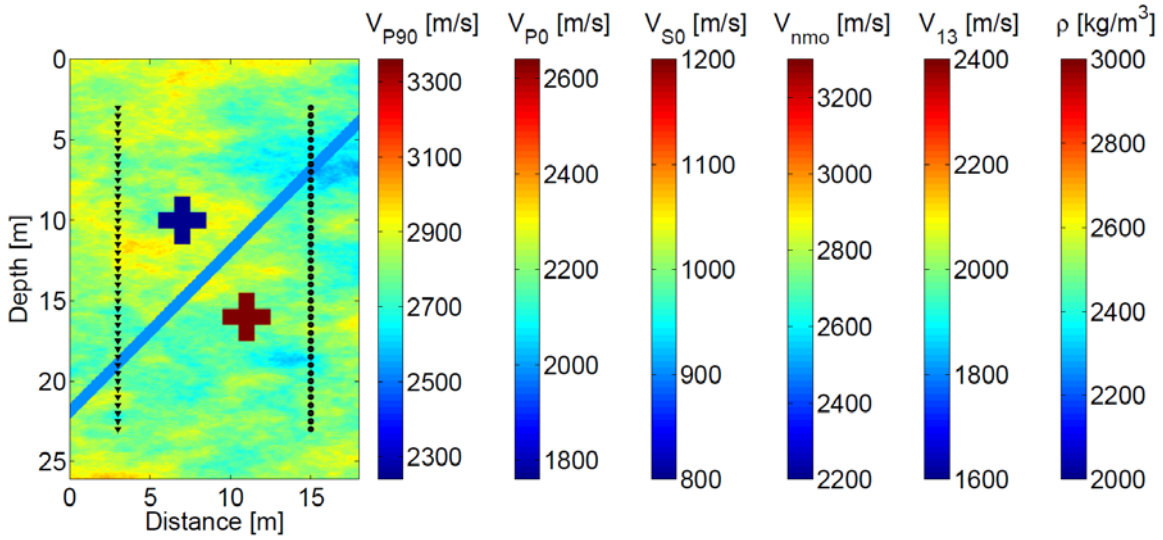

Figure 1. True model parameters for FWI. Sources are marked with triangles and receivers with dots.

Synthetic data were computed for the configuration shown in Figure 1. They were treated like "observed" data ($\mathbf{d}^{obs}$ in Equation 4.1), and it was checked, if the true model parameters could be reconstructed. The results obtained without structural constraints are shown in Figure 2. All parameters resolve the deterministic anomalies, although at similar fidelity.

When adding the structural constraints, the tomograms in Figure 3 are obtained. The quality of the tomographic images improved considerably for all parameters.

© Modern2020

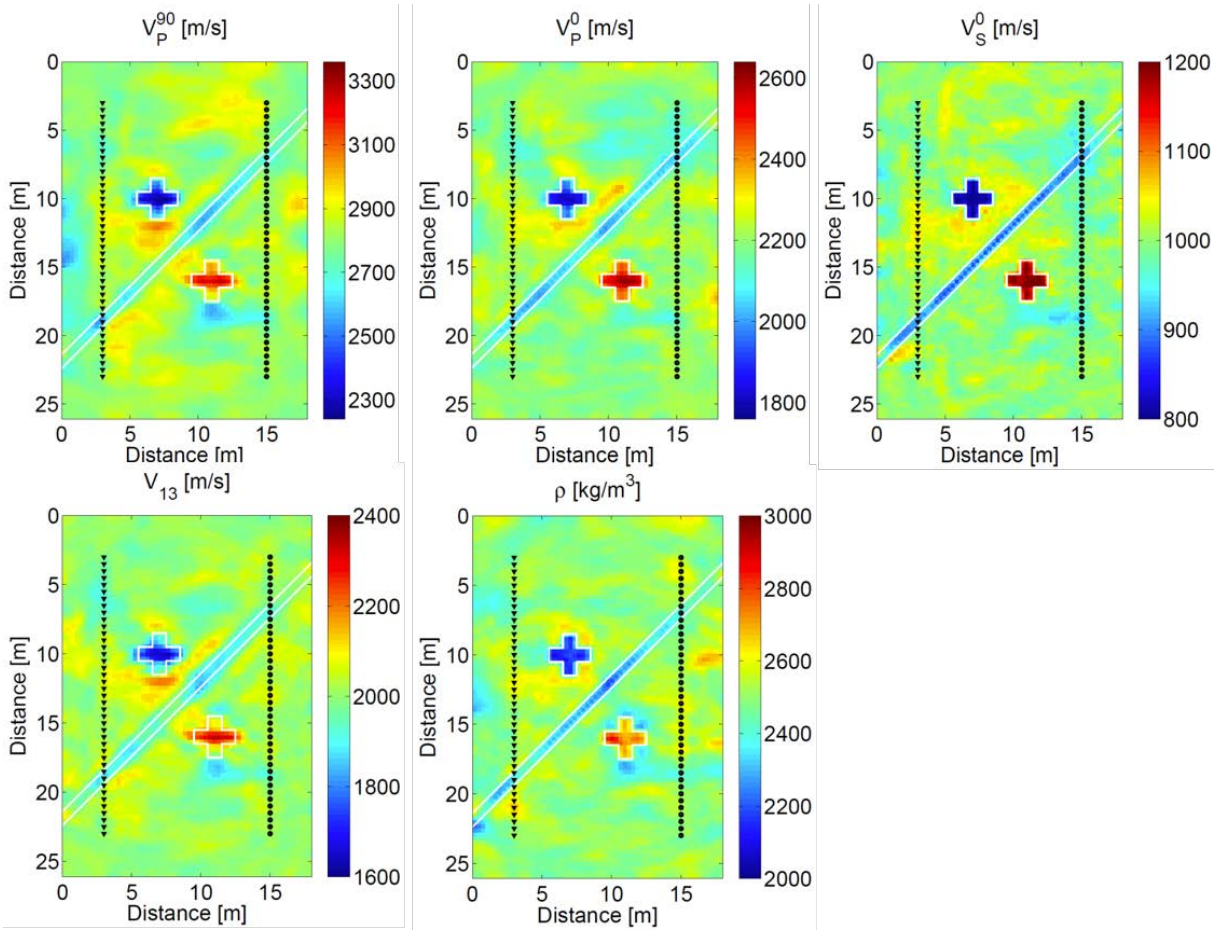

Figure 2. Inversion results without structural constraints.

© Modern2020

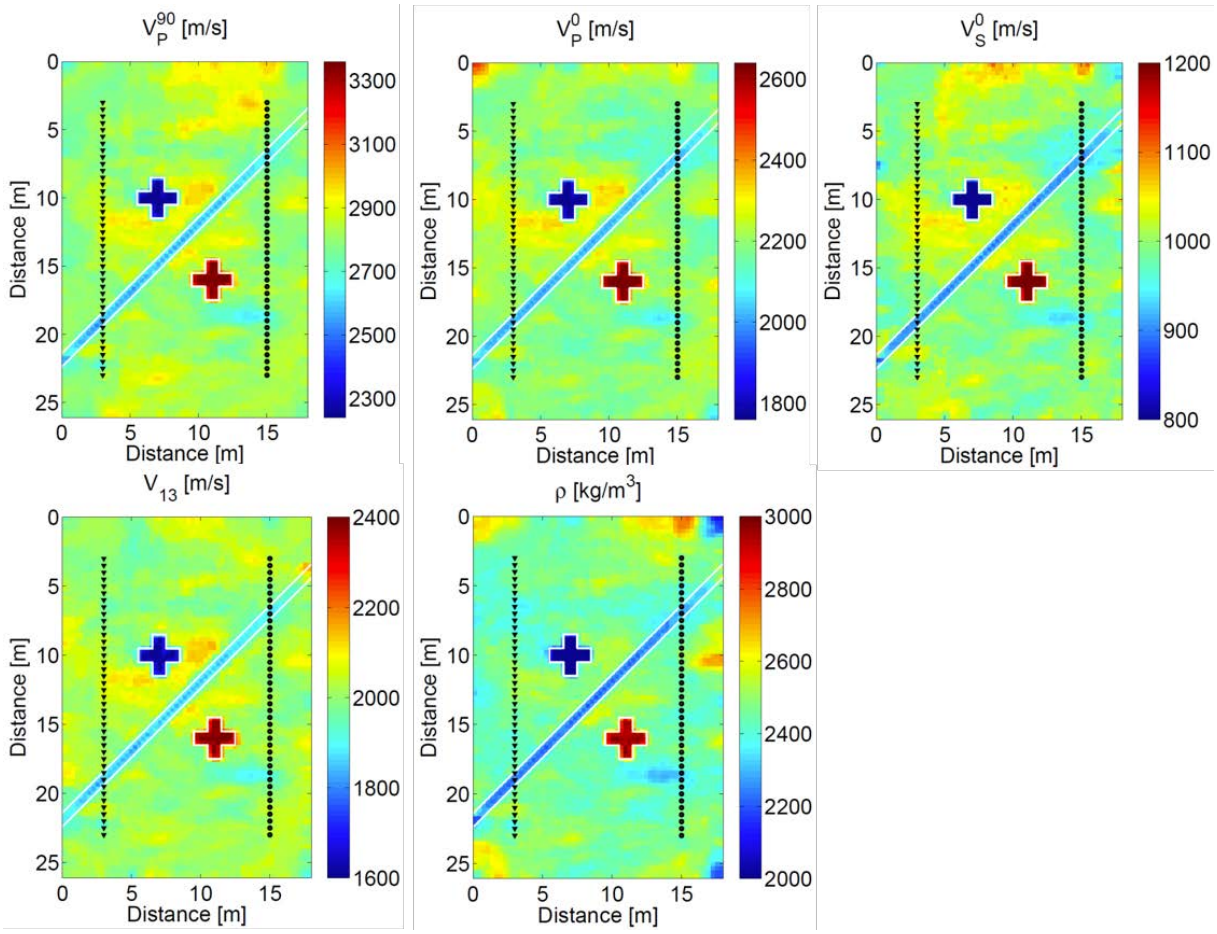

Figure 3. Inversion results with structural constraints.

2.3 Validation with experimental data

The synthetic tests demonstrated that the novel technologies are expected to provide useful results, but before this FWI technology can be recommended as a tool for repository imaging and monitoring, it has to be demonstrated that it is also applicable to realistic field data sets. There are several factors that may affect FWI results from field data, including, for example,

- 3D (out-of-plane) effects for 2D FWI,
- the presence of noise, and
- effects not considered in the solution of the forward problem (Equation 4.2) that may require data pre-processing (i.e., restriction to selected time windows of the seismograms).

Seismic tomography experiments were conducted at the Mont Terri URL in the Opalinus Clay in north-west Switzerland. We made use of an experimental setup, as set up for the so-called HG-A experiment (Manukyan, 2011). The experiments, described here, are unrelated to the actual HG-A experiments (i.e., they share only the test site), and the data were acquired in the framework of the Modern2020 project with the goal to image the 1-m-diameter HG-A tunnel, its excavation damage zone (EDZ) and significant geological structures. The experimental setup is shown in Figure 4. Seismic signals were generated with a high frequency P wave sparker source at every 0.25 m in the lower borehole and recorded with 48 three-component geophones. The geophones were cemented in the upper borehole with 0.5 m spacing between the sensors.

© Modern2020

For establishing a reasonable initial model for the FWI, the P-wave travel times of the data set was analyzed. This indicated that within the domain of interest there are two major reasons for P-wave velocity variation. Firstly, P-wave velocity depends on the direction of the wave propagation due to the pronounced anisotropy of the Opalinus clay host rock. Secondly, the traveltime analysis shows that there is a strong dependence of P-wave velocities on the spatial location. To visualize the spatial variation of P-wave velocity in Figure 5 we eliminated the effect of anisotropy by depicting all seismic rays that propagate within 1° from vertical under a straight ray approximation. These rays are colour coded according to their apparent P-wave velocities. It can be seen that (i) the closer the ray is to the main tunnel the smaller is the P-wave velocity and (ii) the traveltime data does not contain any information about the microtunnel. The same observations could be made also for other ray directions (not shown). Velocity decreases within 10 to 15 m away from the main tunnel can be due to the EDZ of the main tunnel.

On the basis of the observations in Figure 4, we generated a starting model for FWI as a simple one dimensional velocity variation with horizontal distance from the main tunnel by explicitly incorporating the EDZ of the main tunnel and fitting all picked traveltimes. As indicated earlier, we rotated the coordinate system to make the symmetry axis vertical (Figure 6).

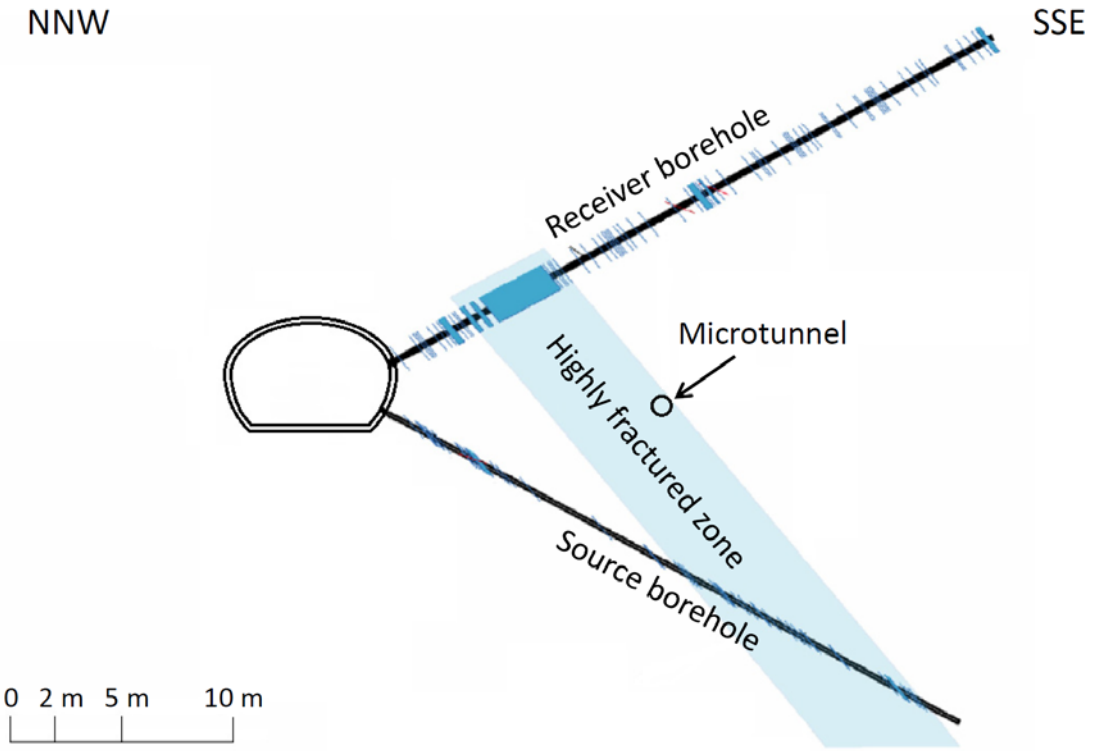

Figure 4. Schematic drawing of the layout of the non-intrusive seismic tomography experiment in the HG-A micro-tunnel at Mont Terri URL.

© Modern2020

Since FWI for 3D anisotropic media is computationally very expensive, and the design of the experiment allows for the 2D approximation, similar to the synthetic study, we performed 2D TI FWI. To eliminate pipe waves (e.g., Marelli et al., 2010) as well as out-of-plane reflections that could jeopardize the convergence of FWI, we time-windowed the recorded data around the first break by exponentially reducing seismogram amplitudes with time. Additionally, we accounted for the 3D spherical divergence of the field data using an asymptotic 2.5D filtering procedure (Bleistien, 1986). Finally, we estimated the source wavelet and receiver coupling factors before each inversion iteration using the methodology developed by Maurer et al. (2012).

Figure 7 shows TI FWI results of the Mont Terri data. Images of V_P^{90}, V_S^0 and V_{13} show a clear, 1-2 m wide layer with lower velocities. This layer is a high-frequency fracture zone detected by borehole logging (Lanyon, 2008). Additionally, reconstruction of V_P^0 indicate the presence of the microtunnel and its EDZ, but the reconstruction is rather blurred. A hint of the microtunnel and the EDZ can be seen also on V_P^{90} and V_{13} images. Despite the application of the structural constraints, there are large differences between different model parameter types close to borehole ends. This could be due to attenuation of the host rock that is not taken into account in the inversion.

A comparison of recorded and predicted data is shown in Figure 8. We can see that the model is able to match both receiver components very well.

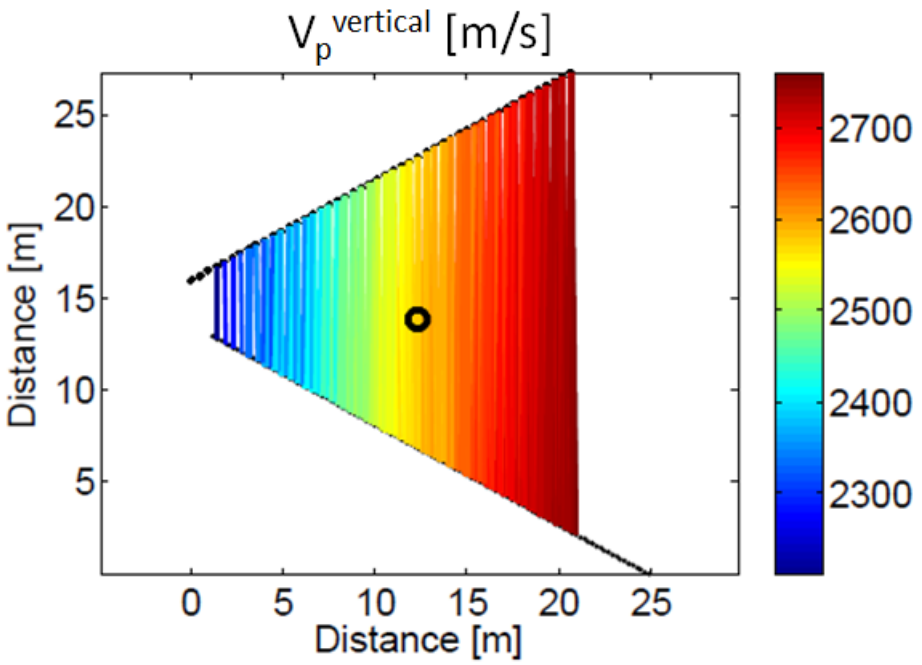

Figure 5. Apparent velocities of P-waves propagating within 1° from vertical under a straight ray approximation. Each ray is color coded according to its apparent velocity.

© Modern2020

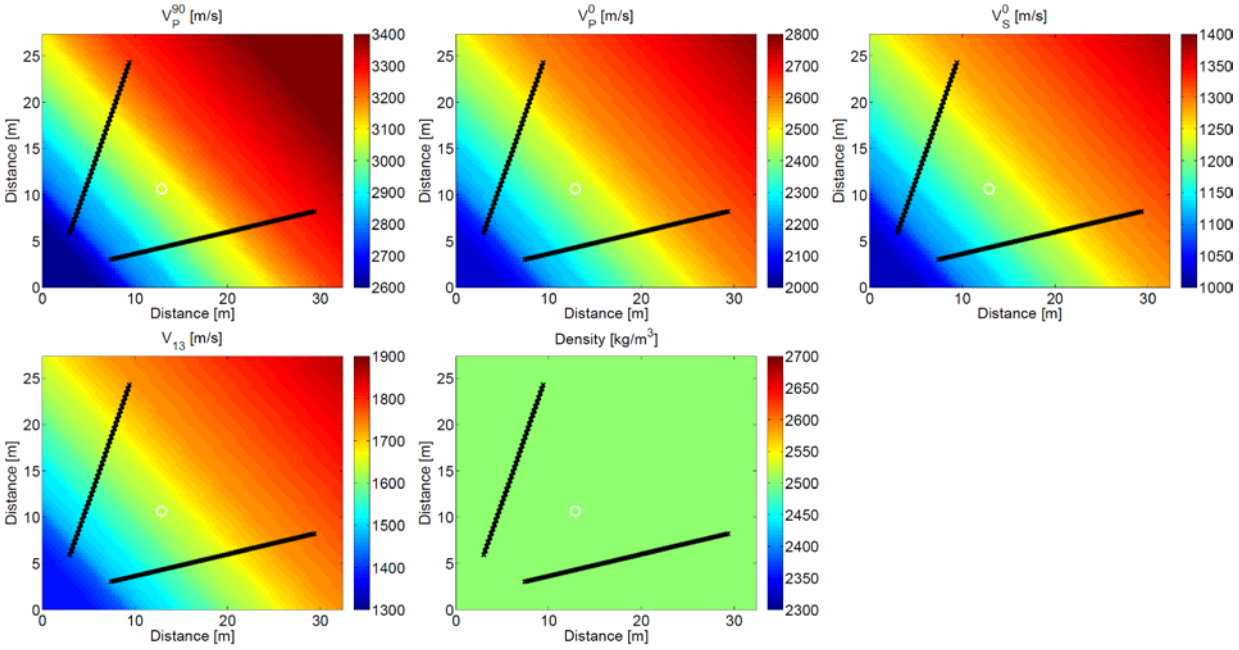

Figure 6. The starting model used for FWI of data recorded in Mont Terri. The coordinate system is rotated in order to make the direction of symmetry axis vertical. Black crosses indicate locations of sources and receivers. White circles indicate location of the microtunnel.

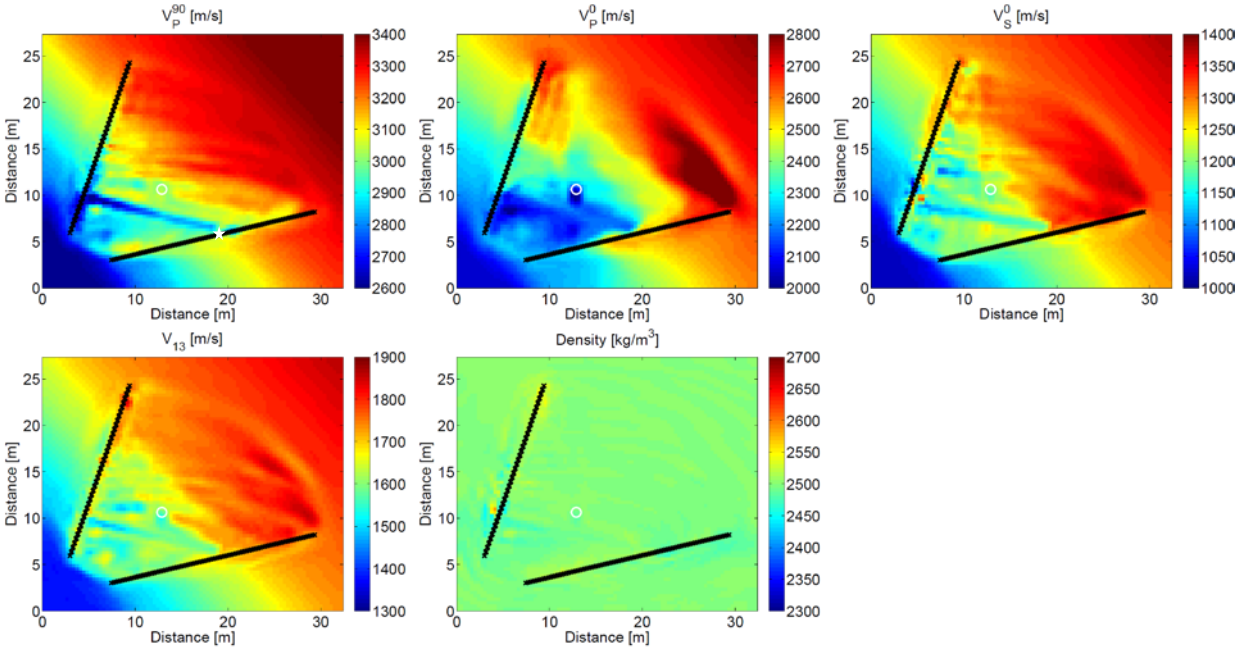

Figure 7. FWI results of data recorded in Mont Terri. The coordinate system is rotated in order to make the direction of symmetry axis vertical. Black crosses indicate locations of sources and receivers. White circles indicate location of the microtunnel. White star indicate the source location for shot gathers of Figure 8.

a b

© Modern2020

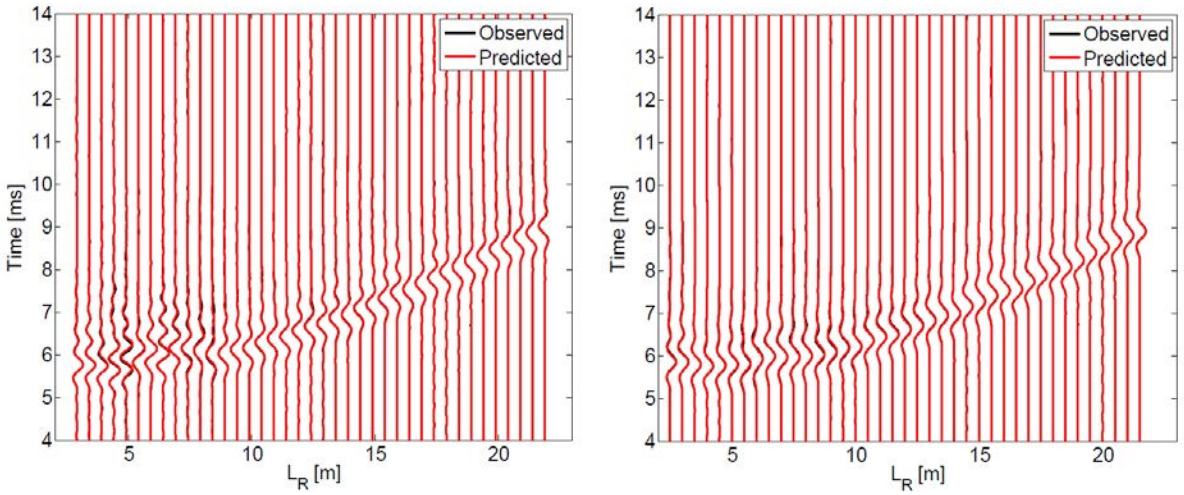

Figure 8. Comparison of observed and predicted seismograms for geophone direction parallel (a) and perpendicular (b) to the receiver borehole for a source indicated by a white star in Figure 7.

2.4 Discussion, conclusions and outlook

With our work on the non-intrusive seismic monitoring of radioactive waste repositories, we were able to discover a model parameterisation, which allows successful FWI for TI media. Furthermore, our numerical experiments showed that incorporation of structural constraints into the anisotropic FWI allows further improvement of tomographic images. We applied the new algorithm to the data recorded around HGA tunnel in the Mont Terri URL. Our inversion results show that with FWI we were able to detect the microtunnel and its EDZ as well as prominent repository structures, such as the predicted fracture zone.

Although these achievements are key for future applications of repository monitoring, there are still a few open points that will require further research.

- In our calculations, the effect of inelastic attenuation was mainly absorbed by source and receiver terms since we did not take into account the effect of inelastic attenuation. Hence, the tomographic images can be further improved by developing a robust algorithm for the calculation of inelastic attenuation.
- Further improvements can be made by replacing the pressure sources by directional sources or by using both of them.
- The primary goal of this Modern2020 research task was to obtain high-resolution FWI images. In a next step, the following points need to be addressed
    - The elastic properties, now expressed by means of V_P^{90}, V_S^0, V_{13} and ρ, need to be converted to physical properties, such as effects of moisture content, pressure and temperature. This requires corresponding constitutive relationships to be established.
    - For the sake of computational feasibility, a 2D FWI was considered, but with the availability of increasing computer power, the approach should be extended to 3D FWI.
    - Ultimately, it will be not only required to obtain images of the repository and its surroundings, but also to monitor subtle differential temporal changes. Section 3 outlines a possible option that may be also applicable to FWI data.

© Modern2020

3. Differential tomography with waveform phase data (ETH)

3.1 Background information

Monitoring temporal changes within a volume of interest is one of the primary missions of geophysical surveying, and it finds many applications related with near surface targets, such as groundwater fluctuations (e.g., Doetsch et al., 2010), freezing and thawing of permafrost (e.g., Hauck and Muhll, 2003), and radioactive waste repository monitoring (e.g. Manukyan et al., 2012b). The latter is likely the most challenging task, since only very subtle changes are expected to occur.

The simplest monitoring option is to perform repeated surveys in a consistent manner and to analyze the data sets individually. Temporal changes can then be inferred by qualitative or quantitative comparisons of the tomographic images (parallel difference strategy, e.g., Asnaashari et al., 2015). If a tomographic inversion algorithm is involved in the data analysis, the results obtained from a first data set can be used as the initial model for the inversion of the follow-up data set (sequential difference strategy). It is also possible to invert directly for the differences of two data sets. According to Asnaashari, et al. (2015), this is referred as the double-difference strategy. This approach is particularly useful (i) in the presence of systematic data errors, and (ii), when the data differences can be determined more accurately and/or more consistently than the actual data. If *a priori* information is available on the temporal behavior of the quantities of interest, it can be included as well. As shown by Day-Lewis et al. (2002) and Karaoulis et al. (2014), this can be achieved by simultaneously inverting for all data sets, while imposing constraints on the temporal changes.

Here, we applied double-difference traveltime tomography to a GPR data set that was acquired in the framework of the FE full-scale experiment at Mont Terri (Müller et al., 2017). We first outline, how highly accurate and consistent traveltime data can be obtained as input for the double-difference tomography. Since the temporal evolution of the physical properties of interest is unknown and may include abrupt and slowly varying components, it is in our application not possible to impose temporal constraints. Instead, we introduced a more general technology, with which the consistency of the differential tomograms can be checked and improved.

It should be noted that this study considers GPR waveform phase information and not full waveform seismic data. Furthermore, the sensors are placed within the material to be investigated, which also does not represent a realistic scenario. However, results from this study provide important prerequisites towards non-invasive monitoring using seismic FWI. As discussed in more detail in the conclusion and outlook section, it will be, at least conceptually, a relatively trivial matter to extend the technology presented here to a more realistic scenario.

Experimental setup

The FE experiment is (still) running in the Mont Terri Rock Laboratory (Bossart and Thury, 2007). Its main objective is to demonstrate that high-level radioactive waste can be emplaced and stored safely in a deep geological repository, whereby a particular emphasis is set on a better understanding of thermos-hydro-mechanical (THM) effects (Müller et al., 2017). For that purpose, a 3 m diameter tunnel was drilled that should mimic a full-scale repository disposal gallery. High-level radioactive waste canisters are simulated by placing three heaters within the tunnel. After their installation, the tunnel was backfilled with a granulated bentonite mixture (GBM) and finally sealed with a shotcrete plug. The heaters were then switched on, and temperatures reached approx. 130° Celsius on the heater surfaces, and, depending on the position, 45 to 60° at the tunnel walls.

© Modern2020

As described in Müller et al. (2017), more than 1500 sensors were installed for monitoring all relevant physical parameters (temperature, humidity, etc.). For monitoring temporal changes of the GBM, two fiberglass pipes were inserted prior to the installation of the shotcrete plug. As shown in Figure 9, these pipes extend beyond the first heater in the tunnel. They were employed for a variety of borehole logging surveys and crosshole measurements.

Here, we consider GPR crosshole data that were acquired with 250 MHz borehole antennas. First, the receiver antenna was placed at 0.25 m intervals within borehole GP2, and for each receiver position crosshole data were acquired by moving the transmitter antenna in 0.05 m intervals within borehole GP1. Subsequently, the procedure was repeated by placing the receiver antenna in GP1 and the transmitter antenna in GP2. The first experiment was performed prior to the installation of the shotcrete plug, and repeat experiments were subsequently performed twice a year. So far, six experiments were carried out.

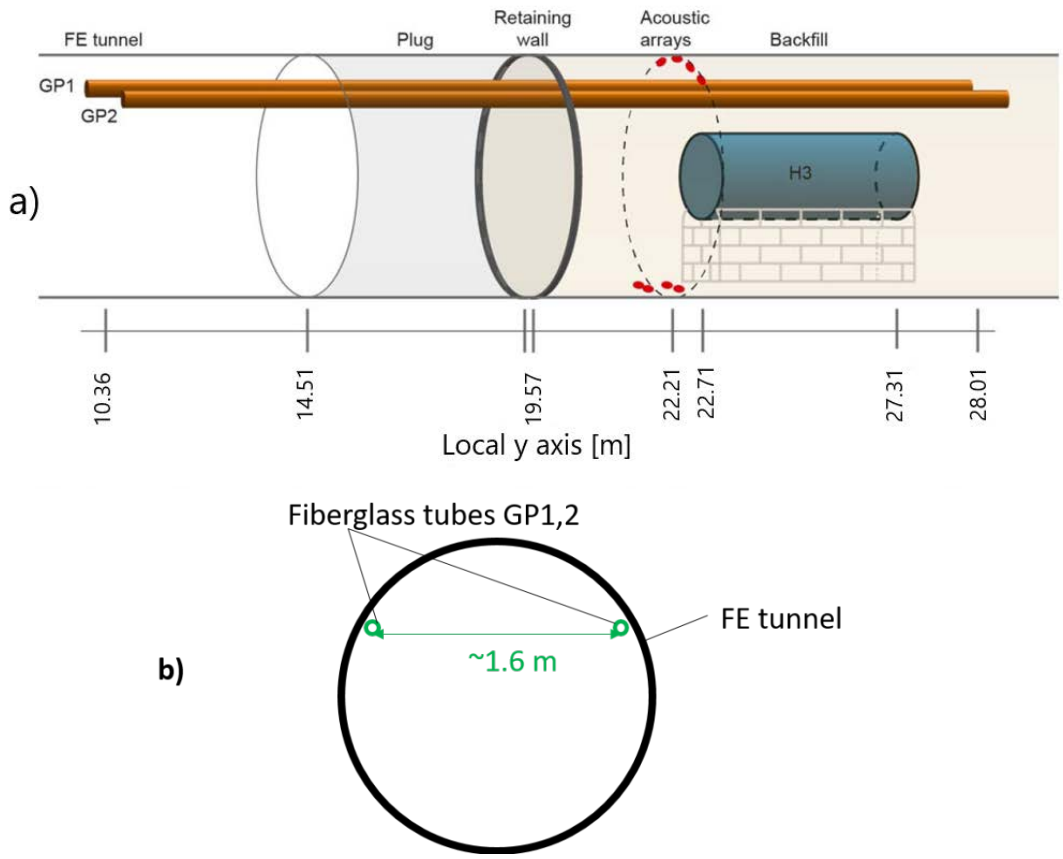

Figure 9. Setup of the FE experiment. a) Side view – GP1 and GP2 are the fiberglass tubes within which the crosshole experiments were performed. H3 represents the heating unit. b) View along the tunnel axis.

3.2 Methodological Developments

Determining high-precision differential traveltime data

Initially, the arrival times of the first arriving waves were picked manually. Then, the accuracy and consistency of the picks was improved using the following procedure.

1. Within each receiver gather, all traces s_{ijk} (*i = 1…number of sources*, *j = 1…number of receivers*, *k = 1…number of experiments*) are cross-correlated with each other using a time window of *3 ns*

© Modern2020

centred over the manually picked first breaks. The relative shifts Δt_{abjk} (*a,b = 1…number of sources*) are determined as the lag of the maximum of the cross-correlation between the *a*th and the *b*th radargram of the jth receiver gather and *k*th experiment. Only those lags associated with sufficiently high cross-correlation coefficients are retained. After some experimentation, we have chosen a threshold value of 0.925.

2. Besides determining cross-correlations within a receiver gather, all traces of a particular source-receiver configuration are cross-correlated across all experiments, that is for each pair of *i* and *j*, all combinations of *k* are cross-correlated resulting in traveltime differences Δt_{ijcd} (*c,d = 1…number of experiments*). Again, only correlations with high cross-correlation coefficients were retained.
3. Each of the lag determinations, described in steps 1 and 2, can be written as a difference equation of the form $t_{ajk} - t_{bjk} = \Delta t_{abjk}$ or $t_{ijc} - t_{ijd} = \Delta t_{ijcd}$. All these equations can be accumulated in a system of equations of the form $\mathbf{Bt} = \mathbf{\Delta t}$, where vector $\mathbf{\Delta t}$ includes all the lags Δt_{abjk} and Δt_{ijcd}, and vector $\mathbf{t}$ includes the refined arrival times to be determined. This system of equations is highly redundant, but rank deficient, because only arrival time differences are involved. To make the system full rank, it is sufficient to include a few absolute traveltimes into the system as additional constraints. We have chosen arrivals, where the manual picking accuracy was particularly good. After solving $\mathbf{Bt} = \mathbf{\Delta t}$ the refined arrival times t_{ijk} are available for further analysis.

This procedure offers several benefits. First, it automatically eliminates traces with a poor signal-to-noise ratio. Furthermore, the redundancy of the system of equations reduces the influence of random errors. Finally, large residuals $(\mathbf{Bt} - \mathbf{\Delta t})$ are indicative for problematic data points that can be eliminated prior to the tomographic inversions.

Double difference tomography

The refined arrival times $\mathbf{t_k}$ (subsets of $\mathbf{t}$ including only arrival times of experiment *k*) are used as input for conventional traveltime tomography of the individual experiments, resulting in tomograms $\mathbf{v_k}$. Then, differential traveltime data $\mathbf{\Delta t_{mn}} = \mathbf{t_m} - \mathbf{t_n}$ (*m,n = 1…number of experiments, and m > n*) and subsequently data sets of the form $\hat{\mathbf{t}}_{\mathbf{mn}} = \mathbf{t}^{\mathbf{calc}}_{\mathbf{v_n}} + \mathbf{\Delta t_{mn}}$ are generated, where $\mathbf{t}^{\mathbf{calc}}_{\mathbf{v_n}}$ includes synthetic data computed with the velocity tomogram $\mathbf{v_n}$. These data sets are then inverted using $\mathbf{v_n}$ as initial models yielding differential tomograms $\mathbf{\Delta v_{mn}}$. For *K = 6* experiments this results in *L = K(K-1)/2 = 15* differential tomograms.

The differential tomograms $\mathbf{\Delta v_{mn}}$ are expected to provide more reliable results than just forming differences of the absolute tomograms ($\mathbf{v_m} - \mathbf{v_n}$, i.e., parallel difference strategy), because systematic errors in the absolute traveltimes $\mathbf{t_m}$ and $\mathbf{t_n}$ are eliminated in $\hat{\mathbf{t}}_{\mathbf{mn}}$. Nevertheless, the differential tomograms $\mathbf{\Delta v_{mn}}$ may still include inconsistencies. This can be examined by comparing combinations of differential tomograms. For example, the differential tomogram of the 3rd and 1st experiment can be reconstructed by summing the differential tomograms between experiments *2* and *1*, and experiments *3* and *2*, that is, $\mathbf{\Delta v}_{21} + \mathbf{\Delta v}_{32}$. It must be expected that $\mathbf{\Delta v}_{31} \neq \mathbf{\Delta v}_{21} + \mathbf{\Delta v}_{32}$, because of approximations and discretization errors within the tomographic inversion algorithm.

A possible option to reduce these discrepancies is to form all possible reconstructions (linear combinations) of the differential tomograms. The procedure has to be carried out separately for every velocity parameter Δv_{mnp} (*p = 1…number of velocity parameters*). For *K = 6* there exist *R = 57* independent options to reconstruct Δv_{mnp} (only additive reconstructions are considered). The

© Modern2020

corresponding equations can be accumulated in a system of equations $\mathbf{C}\mathbf{q}^p = \mathbf{x}^p$. Vector $\mathbf{q}^p$ includes the sought L refined velocity differences Δv_{mnp} and the right-hand-side vector $\mathbf{x}^p$ of length R includes repeated entries of original velocity differences, as obtained from the L double-difference inversions. The $R \times L$ matrix $\mathbf{C}$ includes ones at appropriate places. The system $\mathbf{C}\mathbf{q}^p = \mathbf{x}^p$ can be inverted to yield $\mathbf{q}^p$.

Similar to the procedure employed for optimizing the traveltime data, this approach does not only provide more consistent results, but it can also identify problematic velocity parameters, where the discrepancies between the original and refined velocity differences are particularly large. Furthermore, the methodology can be transferred in a straightforward manner to differential amplitude inversions.

3.3 Validation with experimental data

Velocity tomograms $\mathbf{v}_k$ obtained from $\mathbf{t}_k$ are shown in Figure 10. The velocities of the first experiment are rather high and exhibit considerable spatial variations. After switching the heaters on (between experiments 1 and 2), the velocities above the heater section decrease significantly, and the spatial variations decrease as well. The tomograms of the following experiments continue to include the low velocities above the heater, but the spatial variability increases.

Subsequently, the double difference tomography and the refinement procedures, as described above, were applied. Examples of spatial velocity difference distributions are displayed in Figure 11 where the differences of consecutive experiments are shown. As already observed in Figure 10, there is a substantial and rather homogeneous decrease of the GPR velocities over the heater. This is likely a temperature effect, since the dielectric permittivity, which is governing the GPR velocities, is temperature dependent. Further velocities decreases can be observed between experiments 2 and 3. These are probably still temperature effects, but they may be also the result of increased humidity.

In the remaining difference tomograms, we observe predominantly velocity increases, but there are also velocity decreases, particularly in the tunnel section between the heater and the shotcrete plug. Since the temperatures stabilized relatively quickly after switching on the heaters (Müller et al., 2017), these fluctuations are likely associated with increased/decreased humidity (velocity decrease/increase) and/or the formation of air-filled cracks/pockets due to stress redistributions within the GBM (velocity increase). An integrated analysis of all sensor data acquired so far will be required for a unique interpretation of the GPR difference tomograms.

© Modern2020

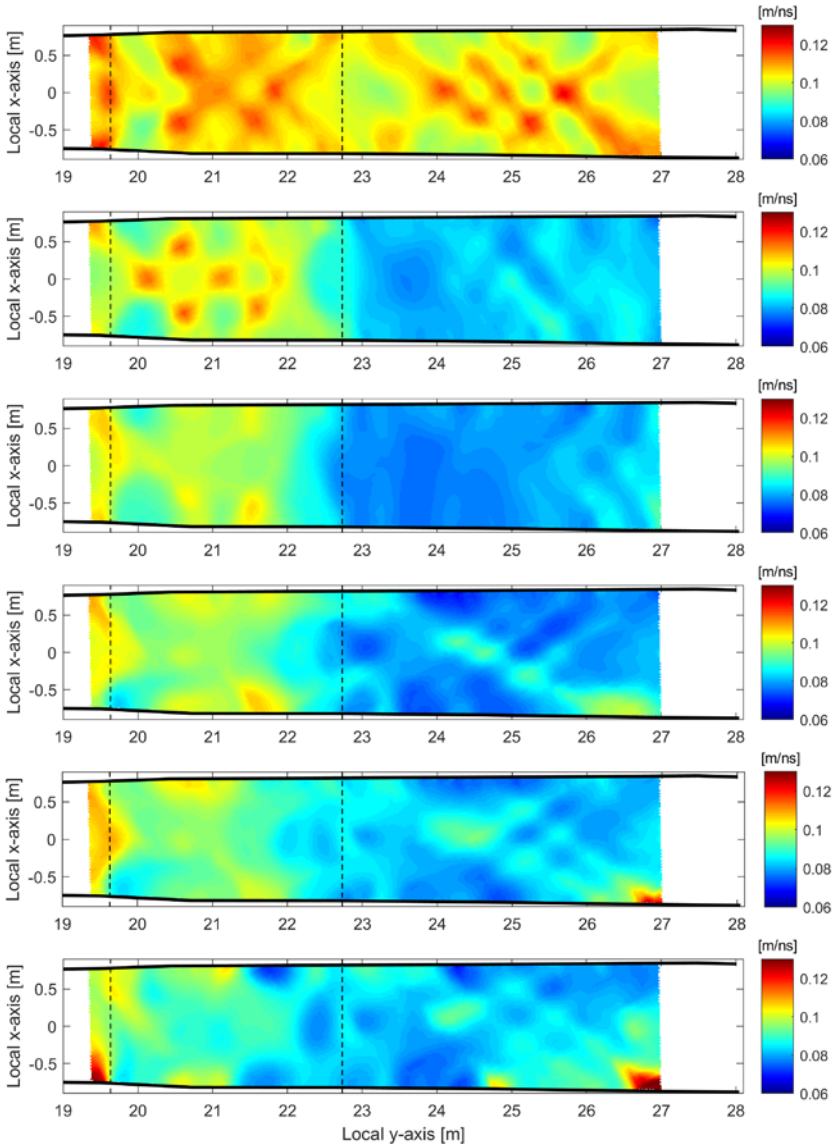

Figure 10. Tomograms obtained from the absolute inversions. The distances indicated above the tomograms correspond to the y-axis of the local coordinate system. The vertical dashed lines indicate the back end of the concrete plug and the frontal part of the heater (see also Figure 9).

© Modern2020

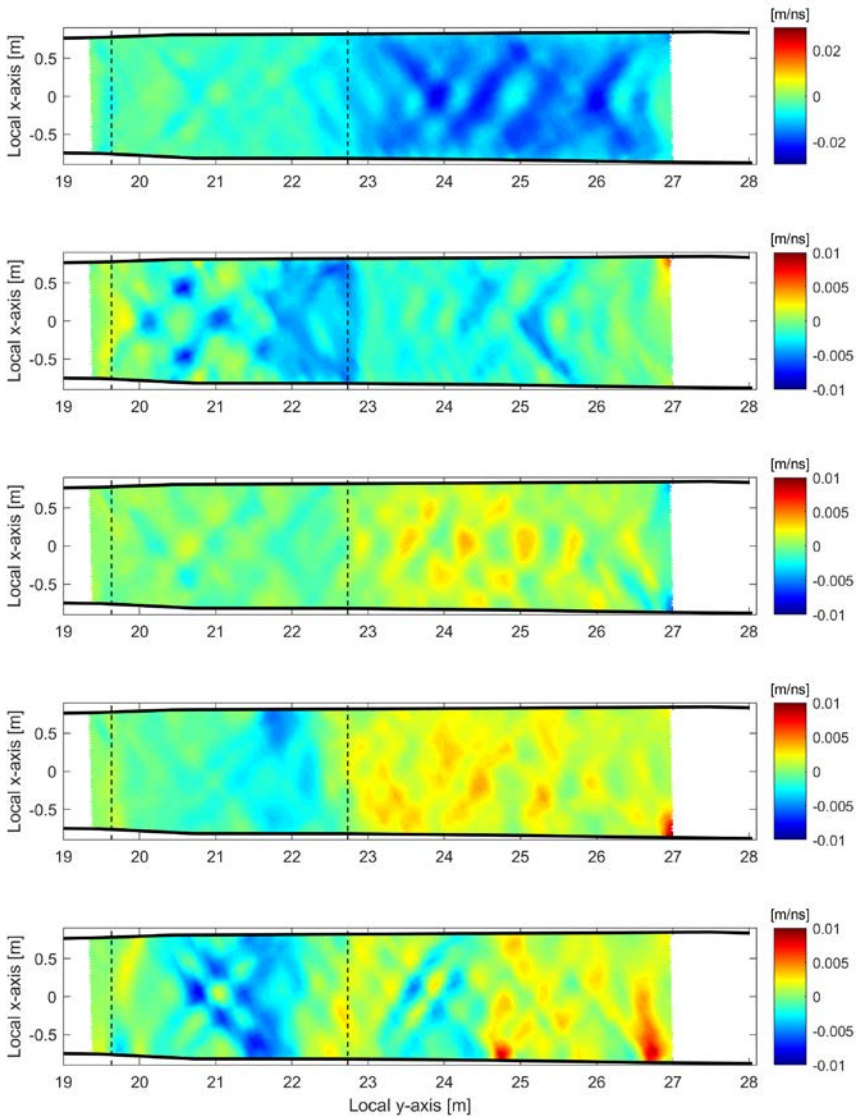

Figure 11. Consecutive differential GPR tomograms for the six experiments carried out so far (first row: exp. 2 – exp1, second row: exp 3 – exp 2, etc.). Note that the colorbar for the differences of the first two experiments is different from the other colorbars. The distances indicated above the tomograms correspond to the y-axis of the local coordinate system. The vertical dashed lines indicate the back end of the concrete plug and the frontal part of the heater (see also Figure 9).

3.4 Discussion, conclusions and outlook

We developed a novel procedure for determining high precision and highly consistent GPR traveltime data, with which the potential of double-difference tomography can be fully exploited. Furthermore, we proposed a refinement technique that allows redundant differential tomograms to be made more consistent. Both procedures do not only lead to improvements of the accuracy of the results, but they also offer powerful means for identifying data glitches and problematic areas in the differential tomograms. Our data refinement procedure is restricted to waveform data (i.e. GPR and seismics), but the differential refinement procedure can be applied to any inversion type during a post-processing step.

On the basis of these results, a possible roadmap for future research towards non-invasive monitoring with seismic FWI can be set up as follows.

© Modern2020

1. GPR is not applicable in the presence of a clay host rock, but the transfer of the results to seismic data is relatively straightforward. Both GPR and seismic data are governed by the wave equation. Indeed, there is an exact analogy between the GPR and the visco-acoustic seismic problem Carcione and Cavallini (1995). Only the material properties are different (i.e., electrical vs elastic properties).
2. In this study, only phase information from the GPR waveforms was considered. For performing differential seismic FWI, it will be required to identify a suitable differential measure. The simplest option would include differential seismograms as input data, but the suitability of such an approach needs to be tested in more detail.
3. Transferring the results of the invasive experimental setup to a non-invasive setup is possible. Conceptually, it merely requires the source and receiver boreholes to be placed outside of the repository, but this may cause (at least) two problems. First, the occurrence of anisotropy of the surrounding host rock needs to be considered (see section on anisotropic FWI). Second, the material within the repository exhibits likely lower velocities than the surrounding host rock. This may cause illumination problems within the repository. It can be addressed by placing several boreholes around the repository.
4. As already discussed in Section 2, the (geo)physical material properties (propagation velocities, etc.) need to be transferred to quantities with which the integrity of the repository can be assessed (e.g., porosity, moisture content, etc.).

© Modern2020

4. Anomaly Detection (TUL)

4.1 Background information

The anomaly detection algorithm, developed in the framework of this project, is based on image processing and supervised learning. The main aim was to have a supplementary method for the full waveform inversion with the ability to automatically extract the temporal changes from the data and to identify the possible source of the data modification. Such a detection can never replace any full waveform inversion techniques, but it may be useful during the repository monitoring to set the alarm, when the reservoir conditions is modified.

The initial idea was inspired by the application of the computer-aided data analysis in the health systems. For example, in the radiology, the computer-aided analysis in radiology helps to categorize pulmonary nodules in x-ray images into two groups: benign or probably malignant. In this situation it is critical to label correctly all the malignant nodules. If benign node is labeled as malignant, it is later eliminated by the rest of cancer diagnostic process. The computer aided analysis helps to focus only to the potentially malignant situations and it helps to skip majority of the benign nodes.

The repository monitoring is a similar task: all the possibly dangerous conditions must be correctly detected. If a false alarm is set, it can be eliminated by the human supervision. The repository conditions are continually evolving, but as the automated detection is based on supervised machine learning techniques, the algorithm can learn also during the monitoring process each time it sets a false alarm - the situation can be added to the algorithm training set and the classifier can be updated.

The heart of the algorithm is a pre-trained classifier, which is able to distinguish predefined normal and abnormal repository configurations. The methodology was developed and tested using synthetic models and it was verified with one set of experimental data. For the future applications in the repository, the initial real data from the repository would be necessary to adapt the classifier training to the current repository configuration and set up.

The input seismic data are normalized, thresholded and converted into sets of black and white images. The training set of the images is later converted into a feature vector, which is used as the input of the classifier training program. The output is the implementation of the classifier. As a reference, the artificial neural network was implemented to verify the precision of the classifier.

During the past ten years, machine learning and supervised classification has been often applied in the domain of geophysical data processing. With focus on seismology data, we can see the application of artificial neural networks (ANN) as well as the support vector machines (SVM) and other types of the classification methods. A detailed overview of ANN application is given in Diersen et al. (2011). The ANN were used to detect the arrival time of the first break, as event classifiers, or to differentiate the natural earthquakes from human caused explosions (Orlic and Loncaric, 2010). The artificial intelligence was also tested to control or monitor the civil infrastructure (Fisher et al., 2017). Ruano et al. (2014) gives an example of the implementation of the real-time seismic monitoring system based on the multi-layer perceptors and support vector machines. In this case, the task of the monitoring system is to distinguish segments of seismic records containing signals caused by local and regional earthquakes and explosions, from all other situations. The use-case for the repository monitoring is similar: to distinguish the abnormal operating mode from the normal situation.

In the case of repository monitoring, the computer vision or machine learning techniques can be applied to help to distinguish normal and abnormal structures in the acquired data. Either the physical conditions in the repository, such as water saturation or temperature, should remain unchanged, or they should change in a known manner. The data from the early monitoring stage can be used to learn the classifier how the normal operating mode looks like. Atypical changes in the acquired data stream may alarm a problem in the repository – for example, the surrounding barrier may be corrupted and safety of the repository can be endangered. Such situations should be modeled and used in the training process labeled as “anomaly”. If such a situation appears, the classifier should distinguish it from the normal operation mode. The repository itself is strictly defined – it is a structure with defined and well-known

© Modern2020

geometry, with stable homogeneous surrounding. This fact can be very helpful for the supervised learning – the normal operating condition can be sampled and used as the initial training data set.

Even if it is possible to find many successful examples of the application of the machine learning in the seismic data processing, it was not yet tested as a supplementary method for the continuous monitoring of the subsurface area. The main task of the monitoring process is to detect all the possibly hazardous situations in the repository. In the first algorithm design phase, we created several seismic models of repository and we have studied what type of physical parameters can be somehow "visible" in the data as a structure detectable by the computer vision techniques. We have modified several physical parameters of the model. Models created with different water saturation of the tunnel were selected as the initial data for the proof of concept. Using the synthetic data we can verify that the supervised machine learning can be used also for the seismic data sets even if we are not working with images. In the real application the classifier should be trained also using the first acquired data sets of initial normal operation as it was described above. The next step is to select a suitable methodology of the data classification, to run the training and to implement the classification algorithm.

4.2 Methodological Developments

The methodology is based on the idea to use the computer vision techniques to describe the structures in the geophysical data and detect the anomaly using the feature vectors and direct inversion (Kosková and Novák, 2012). The original algorithm was implemented for the gravity field data, and it was tested on predefined set of simple anomaly bodies with different density contrasts. The schema of the original algorithm is depicted in Figure 12.

The contrast gravity body appears in the data as a peak or a depression. The contours of the peak have typical shape, which can be described by its contours. For linear anomaly body we can see linear contours in the data, spherical anomaly body gives spherical contours. To get the shape of the contours the input field data were normalized and thresholded at nine levels to get nine black and white images. Each of the images can contain contrast areas with different shape. If the significant spherical anomaly was in the field, concentric circular shapes should appear at least in half of the BW images.

The algorithm searches through the BW images for the linear and circular shapes in the images, which can be sign of a spherical or cylindrical anomaly body. For all the detected shapes, the algorithm detects it position and quantifies its typical characteristics (such as radius, arc length, mutual angle for linear structures). These values are formed into a numerical vector, which is used as the input of the classifier. Three types of the classification were available: the classification based on the direct inverse calculation, the classifiers based on decision trees (DT) or support vector machines (SVM), and the artificial neural network (ANN).

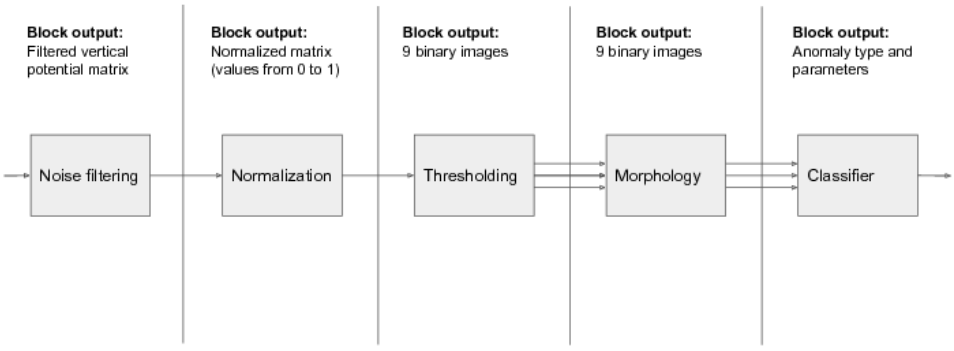

Figure 12. Original algorithm at the beginning of the Modern2020 project

The adaptation of the algorithm and to test, if it can be used also in the repository monitoring required to redefine it for seismic data. As the underlying physical model in seismics is more complex compared

© Modern2020

to gravity, it was decided not to use the direct inverse calculations and to focus on the supervised learning based on the DT and SVM.

The first step of the algorithm implementation was to decide what type of structures should be detected in the data and what is the correct labelling of the data for the supervised training. Several initial synthetic data sets for different configuration of the repository were generated at the beginning of the project. The scenario employed for the tests was adapted from Manukyan (2011). The models contained different tunnel geometry and different water saturation. Finally, it was decided to concentrate on the standard circular shape of the tunnel and detect different water saturation. The data contained a model of the repository, with 10 selected levels of water saturation level (from 0 to 100 %).

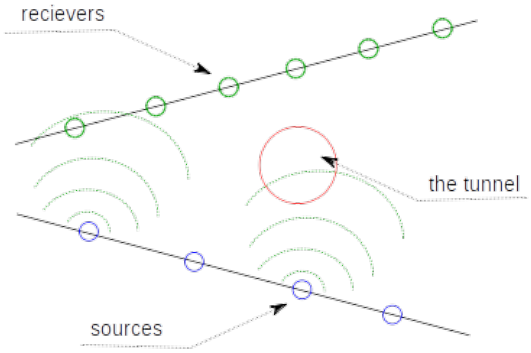

Figure 13. The configuration for the synthetic data set. The tunnel is surrounded by the receiver borehole and sources borehole. The model consists of 113 sources and 104 receivers.

The original cube of data includes all the waveforms as they were detected at the receivers. It was separated and converted to a set of matrices – one matrix contained the image of the waveforms of a single source. This resulted in 113 images of the tunnel for each water saturation. These matrices were normalized from real values to the value range from the interval <0,1>. Normalized data were thresholded at nine levels from 0.1 to 0.9. The thresholded images were binary black and white data. Figure 14 demonstrates the GUI prepared in the Matlab for this phase of development. The GUI was used to define how the structures in the data are related to the model parameters, how it should be described and emphasized. On the left side is depicted a data set with the water saturation set to 10 %, on the right side the water saturation is set to 90 %.

To test a proof of concept it was therefore decided to train the classifier to be able to distinguish between two main model configurations: a “dry” tunnel and a “wet” tunnel. To test the concept, it is not necessary to label the situation as normal or abnormal. It is important to train the classifier correctly to be able to distinguish such two different situations. In the real repository, the tunnels will have low saturation and these tunnels may dry out further. The future user can decide what will be understood as normal or as the configuration, which is to be detected.

© Modern2020

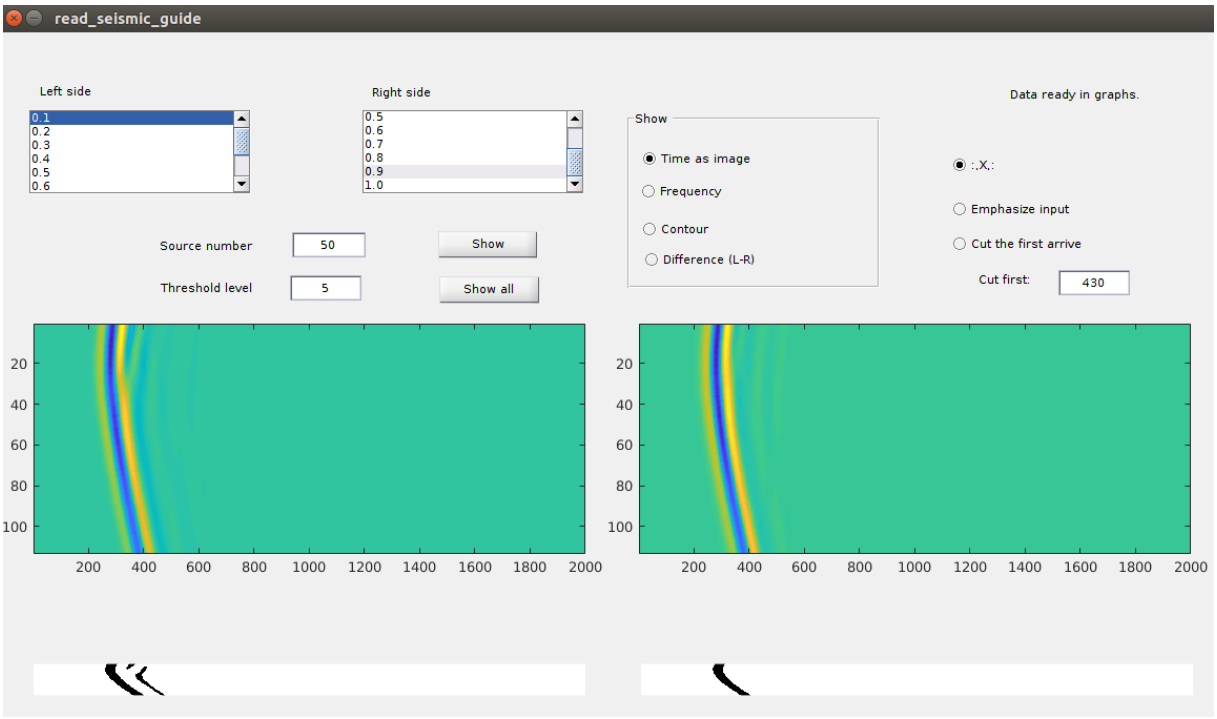

Figure 14 The different structures in the synthetic data. Low water saturation on the left side, high water saturation on the right side. In the middle of the image are depicted the original data, in the lower part are depicted the thresholded normalized data. The number of objects in the thresholded data increases when the water saturation is less than 40 %.

With different water saturation of the tunnel, we can see different number of objects in the thresholded images. Also, the total area of the object is different. Therefore it was decided to create a characteristic vector describing the one concrete situation with following values: [N_{01}, N01, …, N_{09}, S_{01}, S_{02}, …,S_{09}] where N_{0n} is the number of object detected at the threshold level n and S_{0n} is the total area of the objects detected at the threshold level n.

Finally we have created 10x113 characteristics vectors for 113 sources and 10 different water saturations of the tunnel. The images with water saturation lower than 40 % were labeled as “dry”, the other part as “wet”. The “dry” situation in the repository was selected as the “malign” and must be always labeled correctly. These data will set the alarm for further processing and detailed processing. The “wet” situation was labeled as normal and will not be processed. If the wet situation will be false labeled as dry, it should be used to retrain the classifier. The labels can be also set in revers (wet is abnormal, dry normal) and the classifier can be retrained to the new configuration.

Table 1. Training data set and labeling

Water saturation	Label	Explanation	Numerical Label
0 – 40 %	Dry	For the test labeled as abnormal operating condition. This type of data must be always labeled correctly.	0
50 – 100 %	Wet	For the test labeled as normal operating condition in the repository.	1

© Modern2020

The data preprocessing (normalization, thresholding, object detection and labelling) was implemented in Matlab. The data were stored in a Matlab Table structure. The general chain of the data pre-processing is depicted in Figure 15.

The prepared data sets were used to train and verify the classifiers. We have tested the classification decision trees and the support vector machines. We used two different tools dedicated to supervised machine learning: the Classification Learner application from Matlab and our own implementation in Python with support of TensorFlow.

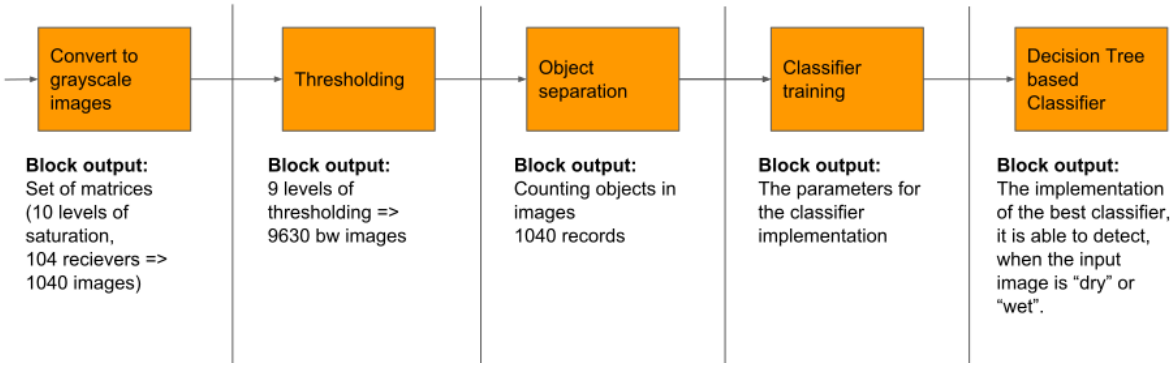

Figure 15 The data preprocessing for the classifier training. Original data are normalized, thresholded, the objects are detected and counted and characteristic vector is created to get the training data.

The decision tree classifier uses a tree structure to predict the responses to the data. The nodes of the tree contain the input features, the leaves of the tree contain the output values. In the node, the input feature are tested and according to the result of the test the decision process selects a next node or a leave. The learning process has to set the test levels to have the best classification. Decision trees are simple classifiers, the learning process is fast, it can be easily implemented and the implementation is not demanding a lot of memory.

Support vector machines (SVM) classify the data by finding the best hyperplane that separates data points of one class from those of the other class. The best hyperplane for an SVM means the one with the largest margin between the two classes. Margin means the maximal width of the slab parallel to the hyperplane that has no interior data points. The SVM is slower compared to decision trees, and it needs more memory, the implementation can be hard for nonlinear SVM types.

The first set of training was done in the Matlab Classification Learner to identify the best fitting classifier structure. The best results were obtained with the fine decision tree using Gini diversity index and maximum number of splits set to 100.

Table 2 summarizes the accuracy of the classification for different classifier types.

© Modern2020

Table 2. The different classifier structures and accuracy of the classification

Classifier type	Fine tree	Medium tree	Coarse tree	SVN linear	SVN quadratic	SVN cubic	SVN Gaussian
Detailed description	Max 100 splits	Max 20 splits	Max 5 splits	Linear kernel	Quadratic kernel	Cubic kernel	Gaussian kernel, scale 0.75
General accuracy of classification	87,3 %	85,5 %	82,9 %	77,8 %	81,1 %	86,9 %	87,7 %

The best results were obtained with fine decision tree and SVN based on fine Gaussian kernel. On the test, the "dry tunnel" scenario was correctly detected in 91 % in the case of Fine decision tree and in 92 % in the case of SVN structure.

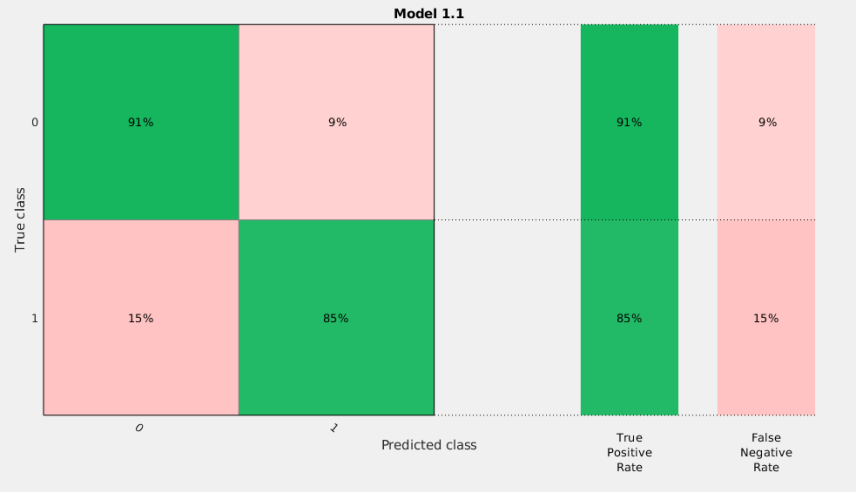

Figure 16 The Matlab classification Learner, Fine decision tree – the resulting confusion matrix.

Figure 17 The Matlab classification Learner, SVM, fine Gaussian kernel – the resulting confusion matrix.

© Modern2020

The next step was the implementation of the algorithms in Python. With the support of Tensor Flow and its libraries, we have implemented and trained the decision tree classifier. We used the same pre-processed data as in the Matlab environment. The general classifier accuracy of our implementation was 88 %. It means that 88 % of the "normal data" were labeled correctly and can be skipped from more detailed interpretation. Only 12 % of the "normal data" will raise the false alarm. Without the classifier, all the data all the data would have to be evaluated and interpreted.

To verify that the data reduction and feature extraction to the characteristics vector was correct, we also used this implementation with the "raw" data. Instead of table of characteristics vectors, we have used the sets of binary thresholded images to train the classifier. In this case, the general accuracy was 85 %. It means that features were extracted correctly and the characteristic vectors contain all the important information.

4.3 Validation with experimental data

4.3.1 Experimental setup

The experimental setup used to get the field data was set in the Bedrichov tunnel locality. From the viewpoint of the deep geological repository development programme in the Czech Republic, the Bedrichov tunnel provides an almost perfect anthropogenic analogue for the study of the processes and changes that might occur within the rock environment in connection with the construction and operation of the country's future deep geological repository. The Bedrichov tunnel is located in the Liberec region, in the village of Bedřichov approximately 5km to the northeast of Liberec and houses a pipe , which connects the Josef mine water retention reservoir with the Bedrichov water treatment plant. The tunnel runs through Liberec and Jizera granite rock environments at a maximum depth of 150m below the surface. According to the Czech deep geological repository development concept, the ideal rock environment for the construction of the Czech repository for radioactive waste consists of a crystalline rock mass.

The experiment was performed by the GImpuls company in February 2019. As the seismics test was not possible at the locality, the electric resistivity tomography (ERT) was selected instead. The data were acquired at the test profile of length 9.4 m with 2 test boreholes. One of the boreholes was filled with bentonite, the second one with foam with blue vitriol to model different conditions in the test borehole.

4.3.2 Description of the experiments performed

The measurement was set according to the ERT methodology with the ARES II equipment, and data were analyzed by the Res2D Inv software. The experiment was done at the 9.4 m profile using the already existing boreholes located close to the ERT profile. One of the boreholes was filled by bentonite, the other were filled by foam with blue vitriol. The blue vitriol is highly conductive and if present in borehole it should be highly contrast in the data. The used boreholes had diameter 5.5 cm and the borehole depth variated from 3.6 to 3.8 m. Boreholes are located about 250 m from the entrance to the Bedrichov tunnel. The experiment setup is illustrated in the Figure 20.

© Modern2020

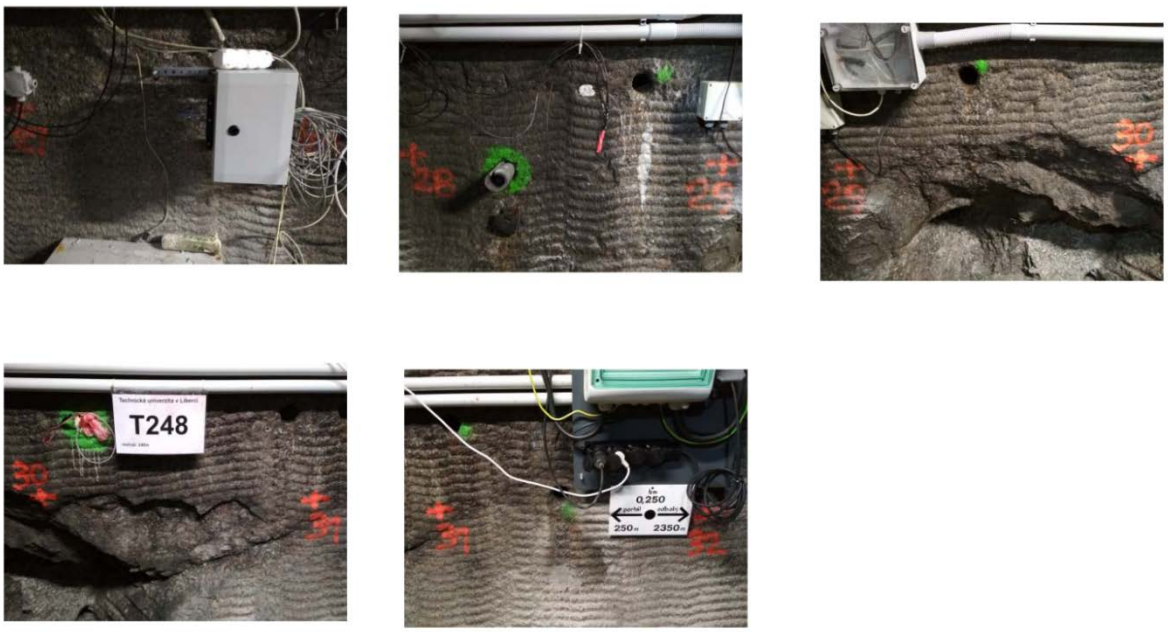

Figure 20 The experiment set up in the Bedrichov tunnel.

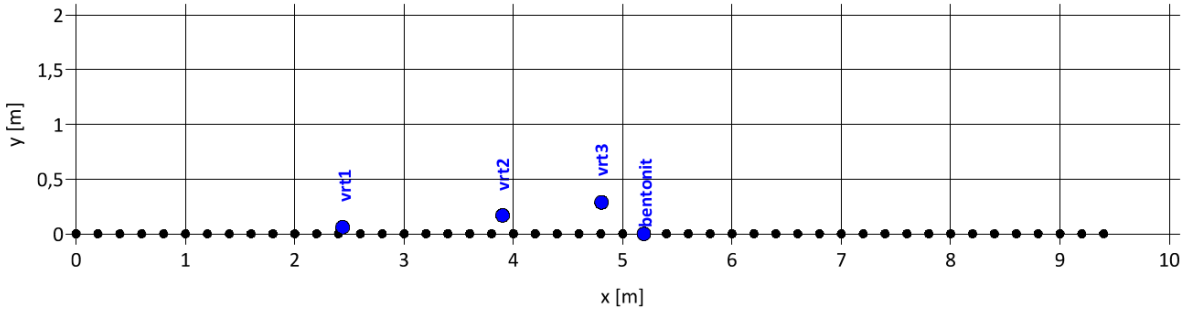

Figure 21 The electrods placement scheme (black dots) with the boreholes (blue dots). The boreholes vrt1, vrt2 and vrt3 were filled with foam, the last one with bentonite.

The experiment ended with 11 different observations:

Observation 1 - 5: All the electrodes in usage, all the boreholes with no fill.

Observation 6 - 9: All the electrodes in usage, one of the boreholes filled with bentonite, other with no fill.

Observation 10: All the electrodes in usage, main borehole with bentonite, vrt 1 filled.

Observation 11: All the electrodes in usage, main borehole with bentonite, vrt 2 filled.

Observation 12: All the electrodes in usage, main borehole with bentonite, vrt 3 filled.

The selected area in the tunnel is the area with rock of extremely high resistance; the highest detected in the Bedrichov tunnel. It results in high demands on reliability of the measuring equipement. The ARES II equipement was operating correctly, but it should be mentioned that such conditions are normally not considered in the geophysical exploration.

The bentonite in the borehole was easily and repeatedly detected. Similarilly the mineralized solution in vrt1 was easily detected in the observation 9. It is surprising that the mineralized solution immediatelly contaminated the surroundings of the vrt1 borehole and therefore the borehole was visible in the Observation 10 and 11 when it was not filled. Similar detection was also in the case of vrt3. The vrt2 is not so distinct in the data. With high probability is the borehole of vrt2 situated in the ideally compacted rock and the solution did not penetrate so fast into the borehole surroundings.

Relatively slender boreholes filled by the conductive environment are easily detectable, but the final detection in the interpretation models is limited by the electrode spacing and the internal mathematical model of the software Res2D used to process the data.

© Modern2020

The data from the measurement will be used to train the classifier. Unfortunately, due to delays with the organization and final set up of the experiments, the data were available at the end of February 2019. It takes time to adapt the classifier ant to retrain it, so the results will be available in May 2019.

4.4 Discussion and conclusions

The main task was to find an algorithm, which can detect characteristic structures in the monitored data and can swiftly distinguish the normal and abnormal situation in the repository.

We proposed a methodology how to pre-process the seismic data, how to create the characteristic vectors and how to set up classifiers. As it was stated at the beginning of the research, such detection will never replace full waveform inversion, but it can be used as a supplementary method to rise an alarm, when abnormal situation occurs in the monitored area. The algorithm is able to classify the configurations for which it is trained. If completely different abnormal configuration will appear during monitoring, the classifier may not record it. Therefore, it is very important to retrain the classifier with all the false alarms it may rise to learn it new normal situation to keep it adapted to the current situations in the repository.

The implementation of the novel development in practice would require getting the initial training data from real location with different repository configuration. The training data should be used to train the classifier.

Because the training data set was not big, we have given priority to the supervised learning with classifiers. If the real monitoring application would offer bigger training data set, with the same data preprocessing the ANN can be used for classification as well.

© Modern2020

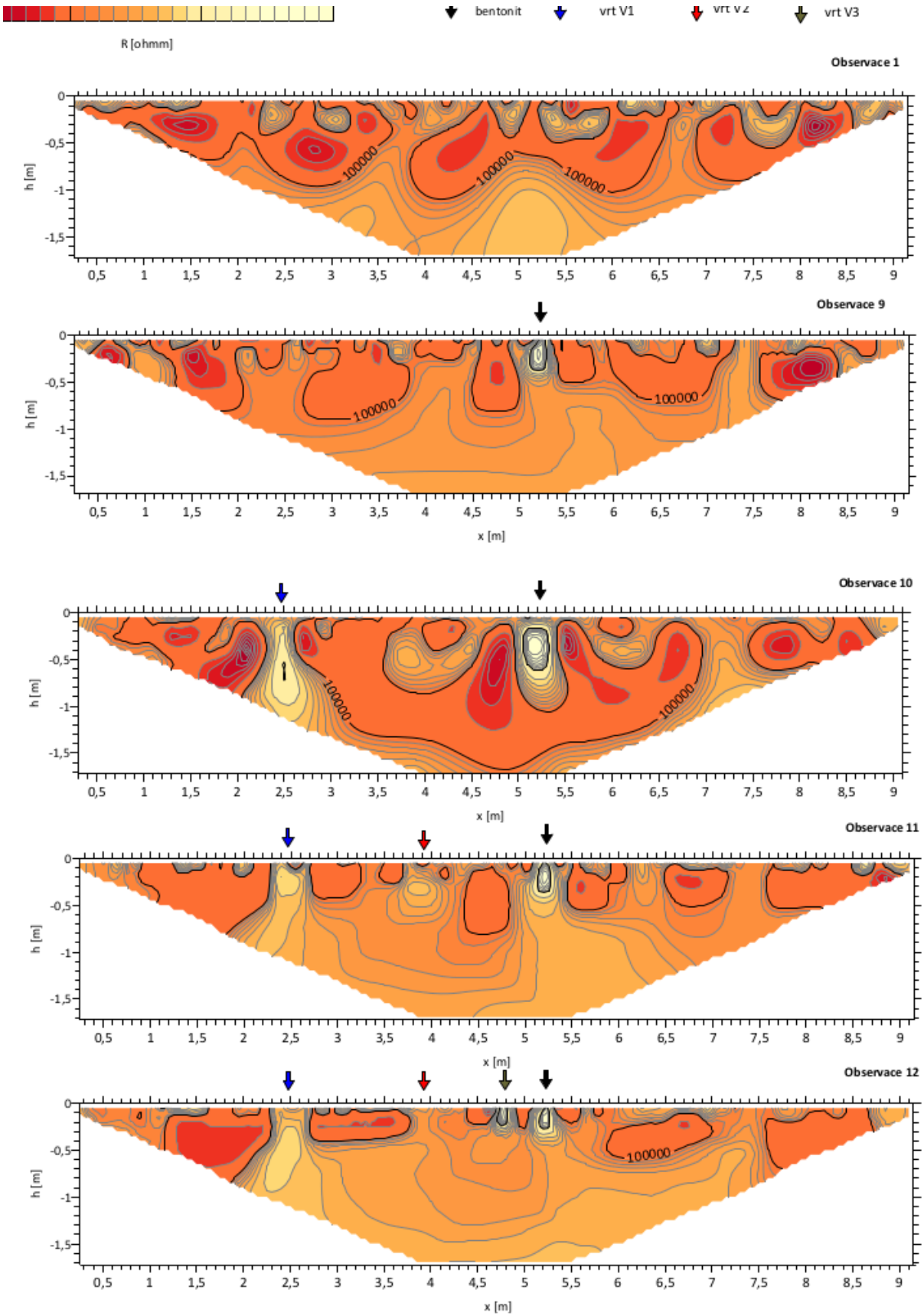

Figure 22: The Res2D interpretations of the acquired data. The Observation 1 shows no boreholes, the bentonite borehole is visible in all the Observation 9-12, the vrt1 is visible in the Observation 9 to 12, the vrt2 is visible in Observation 11 and 12, the vrt3 is visible only in Observation 12.

© Modern2020

5. Geoelectric and Induced Polarization Tomography (VTT)

5.1 Background information

Electrical resistivity tomography (ERT) is a widely proven and robust method of characterizing subsurface structure and monitoring subsurface hydrological, thermal and geochemical changes for geological, geotechnical, hydrological and environmental applications. The monitoring natural or artificially induced changes in resistivity can often provide valuable information about flow and transport processes. Recent advancements in data collection hardware and imaging software enabled ERT to become practical for variable scale 3D characterization and high-resolution 4D monitoring applications. The sensitivity of subsurface electrical conductivity to a number of important hydrogeological, geochemical and geotechnical parameters indicates the potential of ERT to provide non-destructive and often non-intrusive information.

Induced polarization (IP) measurements and induced polarization tomography (IPT) can be measured simultaneously and parallel with direct-current (DC) resistivity in time-domain ERT surveys. The IP mechanism can be described as a charge-up effect. When cutting off the injected current the voltage does not drop to zero immediately but persists for some time with a continuously decreasing magnitude (the current OFF parts in the measured full waveform time-domain potential signals). Correspondingly, the voltage between the electrodes does not reach its maximum value immediately after the current is switched on but instead increases steadily towards the maximum for several seconds or minutes (the current ON parts in the measured full waveform time-domain potential signals). The IP method can be employed in the time domain or the frequency domain. Electronically speaking, this IP effect in the time domain resembles the charging and discharging of a capacitor. In the frequency domain, the **IP** effect is like the variation of the impedance of a circuit including a resistance and a capacitance in parallel for an alternating current (Parasnis, 2012).

The IP measurements are sensitive to additional electrical parameters, such as chargeability. Low-frequency (below 1 kHz) induced polarization is caused by the transport and accumulation of charge carriers (ions and electrons) in micro-heterogeneous materials (e.g., rock or soil) due to an external electric field. Induced polarization phenomena can be observed both in time and in the frequency domain. The main mechanisms that typically dominate polarizations at frequencies below 1 kHz and in the absence of disseminated conductive minerals are polarization of the Stern layer, i.e., the inner part of the electrical double layer (EDL) at the interface between minerals and water (Revil et al., 2012), and membrane polarization (e.g., Vinegar and Waxman, 1984). Revil (2012) has indicated that the diffuse layer is not the main contributor to low-frequency polarization of clayey materials and that the Maxwell–Wagner polarization is not the dominating mechanism of polarization at intermediate frequencies. The strong relationship between IP parameters and structural properties (e.g. specific surface area, clay concentration), coupled with relatively low sensitivity of these parameters to fluid chemistry, provides often ambiguity in the interpretation of ERT and IP results. For example, the chargeabilities computed using time-domain IP measurements are largely controlled by the surface area and they are only weakly dependent on fluid chemistry (Mwakanyamale et al., 2012).

The use of ERT and IPT in the geotechnical/civil engineering and environmental site investigation studies has been increasing all over the world. They are convenient methods for evaluating spatial and temporal variations of moisture and heterogeneity of geological structures. Recently, quantification of geotechnical properties has become an important issue in engineering applications. The correlations of different geotechnical and/or geochemical properties with ERT are closing the gap that exists between geophysical volume imaging and geotechnical and/or geochemical point (i.e. only at key locations) sampling, testing and drilling.

During the past 7 years, VTT has tested and applied ERT in monitoring water content changes and structural integrity in various scales in the lab and the field experiments related to deep geological

© Modern2020

disposal of high-level nuclear waste. Non-destructive, tomographic ERT studies have been applied to monitor electrical conductivity distributions and changes in the buffer and backfill bentonite using 3D electrode chains embedded into the boreholes in the crystalline bedrock, bentonite-crystalline bedrock interfaces, tunnel floors, rock-buffer-backfill materials etc. The electrical conductivity of compacted bentonite blocks and bentonite pellets is influenced by the porosity, dry unit weight, pore water (gravimetric water content, degree of saturation and volumetric water content), as well as pore water salinity. It is found that for high water salinities, the electrical conductivity is most significantly related to the volumetric water content. The high electrical conductivity of injected salt solution has only little effect on changes of the bulk resistivity of the bentonite blocks or pellets for water contents between 30 and 80 % (Rahimi and Siddiqua, 2018).

Over the past years, ERT and IPT survey instrumentation advanced rapidly, enabling large amounts of data to be collected quickly and autonomously, and providing the opportunity to characterize the subsurface and monitor subsurface properties at high resolution in space and time. Even the full waveform acquisition in the field applications is possible. ERT has developed from a slow procedure of manually measuring point by point to rapid multi-channel data acquisition using automatic multi-electrode systems. The development in computational power has allowed for more efficient processing and imaging-inversion of data, which has been encouraging for investigations with large amounts of data, such as three-dimensional investigations and repeated measurements.

In the Modern2020 project, VTT has developed time-lapse (4D) inversion and conceptualization processes with and without petrophysical and thermo-hydro-chemical constraints. Furthermore, measuring and signal processing protocols for simultaneous ERT and IPT imaging of the canister-buffer-bedrock systems were established.

The overall goal was to develop the IPT algorithms for the whole time-domain, on-time portions of the time-domain “spectral” full waveform potential recordings. These inversions can be carried out simultaneously with the ERT data. The IPT information is picked as resistances against frequency from the current ON measured full waveform time-domain potential signals. In this way we can apply the same geologically-structurally constrained 3D/4D inversion process to IP responses as is used to invert the resistivity changes. On-time signals have a little better signal-to-noise ratio than off-time information (Olsson et al., 2015). We have also develop data processing algorithms for identifying and removing noise, signal spikes and the self-potential drift from the full-waveform recordings of measured potentials in order to increase the signal-to-noise ratio and thus widen the spectral time-lapse information (Olsson et al., 2016).

The difference inversion method (described more detailed in the Section 5.2.2 below) was applied for the inversion of both the time-lapse resistivity and IP monitoring measurements. The difference inversion method inverts the difference between monitoring and the baseline datasets and uses the baseline or previous monitoring model as the priori model. The primary advantage of this method is that the effects of systematic and coherent noise are mitigated so that fewer inversion artefacts are shown on the difference images.

In the Modern2020 project, the IPT algorithms together with time-lapse ERT were tested in a laboratory column filled with bentonite pellets. The information from this kind of small scale test can be adapted and scaled to the future full-scale experiments with monitoring of bentonite blocks and pellets in deposition holes and deposition tunnels.

© Modern2020

5.2 Methodological Developments

5.2.1 3D ERT/IPT inversions

The idea of the time-lapse (repeated) measurements is to use the same fixed network of electrodes and use exactly the same measurement protocol for all monitoring cycles. Either the initial data set or the previous data set can be used to constrain the inversion of the later time data sets so as to minimize changes in the model resistivity that are unlikely to be due to actual changes.

The 3D modelling and inversion software DCIP3D was used for the image reconstruction (inversion) of the field data. This software, which was developed by the University of British Columbia's (UBC), Geophysical Inversion Facility (GIF), enables the forward modelling and inversion of resistivity of 3D subsurface models. The software can handle buried electrodes and even combined surface-downhole datasets. DCIP3D is particularly useful, when applied together with the time-lapse modules developed at VTT. Using DCIP3D with the time-lapse modules allows the inversion of repeat datasets with the resistivity distribution either recovered from the baseline or preceding monitoring result as starting model. The data can be depicted as 3D resistivity distributions as well as resistivities normalized by the reference resistivity field in order to better understand the effects associated with the dynamic (i.e. saturation, salinity or temperature) changes. The time-lapse approach has the benefit of suppressing features that are unrelated to the fluid migration process, but that maybe of sufficient size and magnitude to obscure the moisture signatures in the datasets. UBC-GIF recently released a substantial upgrade DCIP3D forward modelling and inversion programs. Enhancements allow users to save time and run efficiently on large-scale problems with multi-processor capability. The new versions provide increased capability to incorporate geologic information via a multicomponent regularisation function, the reference model, petrophysical constraints, and use of active and inactive cells. The DCIP3D library works with data acquired using general electrode configurations and arbitrary observation locations either on the surface, inside the structures or in boreholes.

We developed three alternative procedures for time-lapse inversions. Prior information can be incorporated via regularization with respect to a reference model according to three basic protocols: 1. independent regularization involving a single reference model, 2. background regularization involving a reference model obtained via inversion of pre-injection data, and 3. time-lapse regularization involving an evolving reference model obtained via inversion of data from previous experimental stages.

The first step of the time-lapse inversion strategy applied is to obtain background (and initial) models of the logarithm of electrical resistivity (m0) by inverting data sets acquired prior to any perturbations. Here, a damped least-squares constraint is used to minimize the differences in the model resistivity values between the reference model (i.e. the conceptual pellet model) and the time-lapse model and simultaneously to recover a model, which acceptably reproduces field observed data. The inversion then proceeds iteratively by decreasing the weight that penalizes deviations until the residuals are as small as the assumed data errors. Our tests using models from the previous time step as background models started to give inferior results, as the numerical artefacts started to accumulate at previously occupied positions of the wetting fronts.

For the IP inversion, chargeability distributions were obtained for lower frequency resistances using the same procedure as in the resistivity inversions, but an evolving reference model was applied and higher resistivity distributions via the corresponding lower frequency resistivity distribution as the starting model. Variation of time-lapse data due to a IP/transient process may be smaller (<1% variation of e.g., lower and higher frequency apparent resistivities) than the total error of the data set. Inverting each such data set independently would not always resolve the IP/transient changes.

© Modern2020

5.2.2 Time lapse inversions

Considering different types of error sources and the correlation between errors of the different time-lapse data sets can help to improve significantly time-lapse inversion results (Doetsch, 2011). A data set $\mathbf{d}_i$ recorded at time step i is typically expressed as:

$$\mathbf{d}_i = g(\mathbf{m}_i) + \mathbf{e}_s + \mathbf{e}_n + \mathbf{e}_{ri} \quad (7.1)$$

where g is the forward operator that calculates the response of the model $\mathbf{m}_i$ with errors being distributed as static $\mathbf{e}_s$, numerical $\mathbf{e}_n$ and random e_{ri} contributions. It is assumed that e_s is common and same for all time-lapse data. The numerical errors $\mathbf{e}_n$ refer to numerical errors introduced due to an imperfect forward operator. They can be assumed to be similar for all models, as long as the models do not change significantly during the time-lapse inversion process. The random errors $\mathbf{e}_{ri}$ correspond to the random observational errors that vary between time-lapse data sets.

One common means of removing the effects of $\mathbf{e}_s$ and $\mathbf{e}_n$ is the difference inversion approach of LaBrecque and Yang (2001), which was successfully applied by Kemna et al. (2002). This inversion option has been also applied in this study. In the difference inversion approach the inverted input data used is the sum of the subtracted observed and *a priori* background data vector and the theoretical background data vector calculated for the inverted background model:

$$\mathbf{d}_i = \mathbf{d} - \mathbf{d}_0 + g(\mathbf{m}_0) = g(\mathbf{m}_i) + \mathbf{e}_{ri} - \mathbf{e}_{r0}, \quad (7.2)$$

where $\mathbf{e}_s$ and $\mathbf{e}_n$ from the two data sets cancel.

In the approach, starting from the background model $\mathbf{m}_0$, one typically uses the difference inversion data $\mathbf{d}_i$ (equation 7.2) to invert for the model update. The convergence is fast since the inversion routine needs only to find small perturbations about the good initial guess. Systematic errors, such as those due to errors in field configuration and discretization errors in the forward modelling algorithm, tend to cancel and the result is often that we can fit the difference data more closely than the individual potentials – the better resolution with fewer inversion artefacts.

5.3 Validation with experimental data

5.3.1 Experimental setup

In the monitoring-inversion experiment a transparent laboratory column (a plexiglass tube of 20 cm inner diameter and 80 cm height) was filled up to the 55 cm level with bentonite pellets (Figure 20). These roller compacted pellets have an initial water content of about 16% and were made by Hosokawa Bepex in Germany. The raw material for these pellets was MX-80 bentonite and they have been used in underground in-situ Buffer test trials done by Posiva-in the ONKALO underground research and characterisation facility (Marjavaara et al., 2013). The saline water was injected at intervals from the same injection point into the pellet filling. The salinity of the injected water was 10g/kg (typical salinity for the groundwater in the Finnish repository depths and typical salinity used in ONKALO *in situ* tests).

The electrode layout consists of four sets of vertical electrode chains (Figure 20). Each vertical line included 16 electrodes and each vertical level includes a symmetrically arranged four-electrode quadrupole. Vertical electrode spacing was 4 cm and the electrode lines were named as T1, T2, T3 and

© Modern2020

T4. The water injection point was in the middle of the electrode lines T1 and T2 on the height level of 21 cm. The ERT monitoring that covered the whole test period and was carried out using all 64 electrodes. The near electrode surroundings were dry in the beginning of the test.

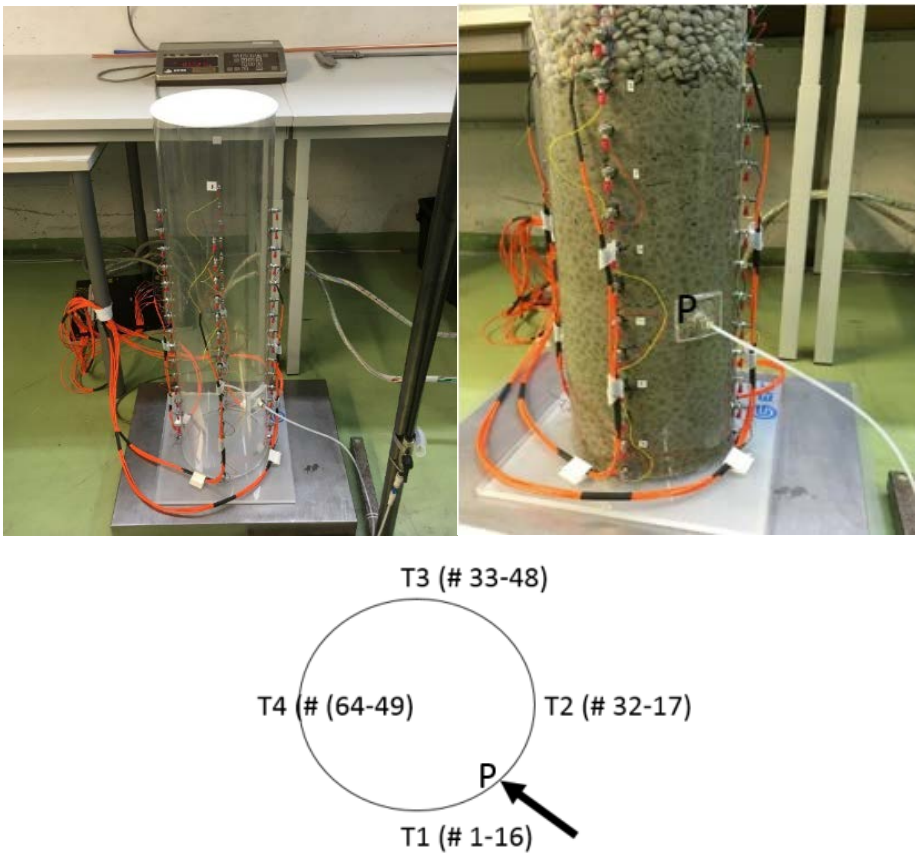

Figure 18. The test column with the locations of vertical electrode chains T1, T2, T3 and T4 as well as numbering of 64 electrodes and the location of the injection point P between T1 and T2.

The idea of the time-lapse (4D) surveys is to conduct repeated measurements over the same fixed network of electrodes and using exactly the same measurement protocol at different times. Repeated Electrical Resistivity Tomography (ERT) measurements were then used to map non-destructively in 3D the progress of infiltration fronts and water content changes. The test was carried out between 26.4.2017 and 18.6.2017. Repeated measurements offer a method to monitor both temporal and spatial resistivity changes (caused for example by water content, temperature or salinity variations).

The automatic monitoring protocol was programmed to repeat the measurements in the interval of 12 hours. The first monitoring was timed to start daily at 8 am and the second at 8 pm. Each single monitoring cycle consisted of 1,304 four-electrode potential-current measurements and took about one and half hours. Thus, each successive monitoring result reflects the moisture changes that happened during the previous one and half hours (the interval between identical four electrode resistance measurements is exactly 12 hours). The first measurement was made on 26.4.2017 at 8 am and the final monitoring ended at 8 pm on 18.6.2017. The salt solution was injected six times (27.4, 28.4, 30.4, 2.5, 3.5 and 19.5) in 75-100 minute intervals into the column. Each time 1,000 g of water was injected (Figure 21).

© Modern2020

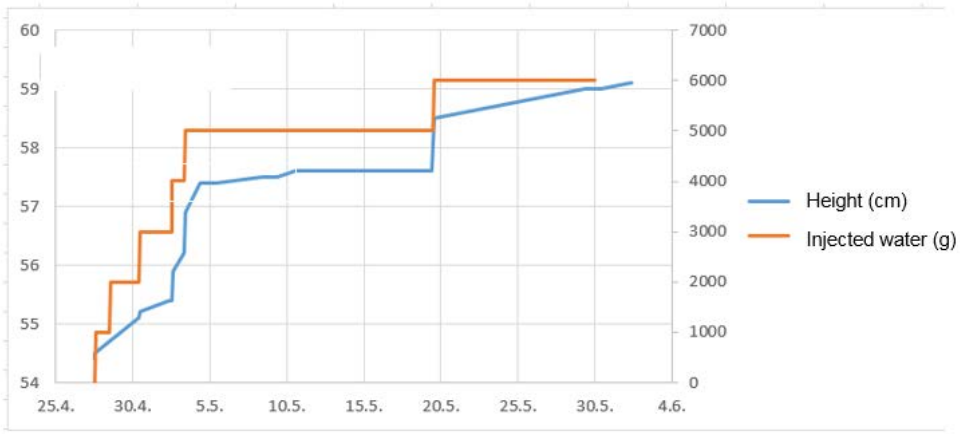

Figure 19. The water injection periods and the corresponding water level heights.

The ABEM Terrameter LS (where LS stands for Lund Imaging System) was used for the measurements. This instrument can also be applied in the field and it continuously adapts the output voltage to keep a constant current with an accuracy of 0.4 % (https://www.guidelinegeo.com/product/abem-terrameter-ls-2/), and together with its capability of full-waveform acquisition is particularly well suited for the combined electrical resistivity and on-time IP monitoring. The system integrates receiver, transmitter, electrode selector and computer units. It has 12-high resolution measuring channels based on 24 bit sigma-delta AD converters, plus two additional measuring channels for monitoring the transmitter. The maximum transmitter output is 600 V or 2500 mA for a maximum power of 250 W. This instrument can also record the transmitted and received signals with 1 ms sampling interval. A measurement cycles up to 4 second current transmission was used. The system can be programmed for automatic measuring at pre-selected intervals and includes also remote control possibility and support via Ethernet. Built in relay-switch and built in processors allow programming of own monitoring protocols. The instrument has a built-in relay switch that handles 64 electrodes, but it can be expanded with a number of Electrode Selector ES10-64C relay switches to allow for more electrodes. The electrode layouts are defined in so-called spread files that define the type of measurement setup (e.g. 2D surface layouts, 3D grids, borehole cables, etc). The measurement sequences are specified in protocol files that can be designed for arbitrary measurement arrays. An arbitrary number of spread and protocol combinations can be combined to run sequentially to cover for example different parts of a monitored site. The instrument software runs on a Linux platform. The timing of the data acquisition is controlled by the standard scheduling feature Cron. Each time it is due, Cron starts up acquisition software and carries out measurements according to the selected spread(s) and protocol(s). Automatic data transfer can also be started this way. After finishing a measurement round the instrument turns off the software and all data acquisition hardware, which means that the power consumption in stand-by mode is minimised. Although no PC is needed for the monitoring when using Terrameter LS it is often an advantage to use a PC for more stable remote control and data transfer. Power supply was so far provided by car batteries and the battery power was kept through the experiment using mains current. The system can be optimised for minimum power consumption via standby mode between measurements for installations where power consumption is provided by e.g. batteries, fuel cells or solar panels. Adjusting output power and optimising the measuring protocol to reduce the number of current transmissions by using the multi-channel capability are other ways to save energy.

In this experiment, we applied a multi-gradient protocol (Dahlin and Zhou, 2006) in programming the 1,304 measured dipole-dipole pairs with 64 electrodes. In this array the current electrode pair is placed on the two outer electrodes of the basic four-electrode setup, and the voltage is measured on the inner pair. In addition to the automatic multi-gradient monitoring the Wenner measurements were also carried out along the vertical electrode chains as well as cross each horizontal level. The progression of measurements occurs by changing one current electrode forward along the array and then measuring all

© Modern2020

adjacent voltage pairs inside the current pair. When the current electrode reaches the end of each transect the other current electrode at the beginning of the electrode chain moves forward incrementally and voltage is measured again on all adjacent electrode pairs. The advantages of the gradient array are the large number of measurements and its effective use of the number of available channels on a multi-channelled resistivity meter. We planned the gradient array so that it tries to use when possible separated cables for transmitting current and measuring potentials to reduce the effect of capacitive coupling and improve the IP data quality (Dahlin and Leroux, 2012). Gradient Protocol can reduce field time collecting data with up to 75%. The electrode contact resistance was measured for all electrodes once a day.

The noise level of the measurements was estimated by comparing now and then the actual measurements with their corresponding reciprocal measurements. In the reciprocal measurements, the current and potential electrodes used in the actual measurements are interchanged. This value of noise has been found to represent the true noise level better than using duplicate measurements, which tend to underestimate noise levels. Reciprocal measurements provide the most effective means of assessing data quality and determining reliable and quantitative data editing criteria reciprocal error is particularly effective for assessing error due to high contact resistances, random errors arising from the resistivity instrument and sporadic errors due to background noise. Measurements with a reciprocal error of more than 10% were removed; the remaining reciprocal pairs were averaged prior to inversion.

After acquisition, the data are pre-processed to remove obvious bad measurements, such as negative voltages, extremely high voltages, data with high repeat errors, and so on resulting from random machine errors, bad electrode placements, or poor electrode contacts with the surrounding material. A filter was applied and all measurements with a measured potential smaller than 5 mV (the sensibility limit of the ERT device) and a standard deviation smaller than 3% were neglected. The quality of the data was good, because less than 10 out of 1,034 measurements per monitoring were neglected. The data quality improved significantly during the test because more and more electrode surroundings were wetted due to the water injection.

For the inversion process, the finite element mesh has to be adapted to the electrode array. As an example, the 3D conceptualization volume with the inverted snapshot example for the column experiment is presented in Figure 22**Error! Reference source not found.**. The pixel volume used was 2 cm x 2 cm x 2 cm. A homogeneous reference/starting resistivity model was used for the bentonite pellet volume.

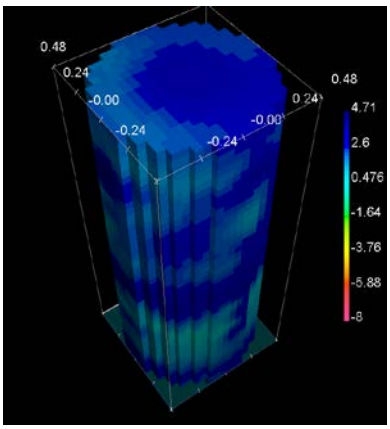

Figure 20. The conceptualization model for the inversion processes.

5.3.2 Results

The primary results of the ERT test are the 3D resistivity distributions that are calculated for each single monitoring. These results are typically studied as 2D vertical and horizontal slices that are cut from the

© Modern2020

3D models or in 3D as selected color contours. The other alternative is to present results as 2D rectangular surfaces as a function of distance from the center of the cylinder structure. Slices are here presented as absolute resistivities.

In the Figure 21, the 3D inversion results from the first 8 days of monitoring (one result per day) are presented as the 2D vertical and horizontal cross-sections. In the 2D snapshots, the vertical presentation plane goes through the center line as well as through T1 and T3 electrode chains and in the horizontal level example the resistivity distribution is sliced from the 3D distribution from the column height of 41 cm are presented. The water injection point is located on the column height level of 21 cm.

The results of the resistivity distributions seem to be rather stable between the measurements and the progress of the wetting front can be traced during the injection periods (27/04-3/05). During the longer non-injection period (3/05-19/05) the changes in the resistivity distribution are small as expected.

From the 2D rectangular outer surface presentations (Figure 22) the progress of the water content changes around the column cylinder can clearly be followed (only results from the main injection period are selected and presented).

© Modern2020

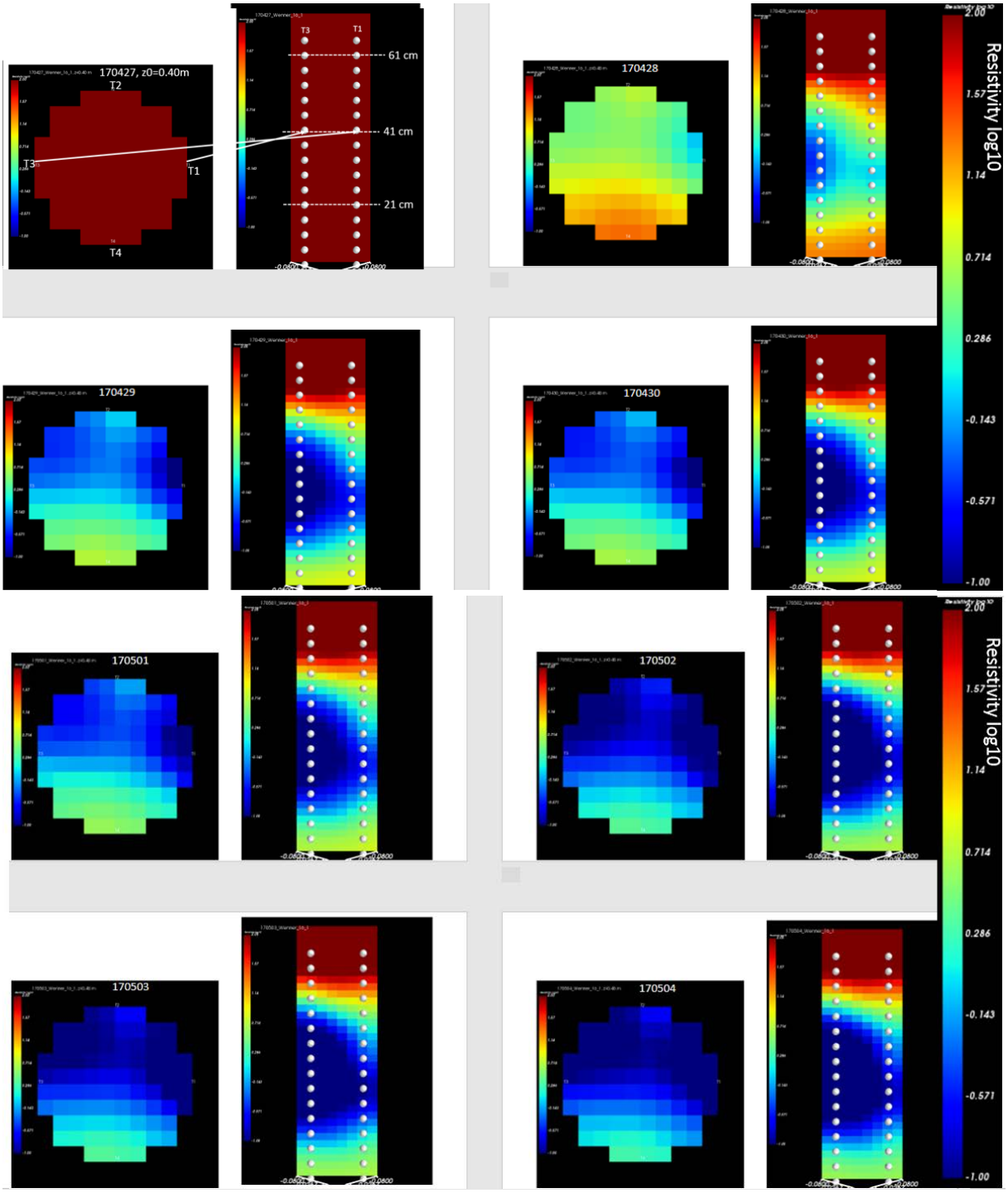
170427, z0=0.40m
T2
T3
T1
T4
T3
T1
61 cm
41 cm
21 cm
170428
Resistivity log10
2.00
1.57
1.14
0.714
0.286
-0.143
-0.571
-1.00
170429
170430
170501
170502
170503
170504

© Modern2020

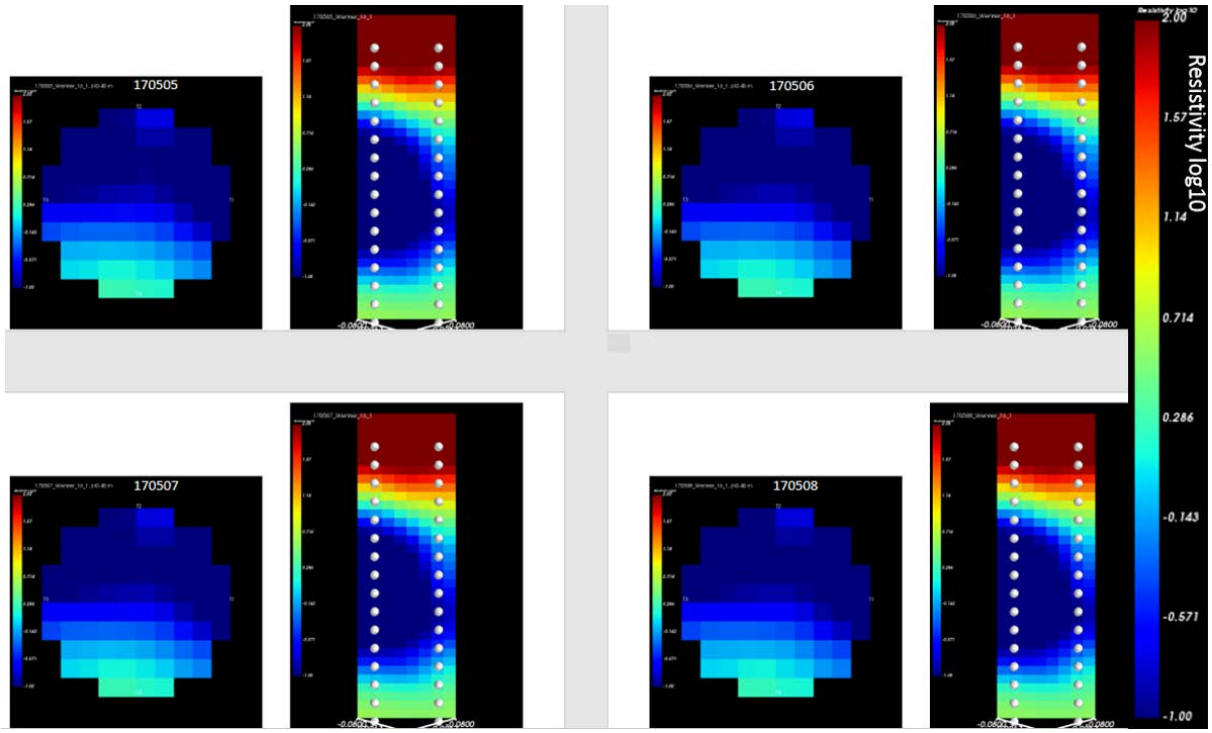

Figure 21. The presentation of 3D resistivity results bot as the the horizontal height level of 41 cm and as a vertical cross-section through vertical electrode chains T1 and T3. daily snapshots between 28/04 and 8/05.

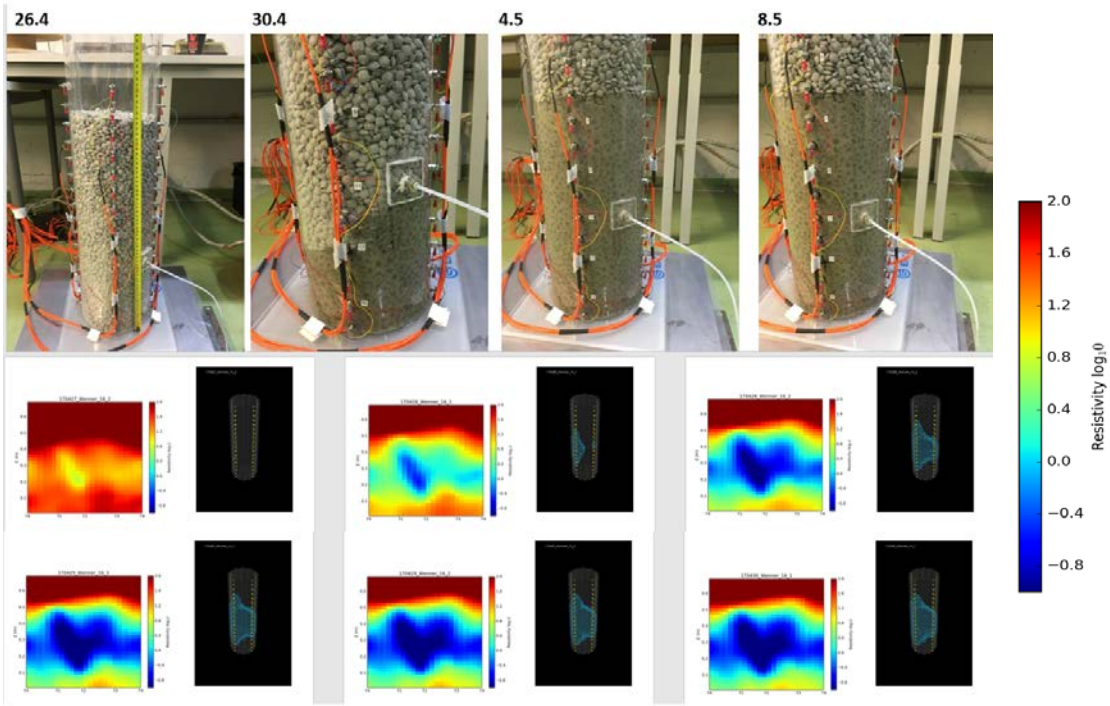

Figure 22. The 3D resistivity results for the beginning of water injection period presented as daily snapshots. These daily snapshots are presented as 2D rectangular surfaces representing the outer volume the cylinder structure.

© Modern2020

The water content was measured in some points after dismantling of the experiment and related to the measured resistivity. The results are collected into the Figure 23. The water content information correlated well with the final 3D resistivity distribution. Electrodes are arranged in 16 evenly spaced vertical levels and each vertical level includes a symmetrically arranged four-electrode quadrupole. The time-series of resistivities from the horizontal Wenner measurements for the selected vertical levels (the level number 1 is the highest and the level number 16 the lowest level in the column) are also presented in the Figure 24. These resistivity-water content values follow the same trends that are reported for bentonite pellets and compacted bentonite blocks elsewhere for the similar saline water concentrations and temperatures (e.g., Rahimi and Siddiqua, 2018).

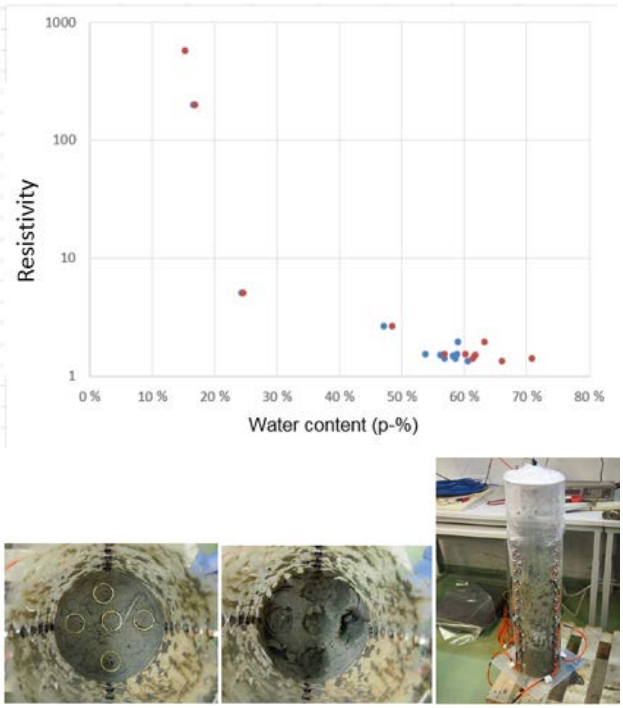

Figure 23. The water contents analysed from the final 18.6 structure are presented together with resistivities for the sampled layers.

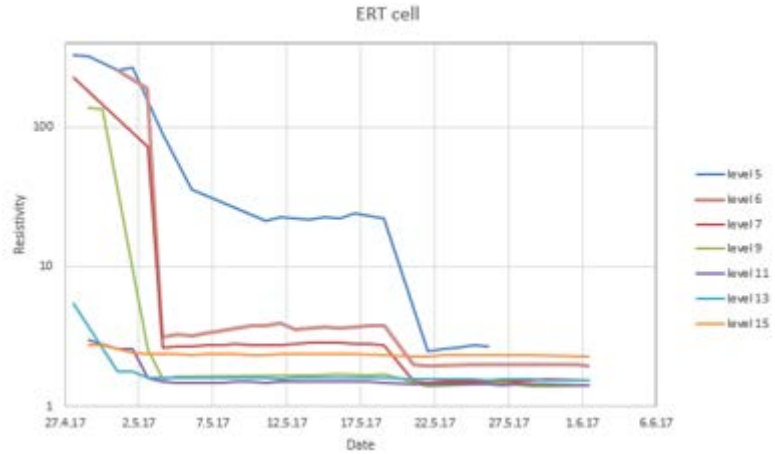

Figure 24. Resistivities calculated from the horizontal Wenner measurements for the selected vertical levels.

© Modern2020

From the pictures of

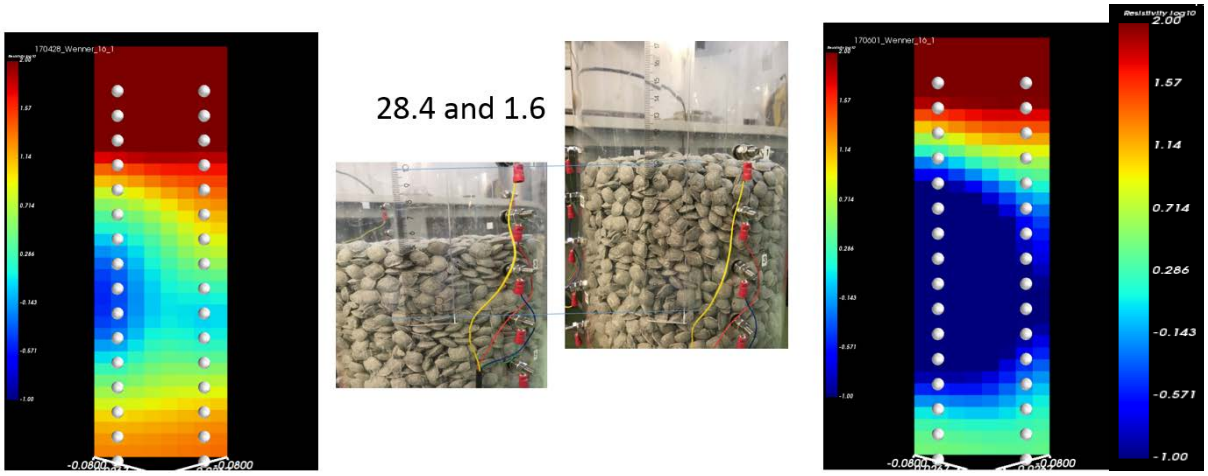

Figure 25, the rise of the upper surface of the pellet filling during the test can be seen clearly. The same rise can be traced from the decreased resistivity levels around the highest electrodes in the vertical cross-section results through vertical center line and through T1 and T3 electrode lines.

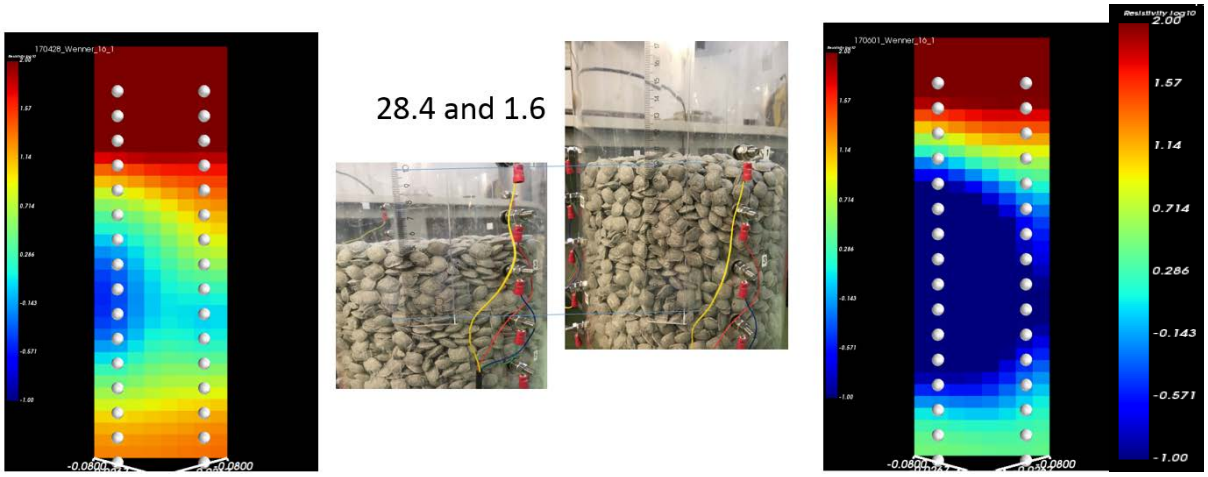

Figure 25. The vertical swelling caused the rise of the upper surface. This rise was around 5 cm between 28/04 and 1/06. and the rise can also be traced from the decreased resistivity levels around the highest electrodes in the vertical cross-section results between T1 and T3 electrode lines.

The percent frequency effect (PFE) distributions (PFE is calculated as the percentage of the remainder of low and high frequency resistivities divided by the high frequency resistivity) are presented as vertical cross-section between electrode chains T1 and T3 in Figure 26 and for the horizontal cross-section of the height of 5 cm. Time-lapse information is presented from the beginning of test (28.4-10.5). In Figure 27, PFE results are presented for the second lowest level (15) as horizontal cross-sections. The PFE seems to follow the progress of the saline water effects in the same way as ERT, but PFE anomalies seem to appear little later.

The PFE inversion process seems to be rather stable. The results show, as expected, that in the bentonite pellet-saline water environment the polarization effects are small due to the homogeneous high clay content material and high conductivity (high salinity and water contents). It can also be recognized that care must be taken in collecting time-domain field measurements designed to replicate frequency-domain laboratory measurements. In the situation where signal-to-noise ratio is high enough to map

© Modern2020

polarization effects, IP data will provide insight into changes electrochemical properties and/or in structures and can be useful in conditioning flow and transport models rather than providing accurate pixel-to-pixel information.

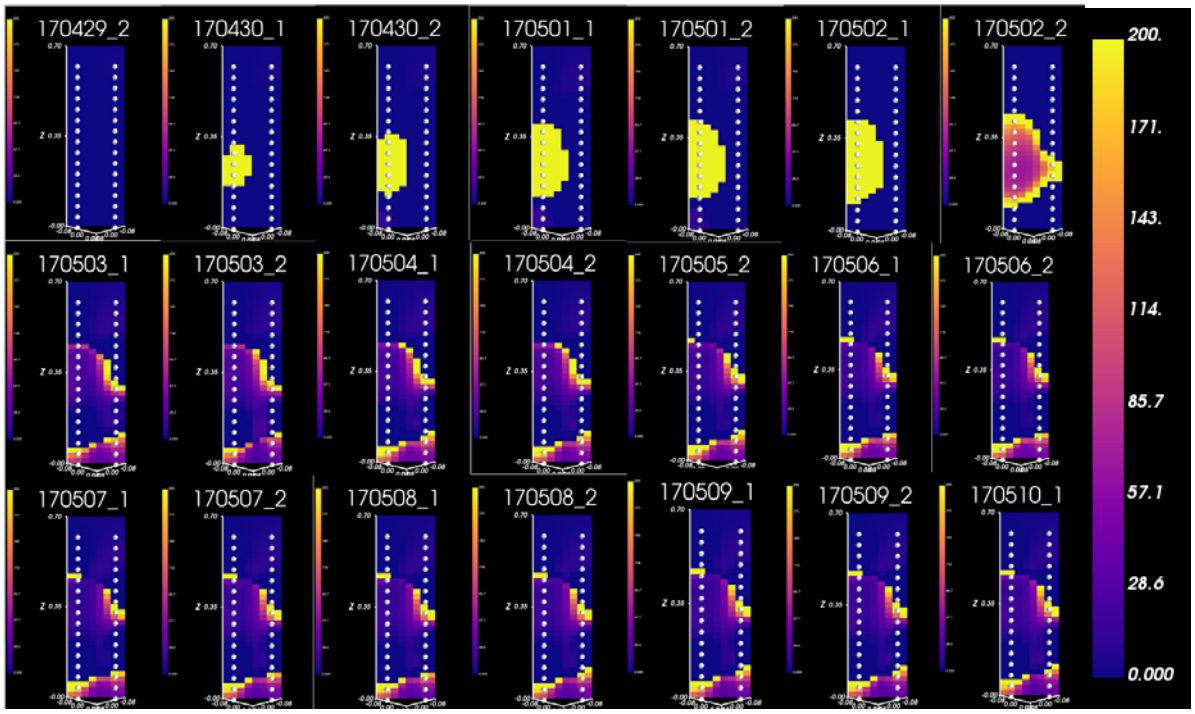

Figure 26. The percent frequency effect (PFE) calculated from the 3D inverted on-time resistance data. The results are presented as vertical cross-sections through vertical electrode lines T1 and T3.

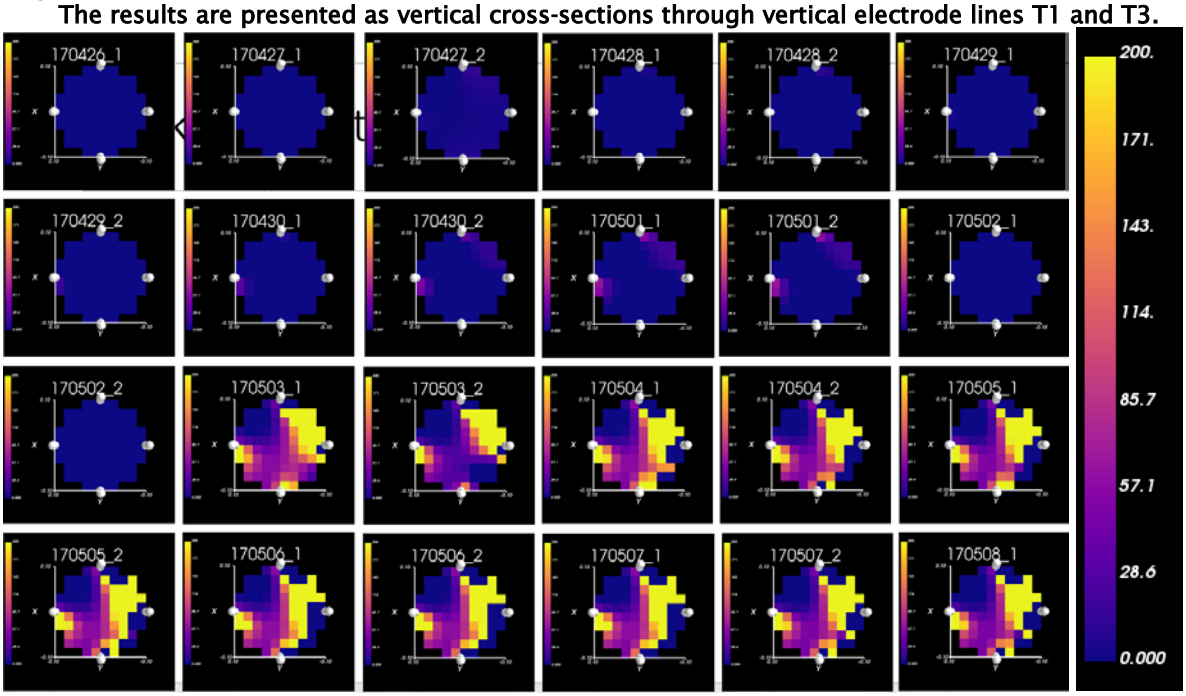

Figure 27. The percent frequency effect (PFE) calculated from the 3D inverted on-time resistance data. The results are presented as horizontal cross-sections for the second lowest level (15). T1 line is on the right.

5.4 Discussion and conclusions

The laboratory-scale, time-lapse ERT results seem to behave as expected. The inverted resistivity distributions and corresponding water content information (from the analyzed samples) is in accordance

© Modern2020

with our previous field-scale considerations as well as with the known experimental petrophysics for the salinity-pellet-water content relationships.

The PFE inversion process seems to be also rather stable. The results show, as expected, that in the bentonite pellet-saline water environment the polarization effects are small due to the homogeneous high clay content material and high conductivity (high salinity and water contents). It can also be recognized that care must be taken in collecting time-domain field measurements designed to replicate frequency-domain laboratory measurements. In the situation, where signal-to-noise ratio is high enough to map polarization effects, IP data will provide insight into changes electrochemical properties and/or in structures and can be useful in conditioning flow and transport models rather than providing accurate pixel-to-pixel information.

The induced polarization tomography offers a valuable, cost-effective addition to ERT monitoring. It can be carried out simultaneously inside the common ERT monitoring process. In the time-domain, the simplest IP process will only double the duration of each monitoring cycle.

In the near future, the 3D ERT and induced polarization measurements will be used more and more together with the 3D reactive transport simulations. The overall, time-lapse resistivity and chargeability distributions offer an effective calibration and updating platform for hydro-geochemically modelled temperature-salinity-water content responses.

The technique is currently applied in the monitoring of buffer and backfill bentonites in the full-scale in-situ system tests in Posiva's underground research facility ONKALO and will be applied in the long-term monitoring of these tests. In these experiments electrode chains are located in the thin pellet layers between the crystalline bedrock and bentonite blocks. ERT and IPT have great potential to be part of repository monitoring concepts that focus on EBS performance and can cope with disturbances caused by intensive instrumentations, such as Posiva's EBS monitoring plan, as described in Modern2020 WP4 Task 4.1 (Deliverable D4.1).

© Modern2020

6. Calibration and validation of constitutive relationships between electrical parameters and temperature and moisture content (STRATHCLYDE)

6.1 Background information

As already mentioned in Section 4, electrical resistivity tomography (ERT) is a common geophysical method that uses injection of electrical currents and measurements of the resulting voltage differences at the earth's surface or in boreholes to reconstruct 2D or 3D images of the bulk electrical resistivity of the subsurface. Common uses of ERT include water exploration and contaminant flow detection (Benson et al., 1997; de Lima et al., 1995; Martinez-Pagan et al., 2009), in engineering site investigations (Banham and Pringle, 2011; Rucker et al., 2009) locating buried artefacts or structures in archaeological surveys (Negri et al., 2008; Tonkov and Loke, 2006) as well as providing geological and hydrogeological site information (Ganerød et al., 2006).

Previously ERT in vertical boreholes has proven useful for environmental investigations (Daily et al., 1995; Daily and Owen, 1991; Deceuster et al., 2006; French et al., 2002; Guérin, 2005; LaBrecque et al., 1996). More recently, investigations using ERT in borehole have been extended to a variety of other applications such as: characterization and monitoring of water infiltration (Coscia et al., 2011), and monitoring CO_2 migration (Schmidt-Hattenberger et al., 2016; Yang et al., 2015), amongst others.

Geophysical electrical monitoring is a potential technique for monitoring the EBS, because it:

1. could be implemented as a non-intrusive monitoring technique;
2. allows capturing local anomalies that local sensors cannot spot;
3. electrical resistivity and dielectric permittivity are very sensitive to changes in water content and are therefore ideal to monitor saturation of the EBS if considered important to a specific programme (Carey et al., 2017; Danielsen and Dahlin, 2010; Korteland and Heimovaara, 2015; López-Sánchez et al., 2017; Merritt et al., 2016; Wang et al., 2017); and
4. electrical resistivity is known to be sensitive to changes in temperature (Carey et al., 2017; Cosenza et al., 2007; Hermans et al., 2015; López-Sánchez et al., 2017; Merritt et al., 2016; Wang et al., 2017).

Previous research conducted in repository-like conditions have been successful in using ERT for monitoring the EBS (Furche and Scuster, 2014; Rothfuchs et al., 2004). However, to the best of the authors knowledge there has been no attempt in investigations to date to implement and develop the approach to monitor the EBS beyond the research phase, as a non-intrusive technique, as in these studies cited, the ERT electrodes are buried inside the EBS.

Laboratory studies including calibration and validation of the relationships between electrical parameters and temperature and moisture content were undertaken. These laboratory studies will enlighten the interpretation of the results of two large scale experiments, the Long Term Rock Buffer Monitoring (LTRBM) and Electrical Resistivity Tomography (ERT) demonstrators, which are field demonstrators installed in the Underground Research Laboratory (URL) at Tournemire. The aim of these laboratory studies and the geophysical monitoring of the aforementioned demonstrators is to assess the capabilities of the ERT as a non-intrusive technique of monitoring the EBS under conditions as close as possible to the expected ones in the repository. Rather than relying on ERT electrodes that are installed inside the EBS, in this approach the ERT electrodes are installed in boreholes adjacent to the buffer. This section of the report will discuss the results obtained from the laboratory studies carried out at University of Strathclyde.

© Modern2020

6.2 Methodological Developments

The electrical resistivity, ρ, of a material is a measure of how well the material retards the flow of electrical current. ERT is a direct current method, although strictly speaking it is a low-frequency alternating current method, however the frequency is so low that it could be considered direct current. The ERT method can be used to estimate the distribution of electrical resistivity under the assumption of electrical isotropy and scalar quantities in the subsurface. Rock type, porosity, ionic strength of the pore fluids, and surface conductivity of geologic materials can be directly related to bulk resistivity (Day-Lewis et al., 2008). Although water in its pure state is non-conductive, the presence of chemical salts in solution produces a conductive electrolyte detectable with resistivity methods (Zohdy et al., 1974). ERT is therefore sensitive to a number of properties, including the nature of the solid constituents of soil (particle size distribution, mineralogy), arrangement of voids (porosity, pore size distribution, connectivity), degree of water saturation (water content), electrical resistivity of the fluid (solute concentration) and temperature (Samouëlian et al., 2005).

The base principle of the surface ERT is straightforward: a continuous electric current of intensity I (in mA) is generated between two current electrodes A and B – where A is the injection electrode (positive), and B is the reception electrode (negative) – placed at the surface of a ground. If two potential's electrodes, M and N, are added, allowing the measurement of the difference of potential ΔV (in mV) due to the joint action of A and B, the resulting quadripole allows measuring the ground's apparent resistivity ρ_a (in Ωm), that can be calculated as follows.

$$\rho_a = \kappa \frac{\Delta V}{I}, \qquad (8.1)$$

where: ρ_a (Ωm) is the apparent resistivity (for inhomogeneous ground conditions), k (m) is the geometric factor, ΔV (mV) is the potential difference between electrodes M and N and I is the current (mA).

The geometric factor k depends on the geometry of the electrode array and the topography. Details about the geometric factor can be found in Lopes and Tarantino (2018b). The diagram displaying the apparent resistivity as a function of location and electrode spacing is called the pseudo section and provides an initial picture of the resistivity distribution.

An inversion process of the measured data is necessary for the final interpretation. This process transforms the apparent resistivities into a reliable model discretized into a distinct number of elements of homogeneous resistivity.

In electrochemistry, polarization is defined as the change in the equilibrium potential of an electrochemical reaction. There are two types of induced polarization (IP) known to geophysicists, the membrane polarization known as the background or normal IP, where there are variations in the mobility of ions in fluids throughout the material, and the electrode polarization where there are variations between ionic and electronic conductivity where metallic metals are present. Both are indistinguishable by IP measurements.

IP measurements can be done in two ways, known as - the time-domain and frequency domain induced polarization. In the time-domain IP, which is the IP method used in this report, the current is cut off and voltage decay is recorded. The Residual Voltage V(t) existing at a time t after the current is cut off is compared with the steady voltage V during the current-flow interval. Chargeability, m (mV/V), is the parameter used to measure the IP in time-domain and it can be defined as:

© Modern2020

$$m = \frac{1}{(t_2 - t_1)} \frac{1}{V} \int_{t1}^{t2} V(t) dt, \quad (8.2)$$

IP can be measured in the field using a similar approach to that for DC resistivity. The potential electrodes should, ideally, be non-polarizing (for example, copper-copper sulphate), although conventional DC resistivity electrodes have been used with some success (Dahlin et al., 2002).

The ERT has long been established as a reliable method to determine qualitatively changes in water content and temperature, among other things (Binley and Kemna, 2005). IP surveys have traditionally been used in the mineral exploration industry, particularly for metal sulphides (Loke, 2013), but it has also been used in a variety of other applications such as environmental investigations to identify contamination areas (Elis et al., 2016) and groundwater exploration (Vacquier et al., 1957). Thus, the challenge has always been drawing a quantitative parallel between the electrical parameters and other hydrogeological, environmental and geotechnical features of the earth. Evolution in this area was reported in terms of resistivity (Fan et al., 2015; Zieher et al., 2017), but there is still a long way for the IP.

6.3 Validation with experimental data

A mock-up scale laboratory test was proposed to assess the non-intrusive capabilities of the ERT. However, preliminarily, calibration experiments were carried out to test the relationship between the electrical parameters and the changes in temperature and moisture content on bentonite samples, which is the material under investigation.

6.3.1 Materials

The bentonite material used in all three experiments and synthetic water used either to prepare samples for the calibration test or to saturate the Mock-up experiment are presented here.

6.3.1.1 Bentonite material

The Bentonite material under investigation is constituted by a mixture of bentonite pellets and powder, namely mixture 3, provided by NAGRA. The average dry density of the pouring material is 1.45g/cm^3 (Garitte et al., 2015). Figure 34 shows the particle size distribution of the material.

6.3.1.2 Synthetic water

The electrical conductivity of water is much larger than that of the solids; therefore, the electrical resistivity of Geomaterials is affected by the presence of water filling their pores. Thus, different resistivity and induced polarization results could be expected depending on the water composition used to prepare the samples. To ensure meaningful and comparable results, a synthetic water representative of the Callovo-Oxfordian argillite at Bure, used for the SEALEX tests (Wang et al., 2013), and the ERT and LTRBM demonstrators are used for the laboratory tests performed here. The chemical composition of the synthetic water is given in Table 3. The resistivity of the water measured with a resistivity probe meter was 2.54Ωm.

6.3.2 Calibration test: Measurements of resistivity and Induced Polarization on Bentonite samples using the four-point method

Bentonite Clay samples were prepared by mechanically mixing Bentonite Clay with Synthetic water up to the target gravimetric water content at 1000 rpm for 5 minutes. All samples were left in a sealed bag for 24 h for homogenization before any test was performed.

© Modern2020

Resistivity and induced polarization tests were carried out on those bentonite samples compacted on the sampler at different gravimetric water contents and exposed to different background temperatures using the 4-point method. This method consists of injecting the current into copper electrodes located at both extremes of the sampler in contact with the cross section of the sample and the difference in potential generated are read by two electrodes located on the top of the sample. The resistivity of the material under test can then be calculated according to the expression below:

$$\rho = \frac{V}{I}\frac{A}{L}, \tag{8.3}$$

where V is the potential (V), I is the current (A), L the length of the cylinder sampler (m) and A is its cross-sectional area (m^2) of the sample.

The literature (Cosenza et al., 2007; Giao et al., 2003; Rothfuchs et al., 2004) suggests that the ratio between length and diameter of the sample should be greater than 2.5 for unidimensional tests. Therefore, the PVC sample holders used are 12 cm long and 3 cm in diameter. Two holes, 10cm apart, were created on the sample holder to house the potential electrodes.

Ten compacted samples with target gravimetric water contents of 18%, 23%, 27%, 32%, 39%, 45%, 59%, 73%, 86% and 100% were compacted into the sample holder and the resistivity and induced polarization were recorded at environmental temperature (20℃). The target density of all samples was 1.4 g/cm^3, which is the expected initial density of the ERT demonstrator buffer at installation (refer to Lopes and Tarantino (2018a) for details regarding the ERT demonstrator). It is not possible to perform resistivity or induced polarization measurements on samples with gravimetric water content lower than 18%. The same set of samples were heated in an oven to four temperatures: 30℃, 40℃, 50℃, and 70℃. At each level, temperature was maintained constant during 24 hours. The gravimetric water content of each sample was measured after compaction at 20℃ and after the heating tests. Before and after each temperature level, the loss of weight, the resistivity and the induced polarization were measured. It should be noted that both the resistivity and induced polarization were recorded immediately after removal from the oven but also 5 hours afterwards following Cosenza *et al.* (2007) methodology, in order to obtain a thermal equilibrium, i.e., to equilibrate sample temperature and room temperature. Nevertheless, to use the results as calibration for the ERT demonstrator test in Tournemire, the most meaningful results are the measurements taken immediately after the oven treatment since in the ERT demonstrator measurements of resistivity are going to be taken during the heating process.

The current electrode used are solid rod disks, with the diameter of the sample (3 cm), made of copper. According to the literature (De Donno and Cardarelli, 2011; LaBrecque and Daily, 2008; Postic and Doussan, 2004) bronze electrodes are the closest to non-polarisable electrode behaviour, therefore the potential electrodes used are made of bronze.

Figure 28 shows the volumetric water content and temperature each bentonite sample was exposed to against the resistivity values measured in a 3D plot. Similarly, in Figure 29, the relationship between volumetric water content, temperature and chargeability values measured are presented. Values of resistivity and chargeability on these plots were taken immediately after oven treatment.

© Modern2020

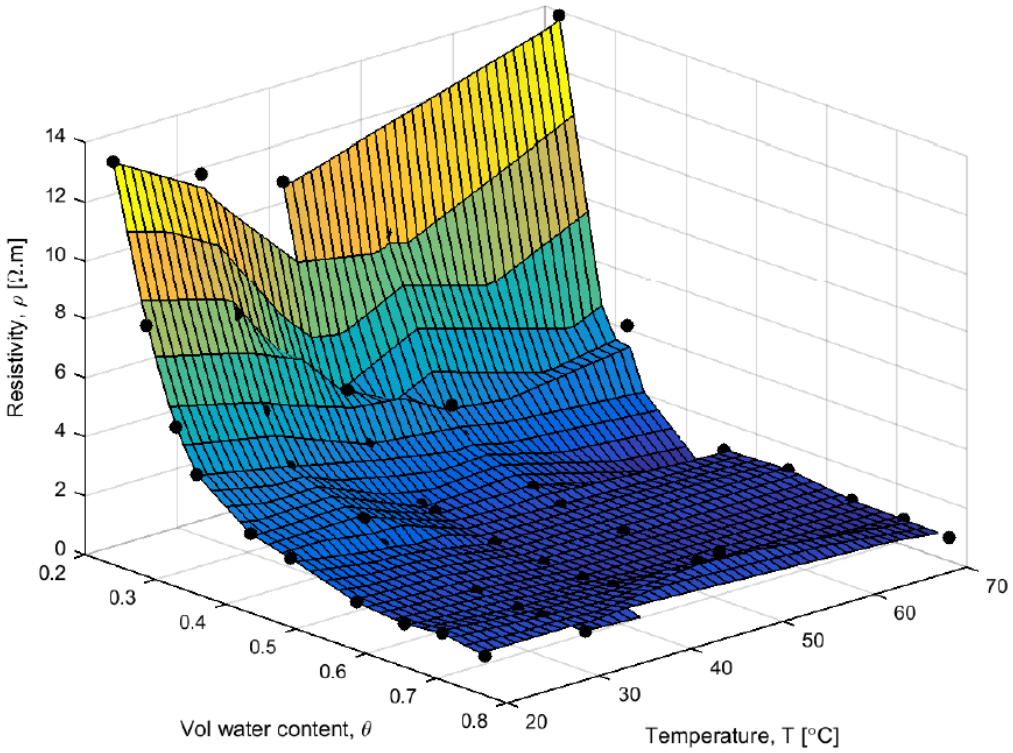

Figure 28 : Resistivity results of bentonite samples

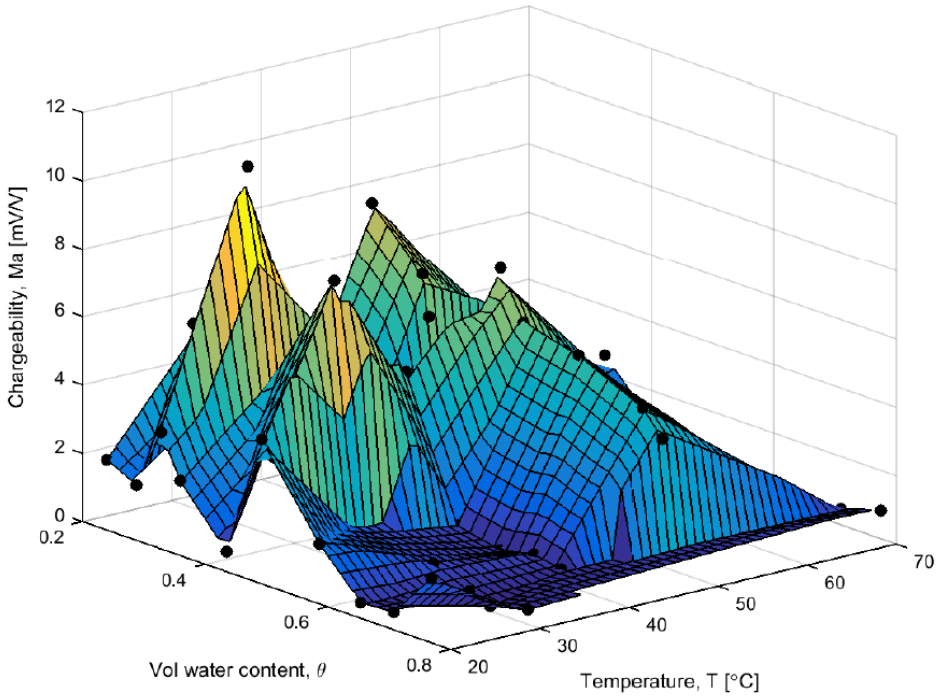

Figure 29 : Chargeability results of bentonite samples

Resistivity values of the bentonite samples are relatively low even in samples with low volumetric water content, where the highest value recorded was 13.86 Ωm, which was expected given the good conductivity property of the bentonite material. As expected, resistivity values decrease with increase of volumetric water content and there is a minor decrease of resistivity values with increase of temperature of exposure. Those differences are less significant the higher is the volumetric water content. For

© Modern2020

instance, the average resistivity value of all samples, exposed to all temperatures, with volumetric water content higher than 0.5 is 1.24 Ωm and standard deviation of 0.24 Ωm.

On the other hand, the relationship between volumetric water content, temperature and chargeability is harder to assess. Figure 35 shows the relationship between chargeability and volumetric water content, where each series of data corresponds to a temperature of exposure. It can be observed that for all temperature series the peak chargeability values are reached between 30 and 50% of volumetric water content. Kiberu (2002) investigated the relationship between chargeability and water content, in the range between 15 and 40%, of a few natural Sandy and Silty soil samples collected in Spain and Holland. The author's results were asymmetric normal distribution curves, which has also been previously reported by Ogilvy and Kuzmina (1972) and Parkhomenko (1971) in shaly sands. According to the author, this behaviour is explained by the presence of fixed sites on the clay surface that are responsible for active IP. When only a few of these sites are occupied by water, there are only a few mobile ions, as they are closely attached to the clay surface, as a result the IP response is small. However, as the water gets increased, the sites become available for ion exchange which gives a marked increase in the response up to the maximum. Then when all sites are occupied by water, the IP response obtained is small again. The same trend can also be observed, repeating itself at least twice, in the results obtained for the bentonite samples in this report – between 20 and 40% and between 40 and 80%.

Ogilvy and Kuzmina (1972) have also investigated the dependency of induced polarization on temperature in bentonite samples. The temperature range investigated by the authors was between -16 and 16°C. Although the authors have not conducted any experiments on temperatures higher than 16°C, they have claimed that at positive temperatures (up to 40°C) the polarizability is nearly constant and with further increase in temperature, IP tends to decrease due to an increased dissociation of ions. The results obtained in this report showed that, the majority of the samples experienced an increase in chargeability from 20 to 30°C and from 40 to 50ºC while experiencing a decrease in these values from 30 to 40°C and from 50 to 70°C (Figure 36).

Those studies suggest that the chargeability results obtained in this report for bentonite samples although difficult to access, due to lack of clear trend and small variation range, are consistent. Because of this difficulty, the decision of not conducting chargeability surveys further in the next experiments was made.

6.3.3 Mock-up experiment using ERT

A mock up setup was designed as shown in the Section 8 (Appendix, Figure 37). A total of 48 electrodes were installed into 4 boreholes while Bentonite was poured (1.4 g/cm^3) on the main shaft of the concrete block. On top of the bentonite shaft a heater was placed (maximum temperature of 90℃). Relative humidity (RH) and Temperature sensors (W. Yang et al., 2015; Yang et al., 2017) were installed into the bentonite at different depths. Two independent experiments were then planned: a temperature and a saturation test.

3D ERT surveys carried out during both experiments were optimised following the experienced gained on the blank test surveys of the ERT demonstrator and LTRBM. Data collection and data quality details are presented in Section 8 (Appendix).

The first test performed was a temperature test, where temperature was increased in steps up to the maximum of 90℃ and then the heater was switched off. Figure 30 (Section 8 (Appendix)) shows the temperature recorded over time during the temperature experiment by the temperature sensors. In Figure 30c (Section 8 (Appendix)) it is possible to see the variation of saturation in the first 7 cm

© Modern2020

immediately below the heater, as well as the values of saturation along the bentonite profile at different times during the test.

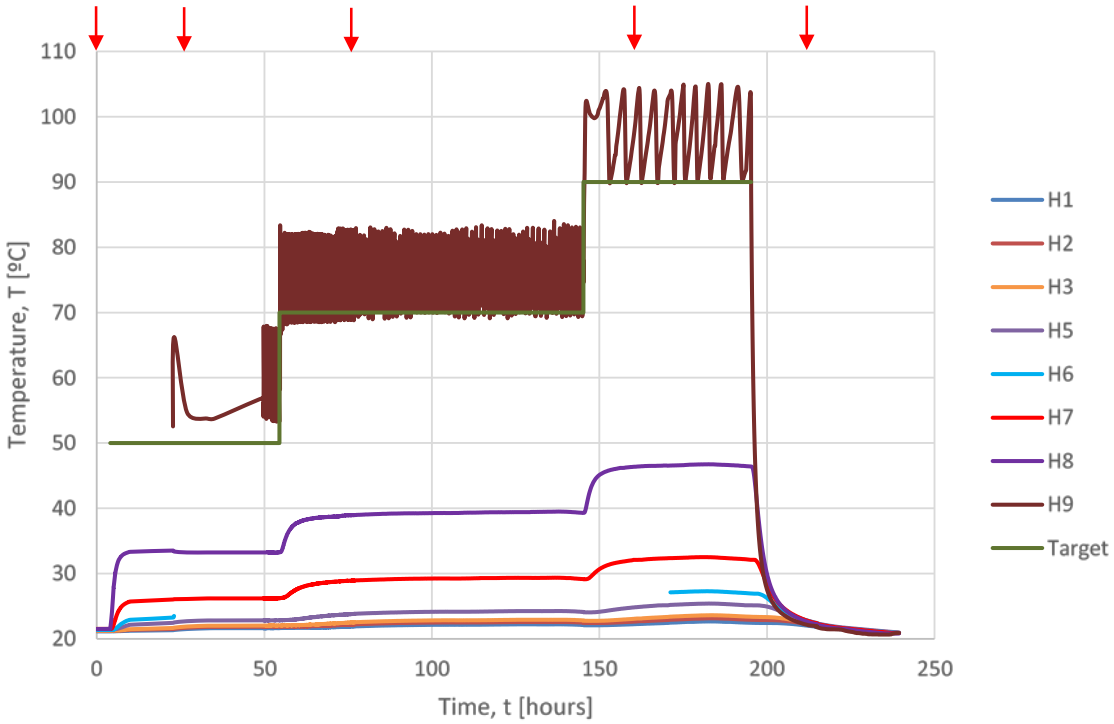

(a)

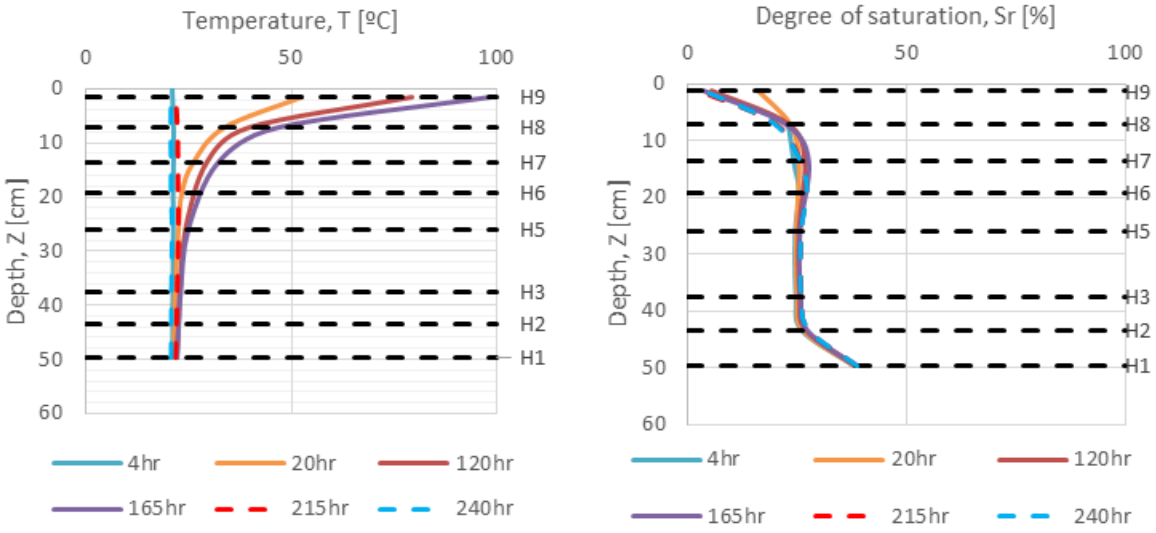

(b) (c)

Figure 30 : Temperature test (a) Temperature recorded by each sensor over the 240 hours of experiment, where red arrows on top of the chart indicate times where ERT surveys were performed; (b) Temperature profile of bentonite along different times of experiment; (c) Saturation profile of bentonite along different times of experiment.

By the results collected with the RH and Temperature sensor, it is possible to notice that a heating front was created lasting up until around 30 cm below the heating point. This increase in temperature has also altered the Relative humidity and consequently the saturation of the first 7 cm of the bentonite layer. Five ERT surveys were performed along the heating and cooling process.

© Modern2020

A 2-point method resistivity measurement performed on a cubic sample of the concrete used in this mock-up experiment indicated a resistivity of 140 Ωm. As previously mentioned, the capabilities of the equipment used did not allow the assessment of the resistivity of the bentonite at a gravimetric water content lower than 18%. A calibrated TDR probe was used to assess the resistivity of the bentonite just prior to installation (w = 8%) and the resistivity obtained was 5,045 Ωm.

Figure 31 shows the inversion of the ERT data collected before the start of the heating test, as well as after 168 h, when heater was at 90°C and after 216 h when heater was switched off. The cubic box in the centre of the inversion models show the physical position of the bentonite shaft.

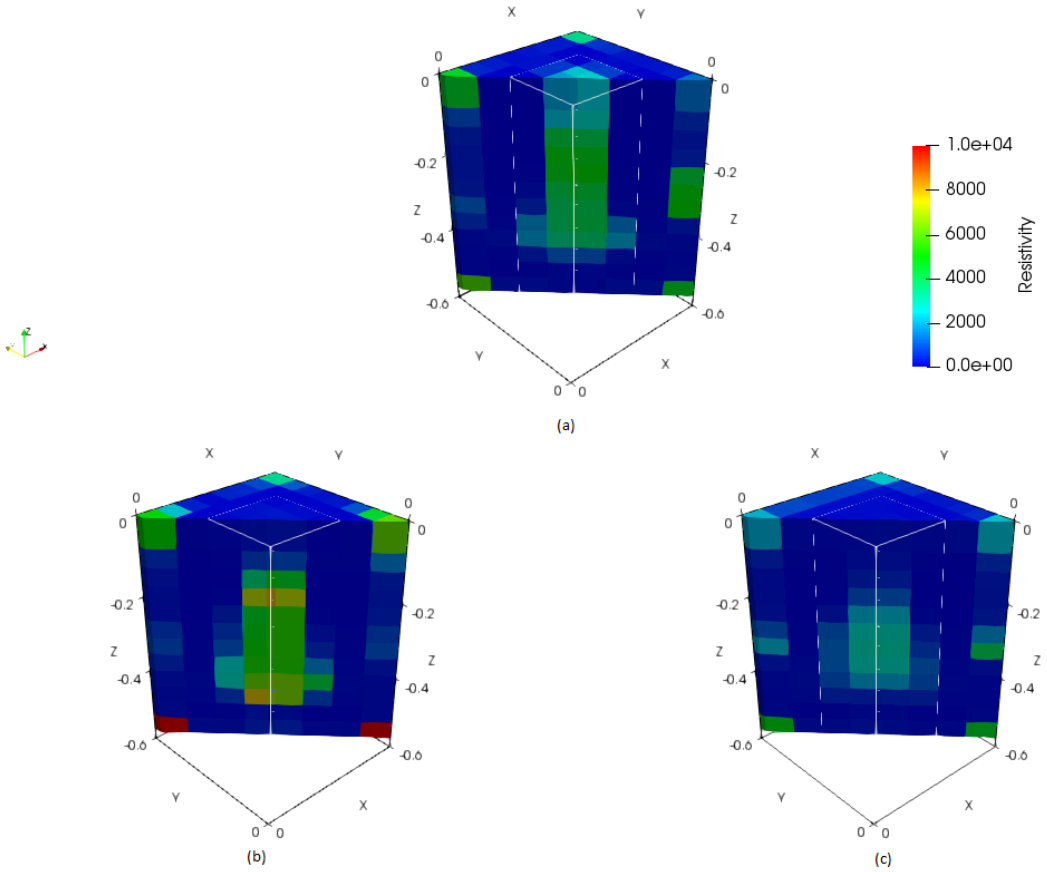

Figure 31: ERT surveys temperature test. (a) Before start of test, base result, heater off, (b) After 168 h, heater at 90°C, (c) After 216 h, heater off.

In general, it is clear that the models captured well the two distinct materials – the background resistivity of the concrete block is within the order of magnitude expected and the bentonite area is characterised by higher resistivities ranging from 2000 to 6000 Ωm, eventually reaching 8000 Ωm. In Figure 31b, it can be noted that the first 10cm of the bentonite shaft is characterised by smaller resistivity values when compared with the ERT model before the heating, which is consistent with the increase in temperature imposed in this area. Figure 31c shows that the higher resistivity values at the top of the bentonite shaft are not recovered and it is also possible to notice a reduction on the resistivities of the bentonite region throughout its whole depth. The overall reduction of the resistivity in the bentonite area after the cooling period could be explained by the water injection into the electrode boreholes to improve contact resistance. Although the shaft was impemeabilised prior the installation, water absorption was not completely eradicated, therefore some water could have flow from the electrodes boreholes towards (and eventually inside) the shaft influencing the inversion.

© Modern2020

The second test carried out, the saturation test, started after the cooling down of the previous temperature experiment. The water inlet was opened and water was let to flow into the main shaft by gravity. At the time of writing this report, the first 500 hours of the data collected had been processed and analysed. Figure 32 a shows the saturation recorded over time during the saturation experiment by the RH sensors, as well as the amount of water injected into the bentonite. In Figure 32b it is possible to see the values of saturation along the bentonite profile at different times during the test. The maximum and minimum temperature recorded during the first 500 hours of the saturation experiment were 21.1 and 20.4°C respectively. Up until this time, four ERT surveys were performed, before the start of saturation and after 20, 250 and 500 h of the saturation, as indicated in Figure 32a by the red arrows.

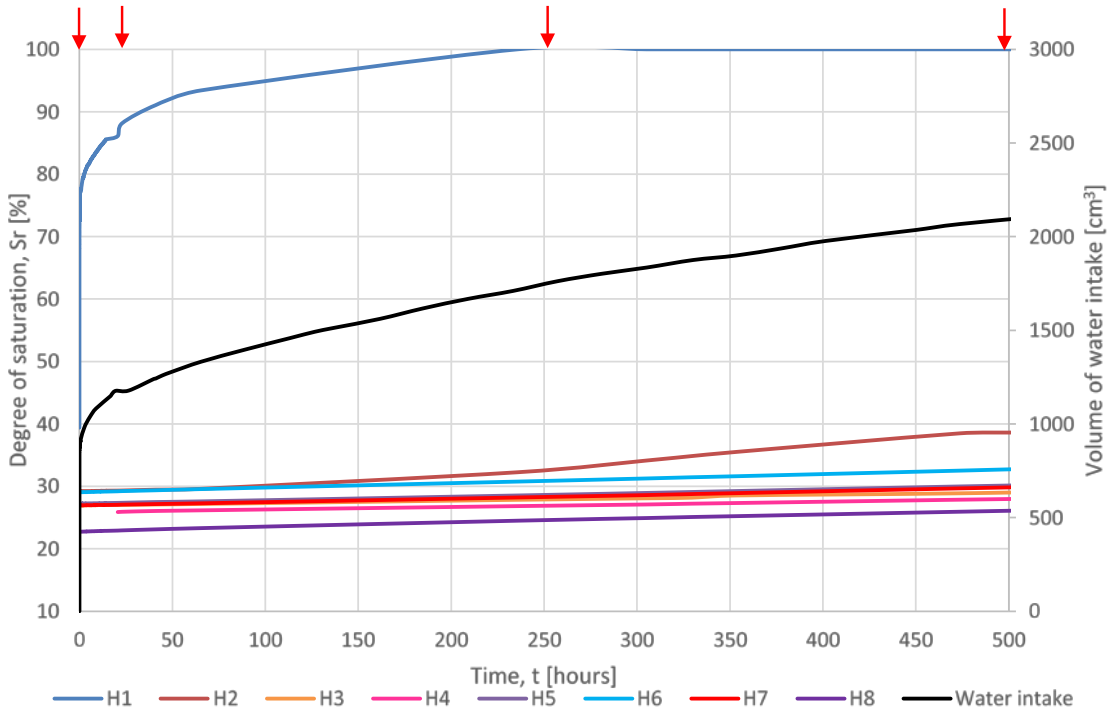

(a)

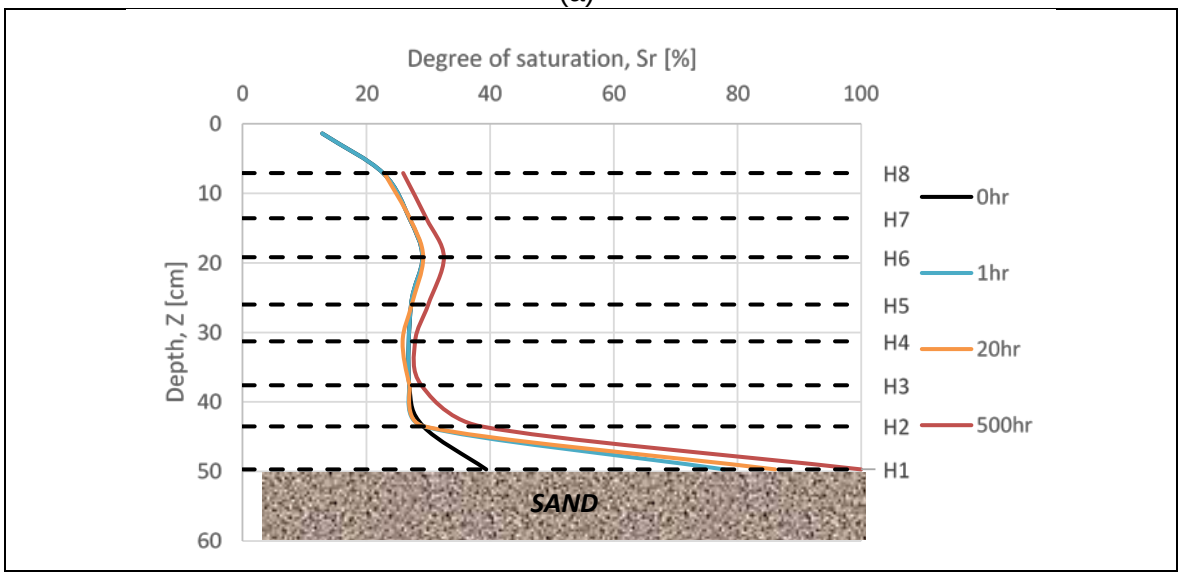

(b)

Figure 32 Saturation test . (a) Degree of saturation recorded by each sensor over the first 500 hours of experiment, where red arrows on top of the chart indicate times where ERT surveys were performed and (b) Saturation profile of bentonite along different times of experiment.

© Modern2020

By the results collected with the RH and Temperature sensor it is possible to notice that after around 250 hours the interface between sand and bentonite was fully saturated (sensor H1). And around the same time, sensor H2 immediately above sensor H1, started showing an increase in saturation that is less pronounced on remaining sensors. It is expected that this experiment will last several months, therefore results are consistent.

Figure 33 shows the inversion of the ERT data collected before the start of the saturation test, as well as after 20 h, 250 h, and 500 h of continuous water injection by gravity.

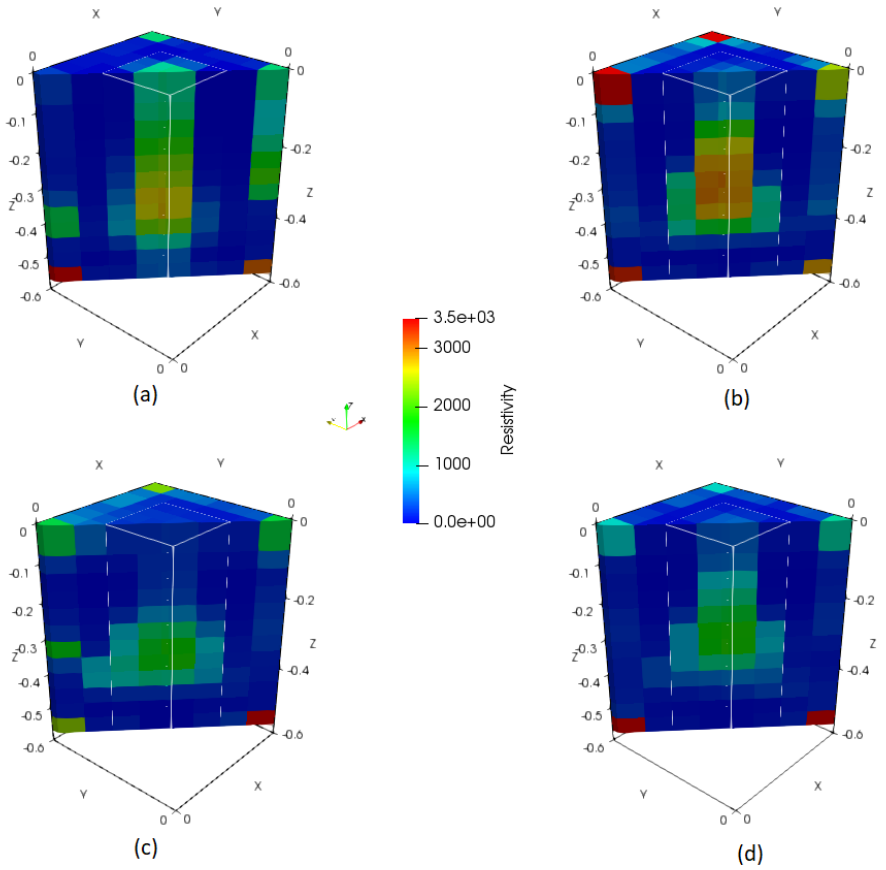

Figure 33: ERT surveys, saturation test. (a) Before start of test, base result, water inlet closed, (b) After 20 h of continuous water injection by gravity, (c) After 250 h of continuous water injection by gravity (d) After 500 h of continuous water injection by gravity

Once again, in general terms, the models captured well the two distinct materials, and there is a gradual reduction of resistivity as time progresses, which was expected with ingress of water from the bottom of the block. It is worth highlighting that at the bottom of the shaft there is a 9.8 cm thick layer of sand, that has been instantaneously saturated with the start of water injection. The slight overall reduction in resistivity around the bentonite area is also justified by the water injection into the electrode boreholes to improve contact resistance. The saturation process is still in the beginning and little could be concluded at this stage apart from the fact that it is expected to be possible to trace the water saturation with adjustments on the color scale as saturation progresses. Water injection to improve electrodes contacts are being controlled to reduce its influence on the experiment.

6.4 Conclusions

The calibration studies performed on bentonite samples revealed an expected relationship between resistivity and moisture content as well as resistivity and temperature. The relationships between chargeability and moisture content and chargeability and temperature, although harder to assess, were consistent with results reported elsewhere.

© Modern2020

ERT surveys carried out on the mock-up laboratory experiment were able to qualitatively show the heating front created by the heating test and also has the potential to show the saturation front as water progresses into the bentonite shaft, which is an innovative way of monitoring changes in temperature and moisture content non-intrusively.

Quantitative analysis is harder to report, even for the resistivity parameter, due to the nature of the relationship. There is a sharp reduction in resistivity in a narrow saturation range, followed by almost constant values of resistivity for values of volumetric water contents higher than 40%. The same is observed for the relationship between resistivity and temperature.

3D ERT surveys are fundamental for the success of the non-intrusive approach proposed here. Experience gained on the surveys performed in the LTRBM and ERT demonstrator blank tests (Lopes et al., 2018; B. de C. F. L. Lopes and Tarantino, 2018) showed that results could be significantly improved if the monitoring approach uses four rather than two boreholes for the installation of electrodes.

To improve further the approach, IP surveys could potentially be incorporated to give additional information to the ERT surveys. However, the interpretation of the chargeability results needs have to be carefully considered, since they are not straightforward.

© Modern2020

7. Overall conclusions

In this report, we have focused on specific improvements that were judged particularly useful for radioactive waste repository monitoring. It is, however, important to note that this is by no means a comprehensive discussion on geophysical repository monitoring in general. For this, the reader is referred to the state-of-the-art report that was provided by the preceding MoDeRn project.

Although most research objectives could be achieved, further research will be required to make the two geophysical techniques considered in this report (i.e., seismic FWI and ERT/IPT) applicable as standard repository monitoring techniques. Therefore, we do not only briefly summarize the achievements, but we also highlight open questions and provide, where appropriate, suggestions for further research.

Seismic waveform inversions (FWI)

Seismic anisotropy of the host rock is a long-standing problem that has precluded application of the powerful FWI techniques for monitoring radioactive waste repositories. With the new developments in the framework of this project, this problem could be addressed. In particular,

- a suitable parameterization of anisotropy was found and implemented,
- structural constraints (i.e., imposing structural similarity between different parameter sets) for improving the reliability of FWI inversions were established, and
- the methodology was tested with field data.

Limitations that require further research can be summarized as follows.

- The method developed in this research is restricted to 2D problems. Extensions to 3D is conceptually simple, but computationally very expensive. Nevertheless, efforts should be made to tackle this challenge.
- Currently, constitutive relationships are lacking that allow “translating” the elastic properties obtained with seismic FWI to quantities, such as moisture content and permeability, which are ultimately required to assess the integrity of a repository.
- The current technology offers high-resolution 2D images of the repository and its surroundings. For monitoring subtle temporal changes, it will be required to adopt differential tomography techniques, as discussed in Section 3.

Differential tomography

A novel technique was established that allows consistent and high-precision differential changes of physical parameters (e.g., GPR or seismic propagation velocities) to be delineated. The methodology was tested successfully in the framework of the Mont Terri Full-scale Emplacement (FE) experiment. As input data, phase information from GPR data were employed, and it should be a relatively straightforward task to apply the technology to FWI problems.

At this stage, it is difficult to judge, if further methodological research on differential tomography is required. This needs to be re-assessed, when the technology will be applied to FWI problems.

Anomaly detection algorithms

A detection algorithm was established and tested with synthetic data, and the analysis of ERT field data is currently underway. The technique proposed offers considerable opportunities for making a quick

© Modern2020

assessment of the state of a repository, or, more precisely, if significant changes, within or around the repository have occurred.

However, more research is required, before the technique can be applied in a routine fashion. In particular, the level of reliability of the detection algorithm needs to be studied in more detail.

Geoelectrical techniques

The potential of geoelectrical techniques for monitoring radioactive waste repositories was tested in the framework of this project. For that purpose, ERT and IPT algorithms were implemented and tested. In particular, the performance of the ERT algorithm was validated with laboratory experiments.

Besides the algorithmic developments, extensive calibration tests with bentonite samples were performed. Furthermore, relationships between the electrical parameters, such as resistivity and chargeability, and other physical parameters, such as temperature and moisture content could be established. The methodology is currently further tested with a demonstrator experiment in Tournemire.

Clearly, there is a need for further research. Besides considering the results from the ongoing Tournemire experiment, which is running beyond the lifetime of the Modern2020 project, there are two critical issues that require further attention.

1. It needs to be investigated, how the results from the laboratory experiments (Section 4) can be up-scaled to realistically sized repository structures.
2. The ERT/IPT experiments, performed in the framework of this project, were conducted in an invasive fashion. It needs to be analyzed, how the technology performs, when the electrodes are placed outside of the repository.

© Modern2020

8. Appendices

8.1 Calibration and validation of constitutive relationships between electrical parameters and temperature and moisture content

8.1.1 Materials

Figure 34 shows the particle size distribution of the Bentonite material, provided by NAGRA using in all experiments carried out in this section of the report.

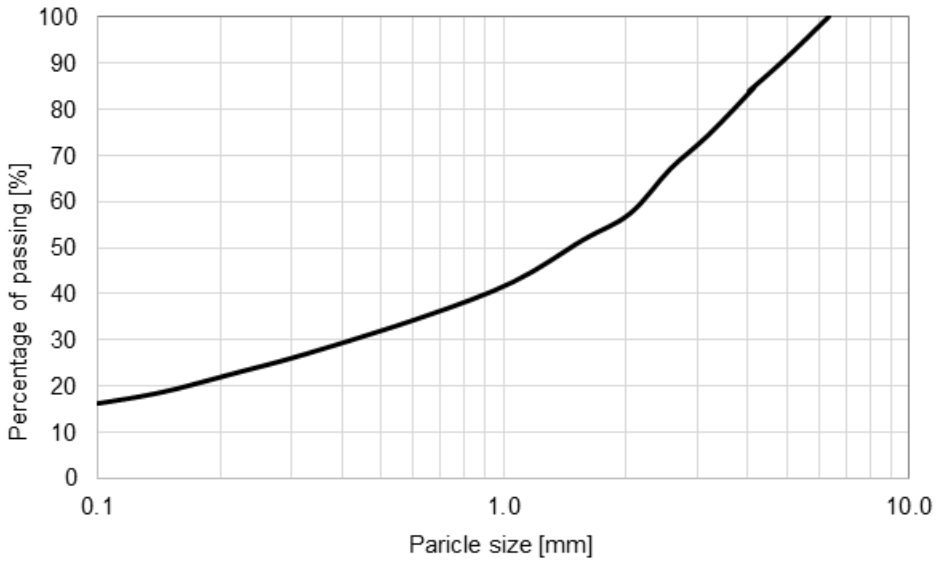

Figure 34 : Bentonite pellets and powder particle size distribution (Garitte et al., 2015)

The chemical composition of the synthetic water representative of the Callovo-Oxfordian argillite at Bure, used for the SEALEX tests, ERT and LTRBM demonstrators as well as used in all experiments carried out in this section of the report is given in Table 3.

Table 3. Chemical composition of Synthetic water

Salt	Molar mass [g/mol]	Concentration [mol/L]
Calcium Sulphate	169.17	7.60E-03
Sodium Hydrogen Carbonate	84.01	4.20E-03
Magnesium Sulphate Heptahydrate	246.47	5.90E-03
Potassium Chloride	74.56	8.99E-04
Sodium Sulphate	142.04	5.50E-03
Sodium Chloride	58.44	4.00E-03

8.1.2 Calibration test

The chargeability dependency on volumetric water content and temperature are presented in Figure 35 and Figure 36 respectively.

© Modern2020

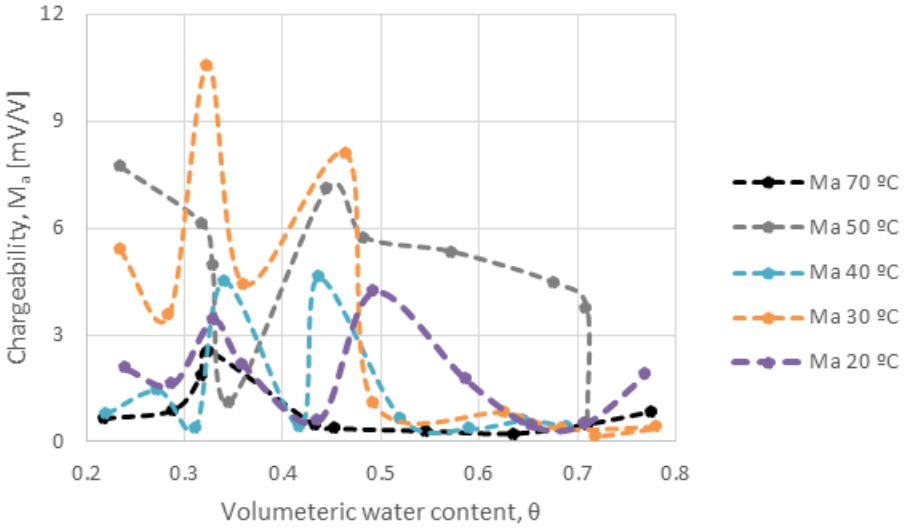

Figure 35: Chargeability dependency on volumetric water content, where each series of data corresponds to a temperature of exposure.
The data shown in this graph correspond to measurements obtained immediately after samples removal from oven.

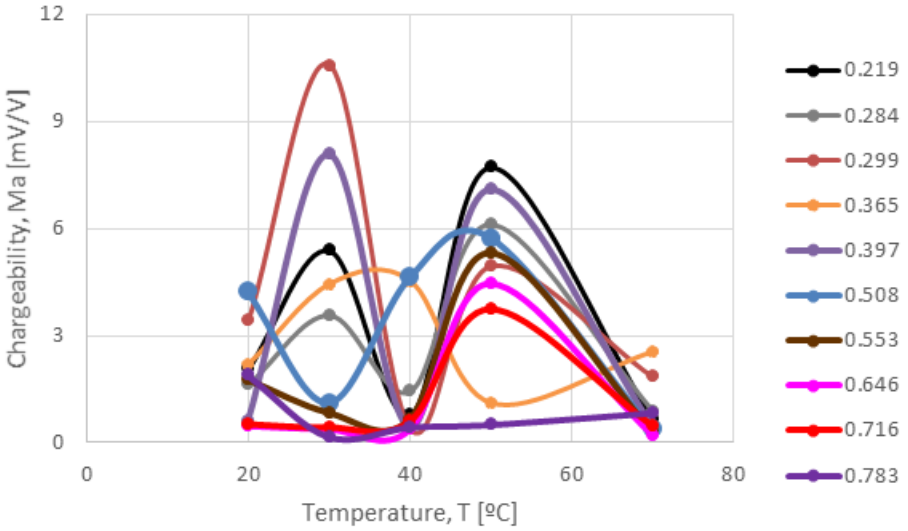

Figure 36: Chargeability dependency on temperature, where each series of data corresponds to samples with the same volumetric water content.
The data shown in this graph correspond to measurements obtained immediately after samples removal from oven.

© Modern2020

8.1.3 Mock-up experiment

A sketch of the mock-up experiment designed in concrete is shown in Figure 37. The block is made of concrete with dimensions of 60x60x80cm. In the centre of the block a shaft with 20 cm in diameter and 60 cm height was created. Four small boreholes with 3cm in diameter and 60 cm length were also created distancing 21 cm from the centre of the main shaft to the centre of each borehole. To let water inside the main shaft, an additional 0.5 cm in diameter L shape pipe was installed 10 cm from the bottom of the block to the centre of the shaft, as indicated in Figure 37. Figure 38 shows the manufacturing process of the concrete block and the installation completed.

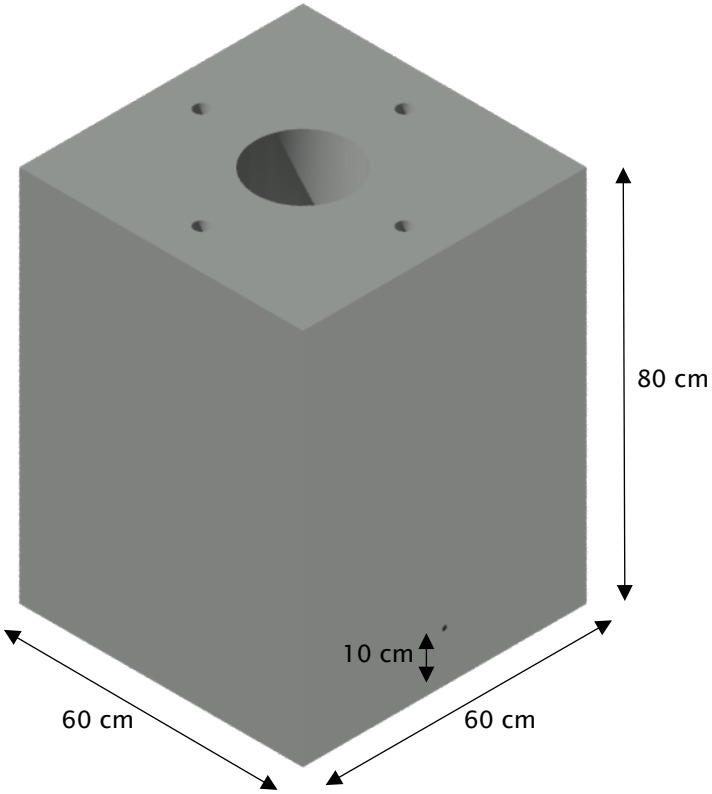

Figure 37 : Mock-up experiment – concrete block

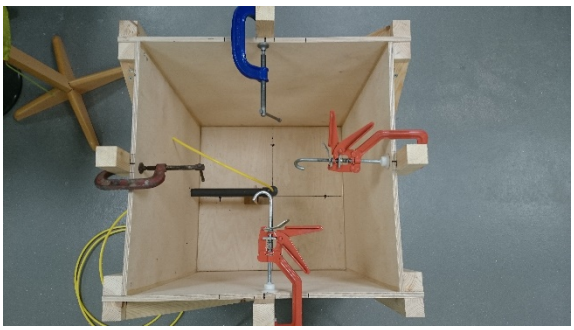

(a)

(b)

© Modern2020

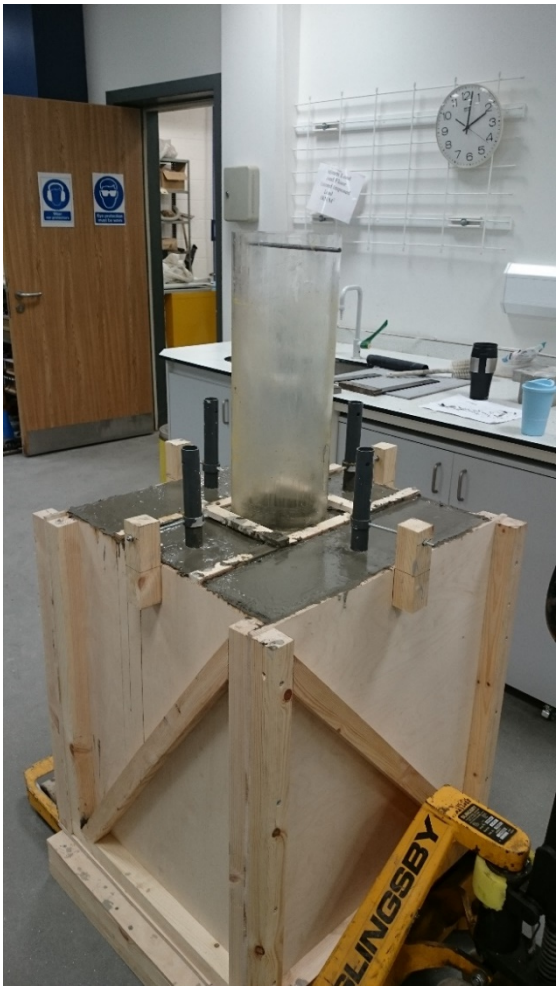

(c)

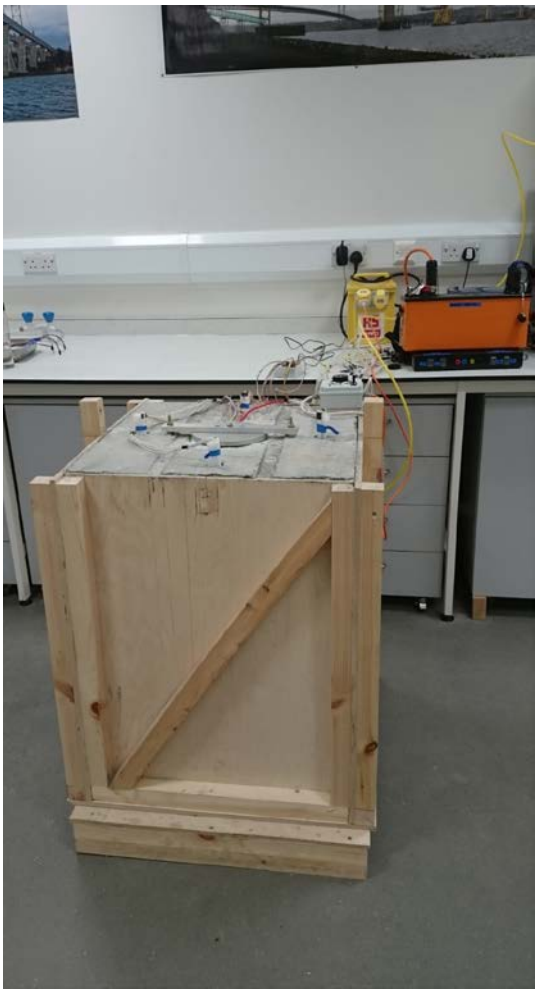

(d)

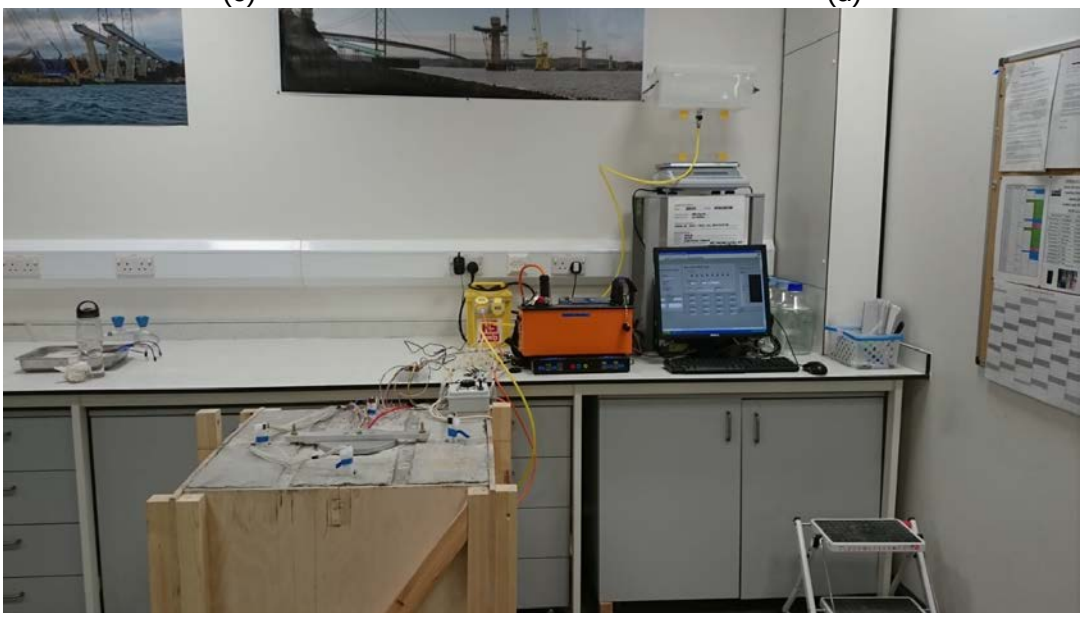

(e)

Figure 38 : Mock-up experiment
(a) Top view of mould before casting, with details of water inlet; (b) Casting process; (c) Curing process; (d) Installation completed and (e) Overview of set up.

© Modern2020

A geotextile was placed at the bottom of the main shaft followed by a 9.8 cm layer of sand and 49.7 cm layer of Bentonite clay. The shaft is closed with an aluminium heater plate of 1.2 cm thick. There are eight relative humidity and temperature sensors installed within the bentonite. Those sensors were manufactured and tested at University of Strathyclyde (W. Yang et al., 2015; Yang et al., 2017). The position of each sensor is indicated in Table 4 and a cross section illustrating the installation is presented in Figure 39.

Table 4. RH and temperature sensors depths

RH and Temperature Sensors	Positioning from surface, Z (cm)
H1	49.7
H2	43.5
H3	37.6
H4	31.3
H5	26.0
H6	19.2
H7	13.6
H8	7.1

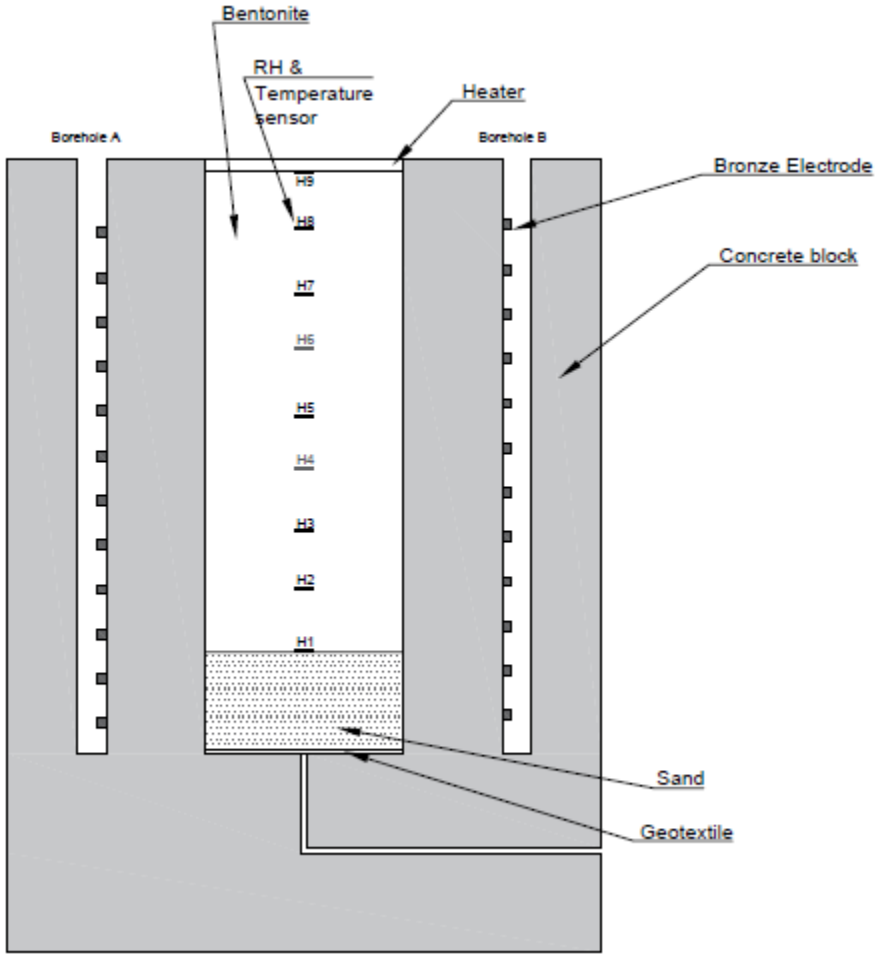

Figure 39 : Cross section of Mock-up illustrating the position of RH and Temperature sensors

In each of the four boreholes, a set of twelve electrodes spaced at 4.5 cm are installed, totaling 48 electrodes in this setup. Similarly, to the electrodes set installed in the LTRBM and ERT demonstrator in Tournemire, these electrodes are attached to half PVC pipes (1.5 cm diameter) as shown in Figure 40.

© Modern2020

Electrodes are made of bronze pins and stainless steel nuts (Figure 41). To ensure good contacts between the electrodes and the borehole walls a strip of foam is attached to the back of the half PVC pipes. The geometric position of each electrode is presented in Table 5. Axis convention is illustrated on Figure 42.

Figure 40: Electrodes line

Figure 41: Electrode detail

© Modern2020

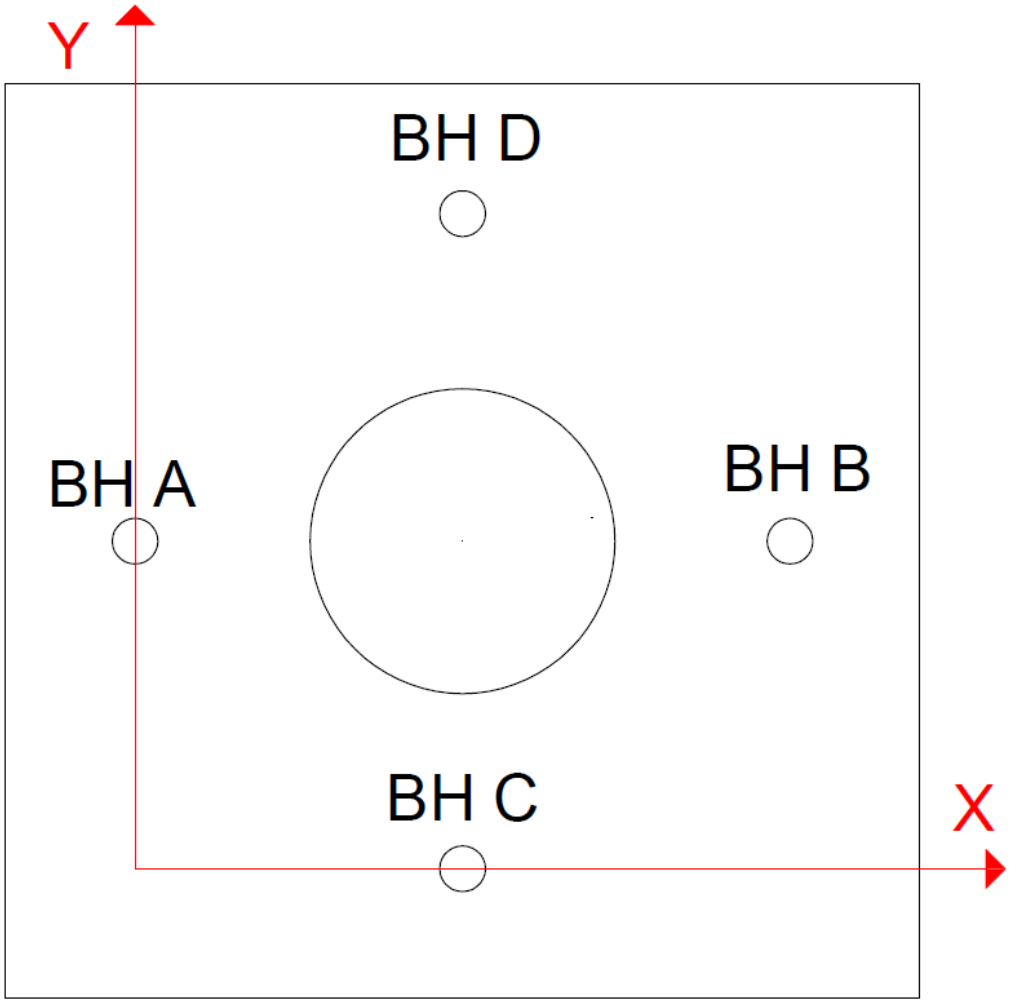

Figure 42: Axis convention

Table 5. Electrode coordinates

Electrode No.	X (m)	Y (m)	Z (m)	Borehole ID
0	0.00	0.21	0.074	
1	0.00	0.21	0.119	
2	0.00	0.21	0.164	
3	0.00	0.21	0.209	
4	0.00	0.21	0.254	
5	0.00	0.21	0.299	BH A
6	0.00	0.21	0.344	
7	0.00	0.21	0.389	
8	0.00	0.21	0.434	
9	0.00	0.21	0.479	
10	0.00	0.21	0.524	
11	0.00	0.21	0.569	
12	0.41	0.21	0.066	
13	0.41	0.21	0.111	BH B
14	0.41	0.21	0.156	
15	0.41	0.21	0.201	

© Modern2020

16	0.41	0.21	0.246	
17	0.41	0.21	0.291	
18	0.41	0.21	0.336	
19	0.41	0.21	0.381	
20	0.41	0.21	0.426	
21	0.41	0.21	0.471	
22	0.41	0.21	0.516	
23	0.41	0.21	0.561	
24	0.20	0.00	0.070	
25	0.20	0.00	0.115	
26	0.20	0.00	0.160	
27	0.20	0.00	0.205	
28	0.20	0.00	0.250	
29	0.20	0.00	0.295	BH C
30	0.20	0.00	0.340	
31	0.20	0.00	0.385	
32	0.20	0.00	0.430	
33	0.20	0.00	0.475	
34	0.20	0.00	0.520	
35	0.20	0.00	0.565	
36	0.20	0.42	0.073	
37	0.20	0.42	0.118	
38	0.20	0.42	0.163	
39	0.20	0.42	0.208	
40	0.20	0.42	0.253	
41	0.20	0.42	0.298	BH D
42	0.20	0.42	0.343	
43	0.20	0.42	0.388	
44	0.20	0.42	0.433	
45	0.20	0.42	0.478	
46	0.20	0.42	0.523	
47	0.20	0.42	0.568	

The degree of saturation recorded by each RH sensor at different times of the saturation test are presented in Table 6.

Table 6. Degree of saturation recorded by each RH sensor at different times of the saturation experiment

	Degree of saturation [%]							
Sensors	**H1**	**H2**	**H3**	**H4**	**H5**	**H6**	**H7**	**H8**
Before start	39	29	27		27	29	27	23
20hrs	86	29	27	26	27	29	27	23
250hrs	100	32	28	27	29	31	28	25
500hrs	100	38	29	28	30	33	30	26

© Modern2020

8.1.4 Data collection

ARES II unit, manufactured by GF Instruments, was used for the data collection of all ERT surveys performed in this section of the report.

The foam attached to the back of the PVC tubes were not enough to ensure a good contact between the electrodes and the borehole walls, thus water was injected into the four boreholes prior to each ERT survey.

Wilkinson *et al.* (2008) demonstrated that for borehole surveys, large geometric sensitivities of an electrode configuration occurs when the geometric factor, K, changes rapidly with position, which will occur when K is close to singular. Also, in the vicinities of the singularity, K will also be large. Therefore, an optimised protocol, including a combination of 4,516 quadripoles, was design and used for all ERT surveys carried out during both, temperature and saturation tests. The quadripole combinations are proposed in a way that each electrode of the quadripole must be in a different borehole, such as suggested in the illustration of Figure 43.

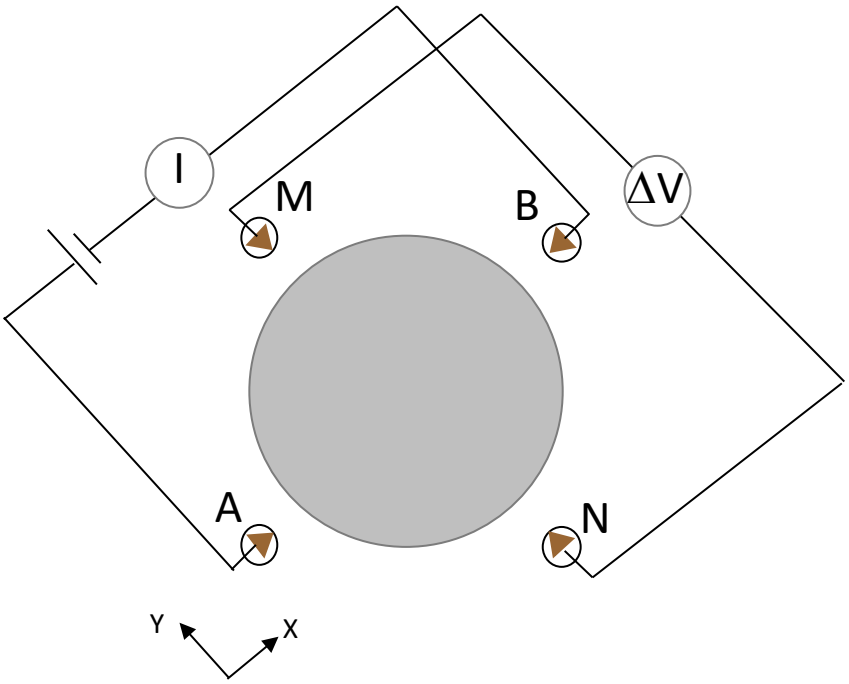

Figure 43: Electrical resistivity measurement with quadripole, A and B injection current electrodes, N and M potential difference measurement.

8.1.5 Data quality

Contact resistance checks were carried out prior to the data collection of each survey. As suggested by Day-Lewis *et al.* (2008), cut-offs of 50 kΩ for borehole data were implemented, since higher values may indicate that limited current can be injected for that electrode pair. After water injection, contact resistance were generally very good. As no contact resistance data larger than 50 kΩ was recorded, all data collected passed this criterion.

The ARES II unit used in the ERT surveys offer stacking procedure. The stack procedure consists of collecting each quadripole several times and average the results. This procedure has two clear

© Modern2020

advantages: (1) random noise is averaged out, which improves signal-to-noise ratio and (2) the standard deviation (stacking error) provides means of quantifying error and defining data weights for inversion. For all surveys carried out the minimum number of stacks selected was 4 and the maximum 8. The maximum variation coefficient accepted was 2%. Data with stacking errors larger than 3% were eliminated (Day-Lewis et al., 2008).

The length of the current pulse selected was 300 ms. Reciprocal measurements, which involves swapping current and voltage electrode pairs were also collected. As suggested by Slater et al. (2000), the reciprocal errors were calculated as follows:

$$e = R_n - R_r, \tag{10.1}$$

Where, R_n is the 'normal' resistance measurement and R_r is the 'reciprocal' resistance measurement

Overall, contact resistance, stacking errors and reciprocal measurement errors were the three features used to filter the data collected in the surveys performed. Table 7 presents a summary of the data quality of each ERT survey presented in this section of the report.

Table 7. Summary of data quality of ERT surveys

	Temperature test		
	Highest electrical contact recorded [kΩ]	**% of data where Sd > 3% [%]**	**Reciprocal errors: % of data where e > 10Ω [%]**
Env. Temp. Start: 20°C	7.8	1.3	12.3
Target heat: 90°C	9.9	0.8	1.6
Env. Temp. Cool down: 20°C	0.9	0.2	0.0

© Modern2020

Saturation test			
	Highest electrical contact recorded [kΩ]	**% of data where Sd > 3% [%]**	**Reciprocal errors: % of data where e > 10Ω [%]**
Before Water injection: 0hrs	18.1	1.3	16.6
After 24hrs	15.7	0.5	7.2
After 250hrs	18.2	0.7	7.2
After 500hrs	22.9	1.1	3.7

8.1.6 Inversions

Inversions were performed using the commercially available software package Res3DInv® (Loke, 2017) . Despite carefully testing numerous inversion settings (Day-Lewis et al., 2008), the default settings proved to be the most appropriate. These settings were used for all control parameters, which were kept identical for each inversion.

The software package used does not offer 3D time-lapse inversions; therefore, inversions were performed individually for each ERT survey and visually compared.

© Modern2020

9. References

Alkhalifah, T., Plessix, R.-É., 2014. A recipe for practical full-waveform inversion in anisotropic media: An analytical parameter resolution study. Geophysics 79, R91–R101. https://doi.org/10.1190/geo2013-0366.1

Asnaashari, A., Brossier, R., Garambois, S., Audebert, F., Thore, P., Virieux, J., 2015. Time-lapse seismic imaging using regularized full-waveform inversion with a prior model: Which strategy? Geophys. Prospect. https://doi.org/10.1111/1365-2478.12176

Banham, S., Pringle, J.K., 2011. Geophysical and intrusive site investigations to detect an abandoned coal-mine access shaft, Apedale, Staffordshire, UK. Near Surf. Geophys. 9, 483–496.

Benson, A.K., Payne, K.L., Stubben, M.A., 1997. Mapping groundwater contamination using dc resistivity and VLF geophysical methods–A case study. Geophysics 62, 80–86. https://doi.org/10.1190/1.1444148

Binley, A., Kemna, A., 2005. DC Resistivity and Induced Polarization Methods, in: Rubin, Y., Hubbard, S.S. (Eds.), Hydrogeophysics. p. 518.

Bleistien, N., 1986. Two-and-one-half dimensional in-plane wave propagation. Geophys. Prospect. 34, 686–703. https://doi.org/10.1111/j.1365-2478.1986.tb00488.x

Bossart, P., Thury, M., 2007. Research in the Mont Terri Rock laboratory: Quo vadis? Phys. Chem. Earth. https://doi.org/10.1016/j.pce.2006.04.031

Carcione, J.M., Cavallini, F., 1995. On the acoustic-electromagnetic analogy. Wave Motion. https://doi.org/10.1016/0165-2125(94)00047-9

Carey, A.M., Paige, G.B., Carr, B.J., Dogan, M., 2017. Forward modeling to investigate inversion artifacts resulting from time-lapse electrical resistivity tomography during rainfall simulations. J. Appl. Geophys. 145, 39–49. https://doi.org/10.1016/j.jappgeo.2017.08.002

Coscia, I., Greenhalgh, S.A., Linde, N., Doetsch, J., Marescot, L., Günther, T., Vogt, T., Green, A.G., 2011. 3D crosshole ERT for aquifer characterization and monitoring of infiltrating river water. Geophysics 76, G49–G59. https://doi.org/10.1190/1.3553003

Cosenza, P., Ghorbani, A., Florsch, N., Revil, A., 2007. Effects of drying on the low-frequency electrical properties of Tournemire argillites. Pure Appl. Geophys. 164, 2043–2066. https://doi.org/10.1007/s00024-007-0253-0

Dahlin, T., Leroux, V., 2012. Improvement in time-domain induced polarization data quality with multi-electrode systems by separating current and potential cables, in: Near Surface Geophysics. https://doi.org/10.3997/1873-0604.2012028

Dahlin, T., Leroux, V., Nissen, J., 2002. Measuring techniques in induced polarization imaging. J. Appl. Geophys. 50, 279–298.

Dahlin, T., Zhou, B., 2006. Multiple-gradient array measurements for multichannel 2D resistivity imaging. Near Surf. Geophys. https://doi.org/10.3997/1873-0604.2005037

Daily, W., Owen, E., 1991. Cross-borehole resistivity tomography. Geophysics 56, 1228–1235.

Daily, W., Ramirez, A., LaBrecque, D., Barber, W., 1995. Electrical resistance tomography experiments at the Oregon Graduate Institute. J. Appl. Geophys. 33, 227–237. https://doi.org/10.1016/0926-9851(95)90043-8

Danielsen, B.E., Dahlin, T., 2010. Numerical modelling of resolution and sensitivity of ERT in horizontal boreholes. J. Appl. Geophys. 70, 245–254. https://doi.org/10.1016/j.jappgeo.2010.01.005

Day-Lewis, F.D., Harris, J.M., Gorelick, S.M., 2002. Time-lapse inversion of crosswell radar data. Geophysics. https://doi.org/10.1190/1.1527075

Day-Lewis, F.D., Johnson, C.D., Singha, K., Lane Jr, J.W., 2008. Best Practices in Electrical Resistivity Imaging: Data Collection and Processing, and Application to Data from Corinna, Maine.

De Donno, G., Cardarelli, E., 2011. Assessment of errors from different electrode materials and configurations for electrical resistivity and time-domain IP data on laboratory models. Boll. di Geofis. Teor. ed Appl. 52, 1–13. https://doi.org/10.4430/bgta0006

de Lima, O.A.L., Sato, H.K., Porsani, M.J., 1995. Imaging industrial contaminant plumes with resistivity techniques. J. Appl. Geophys. 34, 93–108. https://doi.org/10.1016/0926-9851(95)00014-3

Deceuster, J., Delgranche, J., Kaufmann, O., 2006. 2D cross-borehole resistivity tomographies below foundations as a tool to design proper remedial actions in covered karst. J. Appl. Geophys. 60, 68–86. https://doi.org/10.1016/j.jappgeo.2005.12.005

Diersen, S., Lee, E.J., Spears, D., Chen, P., Wang, L., 2011. Classification of seismic windows using artificial neural networks, in: Procedia Computer Science.

© Modern2020

https://doi.org/10.1016/j.procs.2011.04.170

Doetsch, J., 2011. Joint and constrained inversion of geophsyical data for improved imaging of aquier structure and processes. Zurich. https://doi.org/https://doi.org/10.3929/ethz-a-006689501

Doetsch, J., Linde, N., Binley, A., 2010. Structural joint inversion of time-lapse crosshole ERT and GPR traveltime data. Geophys. Res. Lett. https://doi.org/10.1029/2010GL045482

Elis, V.R., Ustra, A.T., Hidalgo-Gato, M.C., Pejon, O.J., Hiodo, Y.F., 2016. Application of induced polarization and resistivity to the environmental investigation of an old waste disposal area. Environ. Earth Sci 75, 1–13. https://doi.org/10.1007/s12665-016-6157-5

Fan, J., Scheuermann, A., Guyot, A., Baumgartl, T., Lockington, D.A., 2015. Quantifying spatiotemporal dynamics of root-zone soil water in a mixed forest on subtropical coastal sand dune using surface ERT and spatial TDR. J. Hydrol. 523, 475–488. https://doi.org/10.1016/j.jhydrol.2015.01.064

Fichtner, A., 2011. Full Seismic Waveform Modelling and Inversion, Book. https://doi.org/10.1007/978-3-642-15807-0

Fisher, W.D., Camp, T.K., Krzhizhanovskaya, V. V., 2017. Anomaly detection in earth dam and levee passive seismic data using support vector machines and automatic feature selection. J. Comput. Sci. https://doi.org/10.1016/j.jocs.2016.11.016

French, H.K., Hardbattle, C., Binley, A., Winship, P., Jakobsen, L., 2002. Monitoring snowmelt induced unsaturated flow and transport using electrical resistivity tomography. J. Hydrol. 267, 273–284. https://doi.org/10.1016/s0022-1694(02)00156-7

Furche, M., Scuster, K., 2014. Long-term performance of engineered barrier systems PEBS.

Ganerød, G.V., Rønning, J.S., Dalsegg, E., Elvebakk, H., Holmøy, K., Nilsen, B., Braathen, A., 2006. Comparison of geophysical methods for sub-surface mapping of faults and fracture zones in a section of the Viggja road tunnel, Norway. Bull. Eng. Geol. Environ. 65, 231–243. https://doi.org/10.1007/s10064-006-0041-6

Garitte, B., Weber, H., Müller, H.R., 2015. Requirements, manufacturing and QC of the buffer components Report LUCOEX – WP2.

Gholami, Y., Brossier, R., Operto, S., Ribodetti, A., Virieux, J., 2013. Which parameterization is suitable for acoustic vertical transverse isotropic full waveform inversion? Part 1: Sensitivity and trade-off analysis. Geophysics 78, R81–R105. https://doi.org/10.1190/geo2012-0204.1

Giao, P.H., Chung, S.G., Kim, D.Y., Tanaka, H., 2003. Electric imaging and laboratory resistivity testing for geotechnical investigation of Pusan clay deposits. J. Appl. Geophys. 52, 157–175. https://doi.org/10.1016/S0926-9851(03)00002-8

Guérin, R., 2005. Borehole and surface-based hydrogeophysics. Hydrogeol. J. 13, 251–254. https://doi.org/10.1007/s10040-004-0415-4

Guitton, A., Alkhalifah, T., 2017. A parameterization study for elastic VTI full-waveform inversion of hydrophone components: Synthetic and North Sea field data examples. Geophysics 82, R299–R308. https://doi.org/10.1190/geo2017-0073.1

Hauck, C., Muhll, D. V, 2003. Permafrost monitoring using time-lapse resistivity tomography. Permafrost, Vols 1 2.

Hermans, T., Wildemeersch, S., Jamin, P., Orban, P., Brouyère, S., Dassargues, A., Nguyen, F., 2015. Quantitative temperature monitoring of a heat tracing experiment using cross-borehole ERT. Geothermics 53, 14–26. https://doi.org/10.1016/j.geothermics.2014.03.013

Karaoulis, M., Tsourlos, P., Kim, J.H., Revill, A., 2014. 4D time-lapse ERT inversion: Introducing combined time and space constraints, in: Near Surface Geophysics. https://doi.org/10.3997/1873-0604.2013004

Kemna, A., Kulessa, B., Vereecken, H., 2002. Imaging and characterisation of subsurface solute transport using electrical resistivity tomography (ERT) and equivalent transport models. J. Hydrol. https://doi.org/10.1016/S0022-1694(02)00145-2

Kiberu, J., 2002. Induced polarization and Resistivity measurements on a suite of near surface soil samples and their empirical relationship to selected measured engineering parameters. Interntional Inst. Geo-information Sci. Earth Obs. Enschede, Netherlands 119.

Köhn, D., De Nil, D., Kurzmann, A., Przebindowska, A., Bohlen, T., 2012. On the influence of model parametrization in elastic full waveform tomography. Geophys. J. Int. 191, 325–345. https://doi.org/10.1111/j.1365-246X.2012.05633.x

Korteland, S.A., Heimovaara, T., 2015. Quantitative inverse modelling of a cylindrical object in the laboratory using ERT: An error analysis. J. Appl. Geophys. 114, 101–115. https://doi.org/10.1016/j.jappgeo.2014.10.026

Kosková, L., Novák, J., 2012. Application of Edge and Line Detection to Detect the near Surface Anomalies in Potential Data 693–696. https://doi.org/10.5220/0004261206930696

© Modern2020

LaBrecque, D., Daily, W., 2008. Assessment of measurement errors for galvanic-resistivity electrodes of different composition. Geophysics 73, F55–F64. https://doi.org/10.1190/1.2823457

LaBrecque, D., Miletto, M., Daily, W., Ramirez, A., Owen, E., 1996. The effects of noise on Occam's inversion of resistivity tomography data. Geophysics 61, 538–548.

LaBrecque, D.J., Yang, X., 2001. Difference Inversion of ERT Data: a Fast Inversion Method for 3-D In Situ Monitoring. J. Environ. Eng. Geophys. 6, 83–89. https://doi.org/10.4133/JEEG6.2.83

Lanyon, G.W., 2008. HG-A (gas path through host rock and along seals) experiment: Discrete Fracture Network Models of Excavation Damage Zone at the HG-A site.

Loke, M.H., 2017. Rapid 3-D Resistivity & IP inversion using the least-squares method.

Loke, M.H., 2013. Tutorial : 2-D and 3-D electrical imaging surveys. Geotomo Softw. Malaysia 127.

Lopes, B. de C.F.L., Sachet, C., Sentenac, P., Benes, V., Dick, P., Bertrand, J., Tarantino, A., 2018. Preliminary non-intrusive geophysical electrical resistivity tomography surveys of a mock-up scale monitoring of an engineered barrier system at URL Tournemire. Geol. Soc. - Mult. Roles Clays Radioact. Waste Confin. 482. https://doi.org/10.1144/SP482.11

Lopes, B. de C.F.L., Tarantino, A., 2018. Modern 2020: LTRBM - ERT blank test report.

Lopes, B.C.F.L., Tarantino, A., 2018a. Modern2020 – Milestone 23 - Progress report.

Lopes, B.C.F.L., Tarantino, A., 2018b. As-Built Report: ERT demonstrator. Glasgow.

López-Sánchez, M., Mansilla-Plaza, L., Sánchez-de-laOrden, M., 2017. Geometric factor and influence of sensors in the establishment of a resistivity-moisture relation in soil samples. J. Appl. Geophys. 145, 1–11. https://doi.org/10.1016/j.jappgeo.2017.07.011

Manukyan, E., 2011. Seismic Monitoring and Elastic Full Waveform Inversion Investigations Applied To the Radioactive Waste Disposal. Zurich. https://doi.org/http://dx.doi.org/10.3929/ethz-a-006689521

Manukyan, E., Latzel, S., Maurer, H., Marelli, S., Greenhalgh, S.A., 2012a. Exploitation of data-information content in elastic-waveform inversions. Geophysics 77, R105–R115. https://doi.org/10.1190/geo2011-0184.1

Manukyan, E., Maurer, H., 2019. Elastic VTI full waveform inversion using cross-gradient constraints – an application to high level radioactive waste monitoring. GEOPHYSICS submitted.

Manukyan, E., Maurer, H., Marelli, S., Greenhalgh, S.A., Green, A.G., 2012b. Seismic monitoring of radioactive waste repositories. Geophysics 77, EN73-EN83. https://doi.org/10.1190/geo2011-0420.1

Manukyan, E., Maurer, H., Nuber, A., 2018. Improvements to elastic full-waveform inversion using cross-gradient constraints. Geophysics 83, R105–R115. https://doi.org/10.1190/geo2017-0266.1

Marelli, S., Manukyan, E., Maurer, H., Greenhalgh, S.A., Green, A.G., 2010. Appraisal of waveform repeatability for crosshole and hole-to-tunnel seismic monitoring of radioactive waste repositories. GEOPHYSICS 75, Q21–Q34. https://doi.org/10.1190/1.3479552

Marjavaara, P., Holt, E., Sjöblom, V., 2013. Customized Bentonite Pellets : Manufacturing , Performance and Gap Filling Properties.

Martinez-Pagan, P., Faz, A., Aracil, E., 2009. The use of 2D electrical tomography to assess pollution in slurry ponds of the Murcia region, SE Spain. Near Surf. Geophys. 7, 49–61. https://doi.org/10.3997/1873-0604.2008033

Maurer, H., Greenhalgh, S.A., Manukyan, E., Marelli, S., Green, A.G., 2012. Receiver-coupling effects in seismic waveform inversions. GEOPHYSICS. https://doi.org/10.1190/geo2010-0402.1

Merritt, A.J., Chambers, J.E., Wilkinson, P.B., West, L.J., Murphy, W., Gunn, D., Uhlemann, S., 2016. Measurement and modelling of moisture-electrical resistivity relationship of fine-grained unsaturated soils and electrical anisotropy. J. Appl. Geophys. 124, 155–165. https://doi.org/10.1016/j.jappgeo.2015.11.005

Müller, H.R., Garitte, B., Vogt, T., Köhler, S., Sakaki, T., Weber, H., Spillmann, T., Hertrich, M., Becker, J.K., Giroud, N., Cloet, V., Diomidis, N., Vietor, T., 2017. Implementation of the full-scale emplacement (FE) experiment at the Mont Terri rock laboratory. Swiss J. Geosci. https://doi.org/10.1007/s00015-016-0251-2

Mwakanyamale, K., Slater, L., Binley, A., Ntarlagiannis, D., 2012. Lithologic imaging using complex conductivity: Lessons learned from the Hanford 300 Area. GEOPHYSICS. https://doi.org/10.1190/geo2011-0407.1

Negri, S., Leucci, G., Mazzone, F., 2008. High resolution 3D ERT to help GPR data interpretation for researching archaeological items in a geologically complex subsurface. J. Appl. Geophys. 65, 111–120. https://doi.org/10.1016/j.jappgeo.2008.06.004

Ogilvy, A.A., Kuzmina, E.N., 1972. Hydrogeologic and Engineering-Geologic possibilities for employing the method of Induced potentials. Geophysics 37, 839–861.

© Modern2020

Olsson, P.-I., Fiandaca, G., Larsen, J.J., Dahlin, T., Auken, E., Olsson, P.-I., Auken, E., Larsen, J.J., Maurya, P.K., Dahlin, T., 2016. Doubling the Spectrum of Time-Domain Induced Polarization: Removal of Harmonic Noise and Self-Potential Drift, in: Proceedings of the 4th International Workshop on Induced Polarization.

Olsson, P.I., Dahlin, T., Fiandaca, G., Auken, E., 2015. Measuring time-domain spectral induced polarization in the on-time: Decreasing acquisition time and increasing signal-to-noise ratio. J. Appl. Geophys. https://doi.org/10.1016/j.jappgeo.2015.08.009

Operto, S., Gholami, Y., Prieux, V., Ribodetti, A., Brossier, R., Metivier, L., Virieux, J., 2013. A guided tour of multiparameter full-waveform inversion with multicomponent data: From theory to practice. Lead. Edge 32, 1040–1054. https://doi.org/10.1190/tle32091040.1

Orlic, N., Loncaric, S., 2010. Earthquake-explosion discrimination using genetic algorithm-based boosting approach. Comput. Geosci. https://doi.org/10.1016/j.cageo.2009.05.006

Parasnis, D.S., 2012. Principles of applied geophysics, Book.

Parkhomenko, E.I., 1971. Electrification phenomena in rocks. Plenum Press, New York.

Postic, F., Doussan, C., 2004. Test of different metal electrodes for IP measurements in time domain, in: 3rd International Workshop on Induced Polarization. Oléron Island. https://doi.org/10.1074/jbc.M112.362327

Pratt, R.G., Worthington, M.H., 1990. Inverse theory applied to multi-source cross- hole tomography. Part 1 : Acoustic wave-equation method. Geophys. Prospect. 38, 287–310.

Rahimi, S., Siddiqua, S., 2018. Relationships between Degree of Saturation, Total Suction, and Electrical and Thermal Resistivity of Highly Compacted Bentonite. J. Hazardous, Toxic, Radioact. Waste. https://doi.org/10.1061/(ASCE)HZ.2153-5515.0000380

Revil, A., 2012. Spectral induced polarization of shaly sands: Influence of the electrical double layer. Water Resour. Res. https://doi.org/10.1029/2011WR011260

Revil, A., Koch, K., Holliger, K., 2012. Is it the grain size or the characteristic pore size that controls the induced polarization relaxation time of clean sands and sandstones? Water Resour. Res. https://doi.org/10.1029/2011WR011561

Rothfuchs, T., Miehe, R., Moog, H., Wieczorek, K., 2004. Geoelectric Investigation of Bentonite Barrier Saturation, Grs-208.

Ruano, A.E., Madureira, G., Barros, O., Khosravani, H.R., Ruano, M.G., Ferreira, P.M., 2014. Seismic detection using support vector machines. Neurocomputing. https://doi.org/10.1016/j.neucom.2013.12.020

Rucker, D.F., Levitt, M.T., Greenwood, W.J., 2009. Three-dimensional electrical resistivity model of a nuclear waste disposal site. J. Appl. Geophys. 69, 150–164. https://doi.org/10.1016/j.jappgeo.2009.09.001

Samouëlian, A., Cousin, I., Tabbagh, A., Bruand, A., Richard, G., 2005. Electrical resistivity survey in soil science: A review. Soil Tillage Res. 83, 173–193. https://doi.org/10.1016/j.still.2004.10.004

Schmidt-Hattenberger, C., Bergmann, P., Labitzke, T., Wagner, F., Rippe, D., 2016. Permanent crosshole electrical resistivity tomography (ERT) as an established method for the long-term CO2monitoring at the Ketzin pilot site. Int. J. Greenh. Gas Control 52, 432–448. https://doi.org/10.1016/j.ijggc.2016.07.024

Slater, L., Binley, A.M., Daily, W., Johnson, R., 2000. Cross-hole electrical imaging of a controlled saline tracer injection. J. Appl. Geophys. 44, 85–102. https://doi.org/10.1016/S0926-9851(00)00002-1

Tarantola, A., 1984. in the Acoustic Approximation. Geophysics 49, 1259–1266.

Tonkov, N., Loke, M.H., 2006. A resistivity survey of a burial mound in the "Valley of the Thracian Kings." Archaeol. Prospect. 13, 129–136. https://doi.org/10.1002/arp.273

Vacquier, V., Holmes, C.R., Kintzinger, P.R., Lavergne, M., 1957. Prospecting for ground water by induced electrical polarization. Geophysics 12, 660–687.

Vinegar, H.J., Waxman, M.H., 1984. Induced polarization of shaly sands. GEOPHYSICS. https://doi.org/10.1190/1.1441755

Virieux, J., Operto, S., 2009. An overview of full-waveform inversion in exploration geophysics. Geophysics 74, WCC1-WCC26. https://doi.org/10.1190/1.3238367

Wang, J., Zhang, X., Du, L., 2017. A laboratory study of the correlation between the thermal conductivity and electrical resistivity of soil. J. Appl. Geophys. 145, 12–16. https://doi.org/10.1016/j.jappgeo.2017.07.009

Wang, Q., Tang, A.M., Cui, Y.J., Barnichon, J.D., Ye, W.M., 2013. A comparative study on the hydro-mechanical behavior of compacted bentonite/sand plug based on laboratory and field infiltration tests. Eng. Geol. 162, 79–87. https://doi.org/10.1016/j.enggeo.2013.05.009

Wilkinson, P.B., Chambers, J.E., Lelliott, M., Wealthall, G.P., Ogilvy, R.D., 2008. Extreme sensitivity of

© Modern2020

crosshole electrical resistivity tomography measurements to geometric errors. Geophys. J. Int. 173, 49–62. https://doi.org/10.1111/j.1365-246X.2008.03725.x

Yang, W., Lunn, R., Tarantino, A., 2015. MEMS sensor-based monitoring system for engineered geological disposal facilities. Mineral. Mag. 79, 1475–1483. https://doi.org/10.1180/minmag.2015.079.6.22

Yang, W., Lunn, R.J., Tarantino, A., El Mountassir, G., 2017. Laboratory Testing of a MEMS Sensor System for In-Situ Monitoring of the Engineered Barrier in a Geological Disposal Facility. Geosciences 7, 2–9. https://doi.org/10.3390/geosciences7020038

Yang, X., Lassen, R.N., Jensen, K.H., Looms, M.C., 2015. Monitoring CO2migration in a shallow sand aquifer using 3D crosshole electrical resistivity tomography. Int. J. Greenh. Gas Control 42, 534–544. https://doi.org/10.1016/j.ijggc.2015.09.005

Zieher, T., Markart, G., Ottowitz, D., Römer, A., Rutzinger, M., Meißl, G., Geitner, C., 2017. Water content dynamics at plot scale – comparison of time-lapse electrical resistivity tomography monitoring and pore pressure modelling. J. Hydrol. 544, 195–209. https://doi.org/10.1016/j.jhydrol.2016.11.019

Zohdy, A.A.R., Eaton, G.P., Mabey, D.R., 1974. Application of surface geophysics to ground-water investigations: U.S. Geological Survey Techniques of Water-Resources Investigations.

© Modern2020